Fall 2019

Biomaterials for bone regeneration

Youqu Shen

Department: Materials Science and Engineering

BIOMATERIALS FOR BONE REGENERATION

by

YOUQU SHEN

A DISSERTATION

Presented to the Faculty of the Graduate School of the

MISSOURI UNIVERSITY OF SCIENCE AND TECHNOLOGY

In Partial Fulfillment of the Requirements for the Degree

DOCTOR OF PHILOSOPHY

in

MATERIALS SCIENCE AND ENGINEERING

2019

Approved by:

Richard K. Brow, Advisor
Delbert E. Day
Gregory E. Hilmas
Yue-wern Huang
Julie A. Semon

PUBLICATION DISSERTATION OPTION

This dissertation consists of the following five articles, formatted in the style used by the Missouri University of Science and Technology:

Paper I: “Evaluation of open hollow hydroxyapatite microsphere on bone regeneration in rat calvarial defects”, pages 22-52, has been submitted to Biomedical Materials.

Paper II: “Hollow biphasic calcium phosphate microspheres from glass dissolution and reprecipitation; Part I: Particle formation and characterization”, pages 53-83, is intended for submission to the Journal of Biomedical Materials Research Part B.

Paper III: “Hollow biphasic calcium phosphate microspheres from glass dissolution and reprecipitation; Part II: *In vivo* Studies of Bone Regeneration and Blood Vessel Formation”, pages 84-108, is intended for submission to the Journal of Biomedical Materials Research Part B.

Paper IV: “Evaluation of 13-93 glass scaffolds with curved filaments to enhance bone formation in rat calvarial defects”, pages 109-141, is intended for submission to the Journal of Non-Crystalline Solids.

ABSTRACT

The purpose of this Ph.D. research is to investigate and improve two classes of hydroxyapatite (HA)-based biomaterials for bone repair: calcium phosphate microspheres and bioactive silicate glass scaffolds. These biomaterials were prepared with modified compositions and microstructures and then were evaluated for bone regeneration.

The open HA microspheres with dense convex surfaces and rough and porous concave surfaces were obtained by sectioning closed hollow HA microspheres. Bone regeneration with the open HA microspheres was greater than with the closed HA microsphere at 12 weeks. Hollow biphasic calcium phosphate (BCP) microspheres have been prepared with different fractions of HA and β-TCP (tricalcium phosphate) and their i*n vitro* and *in vivo* reactivities determined. The BCP microspheres with higher β-TCP/HA ratio (70/30) had faster degradation rates both *in vitro* and *in vivo* and a better capacity to regenerate bone. Moreover, the more reactive BCP microspheres were associated with significantly more blood vessel formation in the subcutaneous implants.

13-93 glass scaffolds with curved filaments stimulated a greater amount of new bone formation than straight filament scaffolds in rat calvarial defect at six weeks. Scaffolds with thin (6 ± 1 μm) HA-like surface layers were more effective at stimulating new bone formation, with the curved-filament structures again showing significant improvement in new bone growth compared to the surface-modified straight-filament structures.

ACKNOWLEDGMENTS

This research was initially financially supported by the National Institutes of Health, Grant #1R15DE023987-01. Additionally, I appreciate the financial support received from the Missouri S&T Center for Biomedical Research (CBR) and the Lasko Endowment in the Materials Science and Engineering Department. This research was technically supported by Materials Research Center and the Department of Biological Sciences at Missouri University of Science and Technology.

I'd like to thank Dr. Mohamed N. Rahaman for being my advisor at the start of my studies. I'd like to thank my advisor, Richard K. Brow for his guidance and support at the finish of my studies. The assistance of Dr. Yue-wern Huang and Dr. Julie A. Semon from the Department of Biological Sciences with the histological analysis is greatly appreciated. I'm grateful to Dr. Gregory E. Hilmas and Dr. Delbert E. Day for being my committee members and supporting for my research. Also, I'd like to thank Dr. Matthew O'Keefe for his help in my research. Thanks to Richard Watters (Animal Research Facility) for providing technical support for the *in vivo* experiments.

This work would not have been possible without the help of the members in biomaterials and glass groups, current and former, for their help in lab and useful discussion: Yinan Lin, Wei Xiao, Xin Liu, Jincheng Bai, Jenhsien Hsu, Parker Freudenberger, Han Zhang, Paul Porter.

Finally, thanks go to my husband, Sixie Huang, and all my family members and friends for their support during my study in Rolla.

TABLE OF CONTENTS

LIST OF ILLUSTRATIONS

SECTION Page

LIST OF TABLES

PAPER III

PAPER IV

NOMENCLATURE

Symbol	Description
SEM	Scanning electron microscopy
XRD	X-ray diffraction
EDS	Energy dispersive X-ray
ICP-OES	Inductively-coupled optical emission spectroscopy
BET	Brunauer-Emmett-Teller
BJH	Barrett-Joiner-Halenda
SSA	Specific surface area
ϕ	Diameter
wt%	Weight percent
SD	Standard deviation
Ca/P	Calcium to phosphorous ratio
FTIR	Fourier transform infrared
H&E	Hematoxylin and eosin
MCPM	Monobasic calcium phosphate monohydrate
DCPA	Dicalcium phosphate anhydrous, Monetite
DCPD	Dibasic calcium phosphate dihydrate, Brushite
OCP	Octacalcium phosphate
α-TCP	α-tricalcium phosphate
ACP	Amorphous calcium phosphate
CDHA	Calcium deficient hydroxyapatite

HA	Hydroxyapatite
TTCP	Tetracalcium phosphate
HCA	Carbonate hydroxyapatite
BCP	Biphasic calcium phosphate
BSA	Bovine serum albumin
TGF-β	Transforming growth factor-β
BMP	Bone morphogenetic protein
SBF	Simulated body fluid
KAc	Potassium acetate

SECTION

1. INTRODUCTION

1.1. THE NEED FOR IMPROVED SYNTHETIC BONE GRAFTS

Effective regeneration of bone defects caused by trauma or chronic disease is a significant clinical challenge. Over the past decades, researchers have investigated the mechanism of bone regeneration in order to develop better healing strategies [1-3]. Bone healing involves three primary stages: the early inflammatory stage, the repair stage, and the late remodeling stage (Figure 1.1) [4, 5]. These three stages are distinct but continuous. In the inflammatory stage, a hematoma forms and inflammatory cells infiltrate the bone resulting in the formation of granulation tissue, vascular tissue and immature tissue. During the repair stage, new blood vessels are developed to extend tissue regeneration and growth; a soft callus is formed around the repair site, and then the soft callus converts to a hard callus. Bone healing is completed during the remodeling stage in which the bone is restored to its original shape, structure and mechanical strength.

Bone defects are clinically reconstructed using treatments that rely on bone regeneration and augmentation. While various treatments have been investigated with encouraging results [6], complete and predictable bone reconstruction is often difficult to achieve[7]. Autologous bone grafts taken from intra- or extra-oral sites are the gold standard for treatment because they contain osteoinductive growth factors and osteogenic cells, and they provide a structural scaffold. However, disadvantages include limited

tissue availability, increased surgery time, and additional pain and cosmetic imperfection at the donor site [7-9]. Many of these issues can increase the health care cost for the patient [10]. An alternative to autogenous bone is allogenic bone that can induce moderate healing results due to its preserved osteoinductivity. However, allografts are costly, have unpredictable performance due to donor variance and adverse immune reactions, and they increase the risk of disease transference [11-13].Thus, there is a need to develop improved synthetic bone substitutes with good *in vivo* performance.

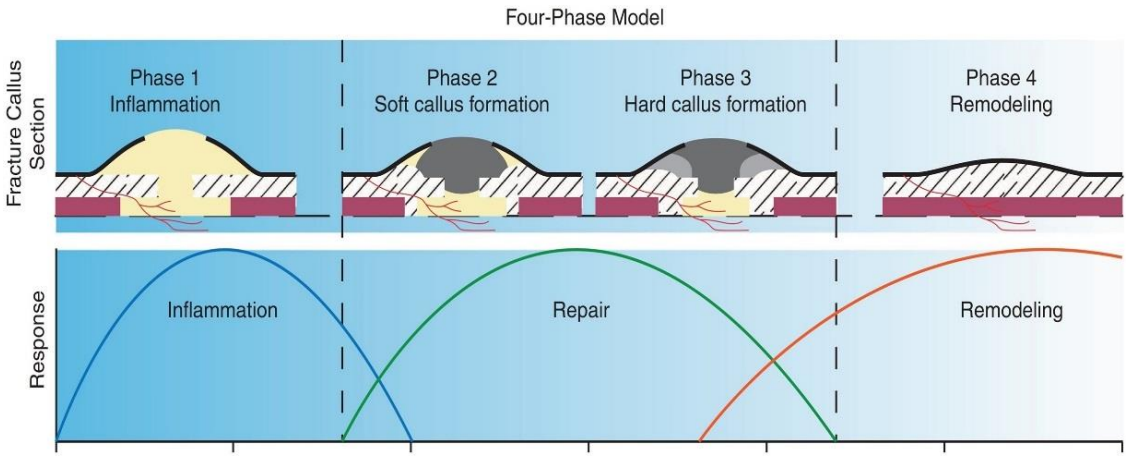

Figure 1.1. Schematic of the 3 primary stages for bone fracture healing [5].

A number of bone graft substitute components are currently available. These include inorganic materials (calcium phosphate and calcium sulfates in ceramics, pellets, and injectable cements) and organic materials (demineralized bone matrix, bone morphogenetic proteins). In the current bone substitute market, calcium phosphates, bioactive glasses, and their combinations with polymeric materials, are among the most commonly available synthetic bone substitutes [14].

1.2. DEVELOPMENT OF THE GLASS CONVERSION TECHNIQUE

Hench developed the first generation of bioactive glasses, including 45S5 Bioglass® (45% SiO_2, 24.5% Na_2O, 24.5% CaO, and 6% P_2O_5 –weight %) [15]. He reported that a carbonate-substitute hydroxyapatite-like (HCA) layer formed on the surface of 45S5 in contact with the body fluid. A borate analog glass, designated 45S5B1, and having the same composition as 45S5 bioactive glass but with SiO_2 replaced by B_2O_3, was investigated by Richard [16]. She found that a calcium phosphate layer formed on the glass surface after immersion in a K_2HPO_4 solution at 37°C; the calcium phosphate layer formed faster on 45S5B1 borate glass than on 45S5 glass. Fears [17] and Han [18] studied the reaction of glass spheres made from lithium calcium borate glass and sodium calcium borate glass in 0.25 M phosphate solution at 37 °C, and they reported the formation of hydroxyapatite.

1.2.1. Kinetics and Mechanism of Glass Conversion. The formation of a calcium phosphate layer on the surface of a calcium-containing borate glass immersed in a phosphate solution results from a series of dissolution-precipitation reactions. Ca^{2+} ions are released from a dissolving glass to the aqueous solution and when the local solubility limit is exceeded, these ions react with the phosphate anions to precipitate calcium phosphate phases on the glass surface. The initial precipitation products are often x-ray amorphous, with various Ca/P ratios depending on the experimental conditions, and so are classified as amorphous calcium phosphates (ACP) [15, 19, 20]. Figure 1.2 shows the solubility of different stable calcium phosphate phases as a function of pH [21, 22]. Hydroxyapatite (HA) is the most stable calcium phosphate phase in the pH range of typical conversion processes (pH=9-12), although other calcium phosphates are stable in

acidic conditions, and will precipitate from solutions with greater salinity. Figure 1.3 shows the speciation of phosphate anions in aqueous solutions as a function of pH; $H_2PO_4^-$ and HPO_4^{2-} are the dominant anions in solutions with pH<10, and PO_4^{3-} anions become increasingly significant in more alkaline solutions.

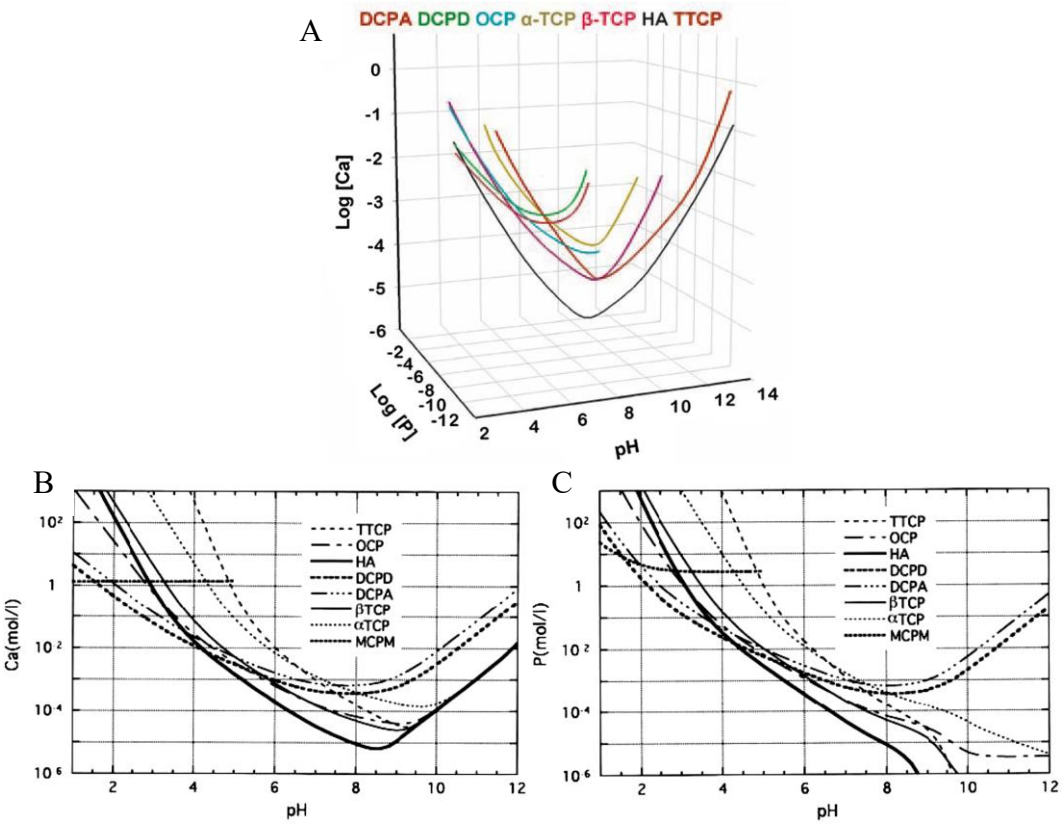

Figure 1.2. The solubility of different stable calcium phosphate phases as a function of pH. (A) 3D version of the classical solubility phase diagrams for the ternary system $Ca(OH)_2$–H_3PO_4–H_2O. Bottom: solubility phase diagrams in two-dimensional graphs, showing two logarithms of the concentrations of (B) calcium and (C) orthophosphate ions as a function of the pH in solutions saturated with various salts [22].

As the glass continues to dissolve, the calcium phosphate layer grows inward from the surface by the reaction of Ca^{2+} ions released from the glass with phosphate

anions that have transported through the reaction layer from the aqueous solution. The reaction continues until the soluble borate glass is completely dissolved. Figure 1.4 is a schematic diagram demonstrating the main steps in the conversion of a lithium-calcium-borate glass in a phosphate solution.

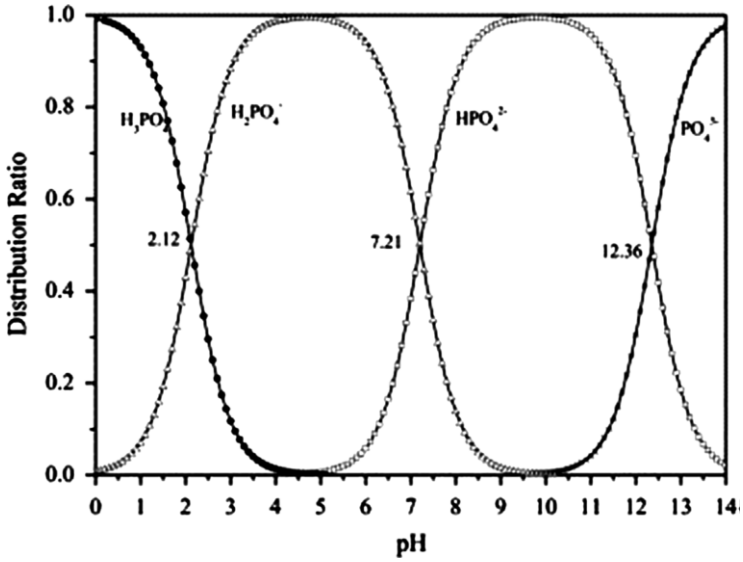

Figure 1.3. Dependence of phosphate species in aqueous solutions on pH [23].

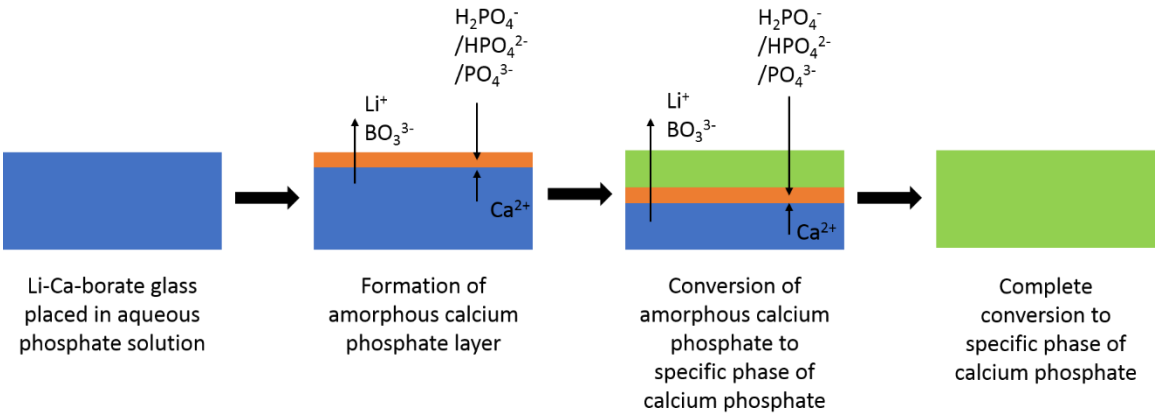

Figure 1.4. Schematic diagram presenting main steps in the conversion of calcium-containing borate glass (Li-Ca-B glass as example) in phosphate solution.

The final product of conversion is a calcium phosphate phase which depends on the pH of the solution. In acidic solutions, dicalcium phosphate dihydrate (DCPD, $CaHPO_4 \cdot 2H_2O$) or dicalcium phosphate anhydride (DCPA, $CaHPO_4$) can form [24], whereas in basic solutions, non- stoichiometric, calcium-deficient hydroxyapatite (CDHA, $Ca_{10-x}(HPO4)_x(PO4)_{6-x}(OH)_{2-x}$) can be produced [18, 20, 24]. Stoichiometric HA has PO_4^{3-} anions, some of which are replaced by HPO_4^{2-} or other anions (e.g. CO_3^{2-}) in CDHA [22]. Similar effects of solution pH on the precipitation of Ca-phosphate phases have been reported in other studies [25, 26].

The kinetics and mechanism of the formation of the CDHA layer on borate glass have been investigated in several studies [27-31]. The kinetics of glass conversion is often evaluated using weight loss data. The weight loss of glass is taken as the difference between the initial (unreacted) mass of particles and the mass at time t [29, 32], with the fraction of reacted glass given by α. Several models, then, can be used to analyze $\alpha(t)$, assuming spherical particles in aqueous solutions [33]. The contracting volume model (CVM) assumes a surface reaction-controlled mechanism where particles react with their surroundings, and as the reaction progresses, the unreacted material uniformly decreases in size. The kinetic equation for CVM is given as:

$$k_{cvm}t = 1 - (1 - \alpha)^{1/3} \quad (1)$$

where α is the fraction of sample reacted in time t and k_{CVM} is the CVM reaction rate constant. The three-dimensional diffusion model assumes that the transformation reaction is limited by the diffusion of a species through a reaction product to the reaction interface. The equation for the 3D diffusion is given as:

$$k_D t = \left[1 - (1 - \alpha)^{1/3}\right]^2 \quad (2)$$

where k_D is the diffusion model reaction rate constant.

Huang, et al. [29, 34] studied the effect of partially or fully replacing the SiO_2 content of 45S5 glass by B_2O_3 on the kinetics and mechanism of the conversion of glass particles to CDHA. Yao [30] did similar work for borate-substituted 13-93 glass particles. The conversion of particles of the borate analogue of 45S5 glass are well-described by a 3D diffusion model over the entire reaction time, whereas the conversion of the borosilicate and silicate glasses was better described by a contracting volume model in the initial stage and by a 3D diffusion model in the later stages [31].

Gu [27] studied the conversion of sodium calcium borate glasses to CDHA in 0.25 M K_2HPO_4. CVM had a good fit for glass conversion at 10, 22 and 37 °C. At 70 °C, the early stage data followed a CVM, but the data was better fit by a diffusion model at the later stages. The activation energy for the conversion reaction in the 10~70°C range was 32~36 kJ/mol, which is similar to activation energies for hydration of borate minerals [35, 36], indicating that glass dissolution controls the conversion kinetics.

George [37] investigated the conversion of 13-93B3 glass (12% K_2O, 6% Na_2O, 20% CaO, 5% MgO, 53% B_2O_3 and 4% P_2O_5 wt %) to calcium phosphate in water at 21 to 60 °C. The glass dissolution kinetics initially followed a reaction-controlled contracting volume model. As the glass dissolved, a Mg-substituted amorphous calcium phosphate layer precipitated on the glass surface. After the glass was ~25% reacted, the dissolution kinetics transitioned to follow a diffusion-controlled model. Both the reaction-controlled and diffusion-controlled kinetic reactions exhibited an Arrhenius relationship, with activation energies of ~32 and 41 kJ/mol, respectively, similar to those

reported by Gu [27]. The resulting amorphous calcium phosphate (ACP) layer had a greater Ca/P ratio than stoichiometric hydroxyapatite, which prevented the transition from ACP to HAp.

Table 1.1. Factors that influence final product of calcium borate glass conversion in phosphate solution.

Factors		Influence	Ref.
Glass composition	B_2O_3	Acts as a soluble matrix Rapid dissolution depends on B[3]/B[4] ratio	[29, 37, 39-42]
	CaO	Produces B[4] Reduces the glass dissolution rate, relative to the alkali oxides Forms calcium phosphate (CP) Determines CP layer thickness	[17, 18, 24, 27, 39, 40, 43-46]
	Alkali oxides	Affects B[3]/B[4] ratio Increases dissolution rate, relative to CaO Increases pH of solution	[24, 39, 40, 47]
	Other alkaline earth oxides	Produces B[4] Reduces the glass dissolution rate, relative to the alkali oxides Forms alkaline earth phosphates	[34]
Solution	pH	Affects the calcium phosphate phases that form Glass dissolution rate	[20, 21, 24, 37, 44, 45]
	Concentration of phosphate ions	Thickness and microstructure of the precipitation layers	[20, 44]
	Carbonate	Formation of a carbonate substituted calcium phosphate	[18, 24, 38]
	Fluoride	Formation of a fluoride substituted calcium phosphate	[24]
Temperature		Reaction rate Microstructure of final product	[18, 20, 27]

Table 1.2. Selected calcium phosphate phases of interest for biomedical applications. [22, 48]

Ca/P Molar Ratio	Name	Formula	pH stability range at 25°C	Density (g/cm^3)
0.5	MCPM (monobasic calcium phosphate monohydrate)	$Ca(H_2PO_4)_2 \cdot H_2O$	0.0–2.0	2.22
1.0	DCPA (dicalcium phosphate anhydrous, Monetite)	$CaHPO_4$	2.0–5.5	2.929
1.0	DCPD (dibasic calcium phosphate dihydrate, Brushite)	$CaHPO_4 \cdot 2H_2O$	2.0-6.0	2.319
1.33	OCP (octacalcium phosphate)	$Ca_8(HPO_4)_2(PO_4)_4 \cdot 5H_2O$	5.5-7.0	2.673
1.5	α-TCP (α-tricalcium phosphate)	$\alpha\text{-}Ca_3(PO_4)_2$	[a]	2.814
1.5	β-TCP (β-ticalcium phosphate)	$\beta\text{-}Ca_3(PO_4)_2$	[a]	3.067
1.2-2.2	ACP (amorphous calcium phosphate)	$Ca_xH_y(PO_4)_z \cdot nH_2O$, n = 3-4.5, 15%-20% H_2O	~5-12[b]	-
1.50-1.67	CDHA (calcium deficient hydroxyapatite; precipitated HAp, pHA, pHAp)[c]	$Ca_{10-x}(HPO_4)_x(PO_4)_{6-x}(OH)_{2-x}$ $(0 < x < 1)$	6.5-9.5	-
1.67	HAp, or OHAp (Hydroxyapatite)	$Ca_{10}(PO_4)_6(OH)_2$	9.5-12.0	3.155
2.0	TTCP, or TetCP (tetracalcium phosphate, Hilgenstockite)	$Ca_4(PO_4)_2O$	[a]	3.056

[a] These compounds cannot be precipitated from aqueous solutions.
[b] Always metastable. The composition of the precipitate depends on the composition and pH of the electrolyte solution.
[c] Occasionally, it is called “precipitated HA (HAp)”.

1.2.2. Parameters that Influence the Glass Conversion Reaction. The microstructural features of the calcium phosphate microspheres produced by the borate glass conversion process depend on the process parameters (Table 1.1). Fears [17] investigated the effect of the calcium content of lithium calcium borate glass spheres on the reaction product formation in aqueous phosphate solutions. The thickness of the calcium phosphate shell wall increased with increasing Ca-content in the initial glass spheres. Glasses with ≤ 40 wt% CaO formed CDHA microspheres with a hollow core and mesoporous shell. Glasses with > 40 wt% CaO formed solid but porous CDHA microspheres. For the hollow microspheres, the ratio of the diameter of the hollow core (d) to the outer shell diameter of the microsphere (D) was affected by the concentration of the phosphate solution and the temperature in the system [20]. The d/D ratio decreased as the concentration of the phosphate solution or temperature increased.

The composition of the converted product is affected by both the glass composition and solution chemistry, including the pH value. Huang [34] investigated the conversion of four-component borate glasses with the composition 10% Li_2O, 10% CaO, 10% AeO and 60% B_2O_3 (wt%) in an aqueous phosphate solution, where Ae is the alkaline earth element Mg or Ba. The reaction product after 30-50 hours was a calcium-magnesium (or -barium) phosphate phase. For variations in solution chemistry, carbonate or fluoride substituted CDHA could be produced by adding carbonate or fluoride ions to the conversion solution [24, 38]. The formation of specific calcium phosphate phases depends upon the pH of the solution. The stability of calcium phosphate phases, at different pH values, has been studied previously (Table 1.2). Based on the stability of these calcium phosphate phases, Vanderspiegel [24] related the transformation of

potassium calcium borate glasses to specific crystalline calcium phosphate phases. By adjusting the pH of the conversion solution, these glasses produced three poorly-crystallized calcium phosphate phases, including DCPD at pH≈4.4, DCPA at pH≈5.5, and CDHA at pH≈9.2.

1.2.3. Hollow HA Microspheres. As mentioned before, the hollow HA microsphere technology was developed at Missouri S&T to address the need for bone graft substitution materials [17, 20, 49, 50]. Glass microspheres with the composition of 15CaO, 11Li_2O,74B_2O_3 (wt%), designated CaLB3-15, were converted in 0.02 M K_2HPO_4 solution at 37 °C and pH = 9 [49] to form hollow CDHA microspheres with mesoporous shell walls, an example of which is shown in Figure 1.5.

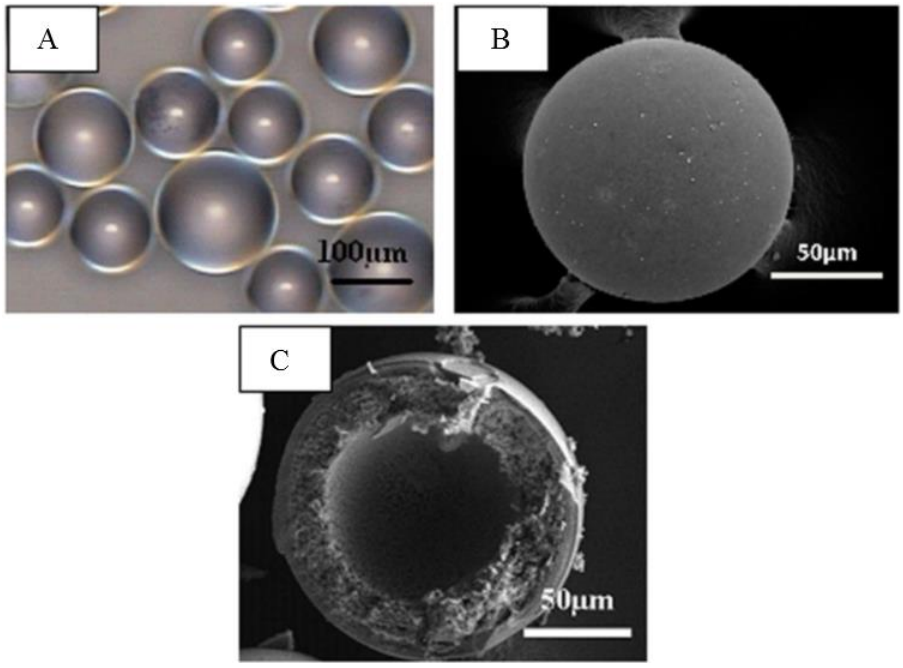

Figure 1.5. Hollow CDHA microspheres produced by glass conversion. (A) Optical image of starting glass (CaLB3-15) microspheres, and SEM images of (B) external surface of hollow CDHA microsphere prepared by converting the glass microspheres for 48 h in 0.02M K_2HPO_4 solution at 37°C and pH = 9, (C) cross section of hollow CDHA microsphere [49].

As a synthetic bone graft, the hollow CDHA microspheres lack the osteogenic cells and osteoinductive growth factors present in autologous bone. However, hollow CDHA microspheres can be combined with growth factors to enhance bone regeneration. The hollow CDHA microspheres with high surface areas have been used as platforms for controlled delivery of proteins [49-52]. Previous work at Missouri S&T showed that hollow CDHA microspheres can absorb proteins like bovine serum albumin (BSA) [49], transforming growth factor-β (TGF-β) [50], and bone morphogenetic protein-2 (BMP-2) [52], and release these proteins *in vitro* or *in vivo*.

Implantation of the hollow HA microspheres in rat calvarial defects *in vivo* stimulated limited new bone formation at 6 weeks and 12 weeks, whereas first loading the hollow CDHA microspheres with TGF-β resulted in an improvement of new bone formation in rat calvarial defects at 6 weeks, but not at 12 weeks [50].The new bone in the implant with the microspheres loaded with TGF-β was only ~20% of the total defect area after 6 weeks or 12 weeks. The hollow CDHA microspheres loaded with BMP-2 (1 μg per defect) showed a significant increase in bone regeneration compared with the microspheres without BMP-2 at 6 weeks. Hollow CDHA microspheres coated with different thickness of poly(lactic-co-glycolic acid) (PLGA) delayed the release of BMP-2 [52].

Open CDHA microspheres are hollow CDHA microspheres (hereafter, called closed HA microspheres) that have been sectioned, as shown in Figure 5C. From the histological characterization of implants in rat calvarial defects, enhanced new bone growth was noted in the micro-concavity of open CDHA microspheres [52]. Previous work [53] showed that the open CDHA microspheres with exposed micro-concave

mesoporous hydroxyapatite in their cores promoted osteogenic differentiation of rat mesenchymal stem cells and increased alkaline phosphatase activity *in vitro* compared to closed CDHA microspheres. In the follow-up study [53], rat calvarial defects implanted with the CDHA microspheres containing 50% open CDHA microspheres showed considerable new bone formation in the many micro-concave regions of the open CDHA microspheres. The enhanced osteogenic property of open CDHA microspheres is presumably a result of their specific microgeometry.

Although the hollow CDHA microspheres showed promising results in bone repair, the effectiveness of these open CDHA microspheres still needs to be improved to optimize bone regeneration.

1.3. BIPHASIC CALCIUM PHOSPHATE

Hydroxyapatite (HA, $Ca_{10}(PO_4)_6(OH)_2$) is widely used as a synthetic bone graft material for bone regeneration[22, 54, 55]. It is biocompatible and osteoconductive and produces no systemic toxicity or immunological reactions. Osteoblasts and osteoclasts adhere well to the surface of HA to form the cytoskeletal structure [56-59]. Moreover, HA forms a chemical bond between the implant and surrounding bone [60]. However, HA has found limited use as an implant material, principally because it lacks the osteoinductivity and osteogenicity possessed by allografts or autografts [1, 14, 61, 62]. In practice, mixing HA with osteogenic growth factors is often needed to achieve desirable bone regeneration [1, 14, 61].

Table 1.3. Commercial BCP products and weight ratios of composition phases [75].

β-TCP%	HA%	Brand name
<4	>96	Calciresorb (Ceraver, France)
20	80	Osteosynt (Einco, Brazil)
25	75	TCH (Kasios, France)
30	70	Ceratite (NGK Spark Plug, Japan) OrthoCer HA TCP (Baumer, Brazil)
35	65	CuriOs (Progentix Orthobiology BV, Netherlands) Ceraform (Teknimed, France) Calcicoat (Zimmer, IN)
40	60	BCP (Depuy Bioland, France) BCP BiCalPhos (Medtronic, MN) BonaGraft (Biotech One, Taiwan) BoneMedik-DM(Meta Biomed, Korea) CellCeram (Scaffdex Oy, Finland) GenPhos HA TCP (Baumer, Brazil) Graftys BCP (Graftys, France) Hatric (Arthrex, US) Hydros (Biomatlante SA, France) Kainos (Signus, Germany) MasterGraft Granules (Medtronic Sofamor Danek, US) MBCP (Biomatlante SA, France) OpteMx (Exactech, FL) Ossceram nano (Bredent Medical, Germany) Osteosynt (Einco, Brazil) Ostilit (Stryker Orthopaedics, NJ) SBS (ExpanScience, France) TriOsite (Zimmer, IN) 4Bone (MIS, Israel)
45	55	CuriOs (Progentix Orthobiology BV, Netherlands) Eurocer (FH, France)
50-70	30-50	Indost (Polystom, Russia)
80	20	BoneCeramic (Straumann, Switzerland) BoneSave (Stryker Orthopaedics, NJ) Kainos (Signus, Germany) MBCP+ (Biomatlante SA, France) OsSatura BCP (Integra Orthobiologics, CA) Osteosynt (Einco, Brazil) ReproBone (Ceramisys, UK) Tribone 80 (Stryker, Europe)

Tricalcium phosphate (β-TCP, $Ca_3(PO_4)_2$), also known as bone ash, is a source for calcium and phosphorus, which can be easily assimilated and absorbed by the body. β-TCP is also widely used in calcium phosphate bone cements [63-65], and other types of bone-substitution bioceramics [66-68], including those for dental applications [69]. β-TCP is both osteoconductive and osteoinductive, and due to its low interfacial energy with respect to apatite, it can provoke the precipitation of an apatite layer upon incubation in aqueous ionic solutions [70]. β-TCP cannot be directly precipitated from aqueous solutions [22]; instead, it forms when other phases, like CDHA [71] or mixtures of materials like dicalcium phosphate anhydrous and CaO [72], are heated above about 800°C. β-TCP can also be prepared at relatively low temperatures (~150 °C) by precipitation in water-free media, such as ethylene glycol [69].

In general, HA is poorly bioresorbable, whereas β-TCP is more bioresorbable and can be replaced by new bone at faster rates [22, 48]. These properties mean that the rate of degradation and bioactivity of calcium phosphate implant materials can be tailored using biphasic calcium phosphate (BCP) materials with a range of β-TCP-to-HA ratios [73, 74]. The *in vivo* dissolution/reprecipitation processes of BCP materials have been studied extensively by TEM [73, 74]. Their dissolution rates are dependent on the β-TCP/HA ratio, and the microcrystals that form during reprecipitation have crystallographic properties and Ca/P ratios similar to those of bone apatite [74]. Moreover, the new apatite crystals are defined as carbonate-apatite [73].

BCP ceramics with various ratios of β-TCP and HA are known to be effective and biocompatible scaffolds for tissue-engineering applications. The ratio between the more soluble β-TCP and the more stable HA has been varied to adjust the level of bioactivity,

bioresorbability, osteoconductivity, and osteoinductivity [75-78]. BCPs may be produced by mixing HA and β-TCP powders, or by sintering CDHAs at high temperature to produce mixtures of the two different phases[78].

Although various BCP products with different β-TCP/HA ratios have been evaluated in large number of studies, there seems to be no agreement about the optimal ratio of BCP phases for clinical applications [75]. Currently, there are over 30 commercially available BCP bone substitute products for various orthopedic and maxillofacial applications. The commercial BCP products with relative β-TCP/HA weight ratios are summarized in Table 1.3 [75].

1.4. ADDITIVE MANUFACTURE OF BIOACTIVE GLASS SCAFFOLDS

Bioactive glasses are widely used as scaffold materials for bone repair, due to their biocompatibility, osteoconductivity, their ability to form hydroxyapatite (HA) -like layers *in vivo*, and their ability to form a strong bond with the host bone. By adjusting the composition, a bioactive glass can release certain elements, such as boron [79], zinc [80, 81], copper [82, 83], and strontium [84], in a controlled manner that facilitates bone regeneration. Bioactive silicate glasses, including 45S5 [85, 86] and 13-93 [87-89], have been approved by the Food and Drug Administration (FDA) for *in vivo* use, and scaffolds based on these bioactive glasses can be fabricated with different architectures to provide desired mechanical and chemical environments for bone reconstruction. 13-93 ($53SiO_2$, $6Na_2O$, $12K_2O$, 5MgO, 20CaO, $4P_2O_5$, wt%) is a bioactive glass that is more stable against crystallization than is 45S5 [90, 91], and so has been used in applications that

require heat treatments to consolidate glass particles or to create bonds between structural elements by viscous flow [92-95].

Additive manufacturing techniques have led to innovative design and control of scaffold architectures [96]. At Missouri S&T, porous bioactive glass scaffolds have been fabricated using different manufacturing techniques, their *in vitro* mechanical properties have been characterized, and their ability to support bone infiltration *in vivo* has been evaluated. Mechanically strong porous scaffolds of 13-93 bioactive glass were created using a freeze extrusion fabrication (FEF) technique [94, 97]. Subsequently, the robocasting process was used to manufacture scaffolds from 13-93 bioactive glass [92, 98, 99].

Scaffolds with a grid-like microstructures (Figure 1.6), produced by robocasting 13-93 bioactive glass, promote the formation of new bone in rat calvarial defects. Pretreatment of these glass scaffolds in a phosphate solution to convert a thin surface layer of glass (~ 5 μm) to amorphous calcium phosphate or Ca-deficient hydroxyapatite prior to implantation, significantly enhances the capacity of the scaffold in bone regeneration [99]. Compared with other architectures of scaffolds made with the same glass composition (Table 1.4), these results indicated that the grid-like architecture has a better capacity to support bone regeneration than the oriented, trabecular and fibrous structures. By loading the surface modified scaffold with BMP-2 (1 μg per defect), new bone regeneration that infiltrated the scaffold significantly increased to 60% at six weeks post-implantation [99].

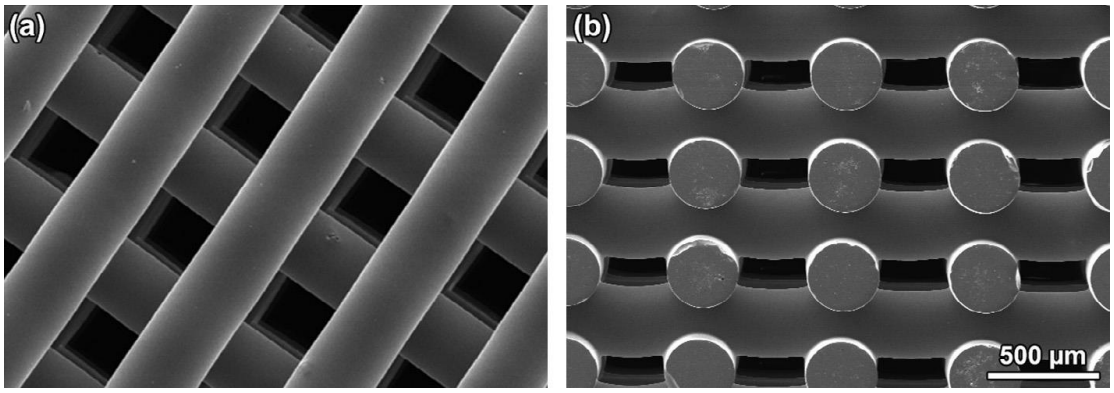

Figure 1.6. SEM images of silicate 13-93 bioactive glass scaffolds prepared by robotic deposition (robocasting): (a) plane of deposition (xy plane); (b) perpendicular to the deposition plane (z direction) [92].

Table 1.4. Comparison of new bone formed in scaffolds composed of silicate 13-93 glass with different microstructures after implantation in rat calvarial defects (4.0-4.6 mm in diameter × 1.5 mm) [99].

Microstructure of scaffolds	Porosity (%)	Pore size (µm)	New bone (%)		Implantation time (weeks)	Ref.
			Available pore area	Total area		
Grid-like	47	300×300×150	32 ± 13	18 ± 8	6	[99]
Trabecular	80	100-500	25 ± 12	19 ± 9	12	[100]
Oriented	50	100-150	37 ± 8	18 ± 3	12	[100]
Fibrous	50	50-500	~17[a]	8.5 ± 2	12	[101]

The amount of new bone is shown as a percent of the available pore space (area) in the scaffolds and the total defect area.
[a] Estimated from the total defect area.

Although the porous scaffolds of 13-93 bioactive glass with modified surfaces were promising in healing bone defects *in vivo*, the ability to regenerate bone still needs

to be improved. Since the architecture of the glass scaffold plays an important role in bone repair, optimization of these structures, made possible by additive manufacturing techniques, may enhance the bone regeneration.

Rumpler et al [38] described curvature-driven effects that promoted *in vivo* tissue formation in scaffolds, particularly on concave surfaces, and Paris et al. [19] developed a scaffold curvature-mediated mechanism for the *in vivo* bio-mineralization of extra-cellular matrix. An *in vivo* test showed that concavities stimulated the formation of blood vessels which play an important role in bone regeneration [102]. Bone formation by intramembranous ossification was preferred on a concave surface [103], and concavity was shown to be conducive to the accumulation of growth factors, such as bone morphogenetic proteins (BMPs) [104]. Based on these results, the addition of concave structures into the design and fabrication of 13-93 glass scaffolds may have a positive effect on bone regeneration.

In the end, it is clear that the microstructures and compositions of the materials used for synthetic bone graft are significant factors for bone repair. Novel materials, like those derived from the glass dissolution/precipitation process, and additive manufacturing techniques like robocasting, provide researchers with new opportunities to optimize those medical devices, and so to ultimately enhance a patient's recovery from bone defects.

2. RESEARCH OBJECTIVE

The objective of this study is to investigate and improve two classes of hydroxyapatite-based biomaterials for bone repair: 1) hollow calcium phosphate microspheres with different microstructures and compositions, and 2) bioactive silicate glass (13-93) scaffolds with different architectures to promote bone regeneration.

A considerable amount of new bone growth in the micro-concavity of open HA microspheres was observed in previous work at Missouri S&T [52, 53]. As open HA microspheres can be systematically obtained by sectioning closed HA microspheres, we hypothesize that open HA microspheres with special characteristics can improve bone regeneration compared to the closed HA microspheres. One goal of this study is to investigate the dependence of microgeometry, size, and time on bone regeneration in an osseous model, and then to evaluate the capacity of open HA microspheres loaded with BMP-2 for bone regeneration in a rat calvarial defect model.

Additionally, previous studies [38, 50, 52] have shown that the hollow CDHA microspheres alone have limited capacity for bone regeneration, likely because of their chemical stability. In the present study, hollow BCP microspheres are described, produced by heat-treating CDHA microspheres prepared using the glass conversion technique. The degradation rates and performance *in vitro* and *in vivo* are evaluated.

Finally, considering the effects of scaffold architecture on bone regeneration, we hypothesized that 13-93 glass scaffolds with curved filaments, produced by the robocasting technique, may have improved capability to regenerate bone *in vivo*. Some

scaffolds were pre-reacted in a phosphate solution to form a thin HA-like layer, prior to implantation and the capability of 13-93 glass scaffolds with curved filaments to facilitate bone formation is evaluated using a rat calvarial defect model.

PAPER

I. EVALUATION OF OPEN HOLLOW CDHA MICROSPHERES ON BONE REGENERATION IN RAT CALVARIAL DEFECTS

Youqu Shen[1], Mohamed Rahaman[1], Yongxian Liu[1], Yue-Wern Huang[2]

[1]Department of Materials Science and Engineering, Missouri University of Science and Technology Rolla, MO, 65409

[2]Department of Biological Sciences, Missouri University of Science and Technology Rolla, MO, 65409

ABSTRACT

Hollow Ca-deficient hydroxyapatite (CDHA) microspheres facilitate bone regeneration in rats with non-healing calvarial defects. Open CDHA microspheres were obtained by sectioning closed hollow CDHA microspheres. The open CDHA microsphere had dense outer (convex) surfaces and rough and porous inner (concave) surfaces. For both size ranges (ϕ106-150 μm vs. ϕ212-250 μm), the open CDHA microsphere were more effective in facilitating bone regeneration than the closed CDHA microspheres in rat calvarial defects. After twelve weeks, bone regeneration in the open CDHA microspheres (49 ± 7% for ϕ106-150 μm; 40 ± 8% for ϕ212-250 μm) was greater than the closed CDHA microspherse (26 ± 8% for ϕ106-150 μm; 30 ± 9% for ϕ212-250 μm). Furthermore, the smaller open CDHA microspheres showed a significant increase in bone regeneration over the larger open CDHA microspheres at both 6 weeks and 12 weeks. The difference in bone regeneration between these microspheres may be due to

their differences in microstructures, namely curvature, concavity, porosity, surface roughness, and total surface area available for cell attachment.

1. INTRODUCTION

Effective regeneration of bone defects caused by trauma or chronic diseases is a significant clinical challenge. Over the past few decades, researchers have investigated the mechanism of bone regeneration to better inform the designs of healing strategies [1-3]. Bone healing involves three primary stages: the early inflammatory stage; the repair stage and the late remodeling stage [4]. These three stages are distinct, but continuous. In the inflammatory stage, a hematoma forms and inflammatory cells infiltrate the bone, resulting in the formation of granulation tissue, vascular tissue and immature tissue. During the repair stage, new blood vessels are developed to facilitate tissue regeneration and a soft callus is formed around the repair site. Bone healing is completed during the remodeling stage in which the bone is restored to its original shape, structure and mechanical strength.

Clinically, bone deficiency is overcome using treatments that rely on bone regeneration and augmentation. While various treatments have been investigated with encouraging results [5], complete and predictable bone reconstruction is often difficult [6]. Autologous bone grafts are the gold standard for treatment because they contain osteoinductive growth factors, osteogenic cells and a structural scaffold. However, disadvantages of this treatment include limited tissue availability, increased surgery time, additional pain and cosmetic imperfection at the donor site [6-8]. Many of these issues

can increase the health care cost for the patient [9]. An alternative to autogenous bone is allogenic bone, which can induce moderate healing results due to its preserved osteoinductivity. However, allografts are costly, can have unpredictable effects on growth due to donor variance, cause adverse immune reactions, and increase the risk of disease transference [10-12]. Synthetic bone grafts have advantages such as consistent quality, safety, and good tissue tolerance, but they usually function as inert or merely osteoconductive implants. Encouraging results have been reported.

Hydroxyapatite (HA), the main component and essential ingredient of human bone, can be prepared by various methods. Studies have demonstrated that HA supports bone regeneration and bonding to surrounding tissue because of its biocompatibility, bioactivity, and osteoconductivity [13]. Closed hollow microspheres composed of Ca-deficient hydroxyapatite (CDHA) can be produced using the glass conversion technique [14]. Previous studies showed that closed CDHA microspheres promoted the regeneration of bone in non-healing rat calvarial defects [15, 16], and that the mechanical properties and biological response depended on the microsphere size (ϕ106-150 μm and ϕ150-250 μm) [17]. In these in vivo tests, it was occasionally observed that better bone regeneration was associated with broken microspheres with exposed micro-concavity [16, 18], and this observation is the motivation for the present study, to see more systematically if open CDHA microsphere with particular geometric characteristics can yield better bone regeneration compared with the closed CDHA microspheres. Closed and open CDHA microspheres with two size ranges (ϕ106-150 μm and ϕ212-250 μm) of were created and bone regeneration was evaluated with a rat calvarial defect model.

2. MATERIALS AND METHODS

2.1. PREPARATION OF CLOSED AND OPEN CDHA MICROSPHERES

The closed hollow CDHA microspheres were prepared by conversion of solid glass microspheres in an aqueous phosphate solution, as described in a previous study [14]. Briefly, calcium-lithium-borate glass with the composition of 15CaO, 11Li_2O and 74B_2O_3 (wt%), designated as CaLB3-15, was prepared by melting $CaCO_3$, Li_2CO_3, and H_3BO_3 (Alfa Aesar, Haverhill, MA, USA) in a platinum crucible at 1200 °C for 45 min and then quenching the melt between stainless steel plates. Glass particles were obtained by grinding the glass using a a mortar and pestle, crushing the powder in a shatter box, and sieving through 100 and 140 mesh (US standard) sieves for the ϕ106-150 μm size range, or 60 and 70 mesh sieves for the ϕ212-250 μm size range. Glass microspheres were obtained by dropping the particles down through a vertical furnace at 1200 °C. The closed hollow hydroxyapatite microspheres were obtained by reacting the glass microspheres in a 0.02 M K_2HPO_4 solution at 37 °C and pH = 9 for 7 days. In the conversion process, 1 g glass was immersed in a 200 ml phosphate solution and the system was stirred gently and continuously. The converted microspheres were washed with distilled water and anhydrous ethanol, and then dried at room temperature for at least 12 h, and at 90 °C for at least 12 h.

The open CDHA microspheres were obtained by sectioning the closed hollow CDHA microspheres using a microtome. Briefly, the closed CDHA microspheres were fixed on a wax block using a water-soluble tape and were sectioned by microtome. The open CDHA microspheres were washed with distilled water and ethanol, and then dried

at room temperature for at least 12 h, and at 90 °C for at least 12 h. Any debris left in the open CDHA microspheres after sectioning was removed using sieves.

2.2. CHARACTERIZATION OF CLOSED AND OPEN CDHA MICROSPHERES

The microstructures of the closed and open CDHA microspheres were observed using a scanning electron microscope (SEM; S4700 Hitachi, Tokyo, Japan) with an accelerating voltage of 15kV and working distance at 12 mm, and compositions were determined using energy dispersive X-ray (EDS) with an electron beam spot size of 1 μm.

The specific surface area (SSA) of the closed and open CDHA microspheres and pore size distributions of the shell walls were measured using nitrogen absorption (Autosorb-1; Quantachrome, Boynton Beach, FL) as described in a previous study [14]. Three hundred milligrams of closed or open CDHA microspheres were weighed and evacuated at 120 °C for 15 h to remove absorbed moisture. The volumes of nitrogen absorbed and desorbed at different relative gas pressures were measured and used to construct adsorption-desorption isotherms. The first twelve points of the adsorption isotherm, which initially followed a linear trend implying monolayer formation of adsorbate, were fitted to the Brunauer-Emmett-Teller equation to determine the specific surface area. The pore size distributions of the shell wall of the hollow CDHA microspheres were calculated using the Barrett-Joiner-Halenda method applied to the deposition isotherms [19].

2.3. ANIMALS AND SURGICAL PROCEDURES

All animal use and care procedures were approved by the Missouri S&T Institutional Animal Care and Use Committee in compliance with the NIH Guide for Care and Use of Laboratory Animals (1985). The rat calvarial defects were implanted with four groups of implants composed of closed or open hollow CDHA microspheres for 6 weeks and 12 weeks (Table 1). The implantation time was based upon considerable bone regeneration in rat calvarial defects implanted with hollow CDHA microspheres observed in previous studies [15, 16]. Closed or open CDHA microspheres in the two size ranges were randomly implanted into defect areas, but mixing implants of closed and open microspheres in the same animal was avoided due to the possible migration of low-weight open CDHA microspheres.

Table 1. Implants groups composed of closed or open hollow CDHA microspheres.

Group	CDHA microspheres		Sample size (n)	
			6 weeks	12 weeks
1	106-150 μm	Closed	5	5
2		Open	5	5
3	212-250 μm	Closed	5	10
4		Open	5	10

The male Sprague-Dawley rats (3 months old, weight = 350 ± 30 g, Envigo, USA) were acclimated for 2 weeks to diet, water, and housing under a 12 h/12 h light/dark cycle. The rats were anesthetized with a combination of ketamine and xylene

(0.15 µl per 100 g) and maintained under anesthesia with isoflurane in oxygen. The surgery area on each animal was shaved, scrubbed with 70% ethanol and iodine, and then draped. With sterile instruments and using an aseptic technique, a 1 cm cranial skin incision was made in an anterior to posterior direction along the midline. The subcutaneous tissue, musculature and periosteum were dissected and reflected to expose the calvaria. Bilateral full thickness defects (4.6 mm in diameter) were created in the central area of each parietal bone using a saline-cooled trephine drill. The sites were constantly irrigated with sterile PBS to prevent overheating of the bone margins and to remove the bone debris. Each defect was randomly implanted with the CDHA microspheres from the four diffeent groups. After implantation, one drop of Ringer's solution was added to each defect. The periosteum and skin were repositioned and closed with wound clips. Each animal received an intramuscular injection of ~200 µl buprenorphine and ~200 µl penicillin post-surgery. All animals were monitored daily for the condition of the surgical wound, food intake, activity and clinical signs of infection. After 6 or 12 weeks, the animals were sacrificed by CO_2 inhalation, and the calvarial defect sites with surrounding bone and soft tissue were harvested for subsequent evaluations.

2.4. HISTOLOGICAL PROCESSING

Harvested calvarial samples were fixed in a 10% formaldehyde solution for five days. The samples were cut into half after being washed with deionized water. Half of the sample was for paraffin embedding, and the other half was for poly (methyl methacrylate) (PMMA) embedding. The paraffin-embedded samples were decalcified in

14 wt% ethylenediaminetetraacetic acid (EDTA, Sigma-Aldrich, USA) for 2 weeks, dehydrated in ethanol, and then embedded in paraffin using standard histological techniques. These samples were sectioned using a microtome. The thickness of the tissue section with paraffin was 5 μm. These slices were then stained with hematoxylin and eosin (H&E) [20]. Without decalcification, the samples for PMMA embedding were dehydrated in ethanol and embedded in PMMA. These samples were sectioned, affixed to acrylic slices, and ground to a thickness down to 50 μm using a micro-grinding system (EXAKT 400CS, Norderstedt, Germany). The von Kossa staining was used to observe mineralization [21].

2.5. HISTOMORPHOMETRIC ANALYSIS

Histomorphometric analysis was carried out using optical images of stained sections and Image J software (National Institutes of Health, USA). The percentage of new bone formed in a calvarial defect was evaluated from the H&E stained sections. The newly formed bone was identified by outlining the edge of the defect, with the presence of old and new bone being identified by lamellar and woven bone, respectively. The total defect area was measured from one edge of the old calvarial bone, including the entire implant and tissue within it, to the other edge of the old bone. The newly formed bone within this area was then outlined and measured; the amount of the new bone was expressed as a percentage of the total defect area. The amount of von Kossa positive area is shown as a percent of the total defect area.

2.6. STATISTICAL ANALYSIS

Measurements of the percentage of new bone (relative to the entire defect area) are expressed as a mean ± SD. Analysis for differences between groups was performed using one-way analysis of variance (ANOVA) followed by the Tukey's post hoc test; the differences were considered significant at $p < 0.05$.

3. RESULTS

3.1. GEOMETRY OF THE CLOSED AND OPEN CDHA MICROSPHERES

The closed CDHA microspheres were prepared by converting glass microspheres in a phosphate solution. The diameters of the starting glass microspheres were either ϕ106-150 μm or ϕ212-250 μm. After conversion, changes in the diameter of the microspheres were negligible. The SEM images revealed a spherical shape for the closed CDHA microspheres with two size ranges: ϕ106-150 μm (hereafter, small size; Figure 1A1 and A2) and ϕ212-250 μm (thereafter, large size; Figure 1C1 and C2). Open CDHA microspheres were sectioned from closed CDHA microspheres using a microtone. The SEM images confirmed successful formation of hemispherical open CDHA microspheres with both sizes (Figure 1B1, B2, D1 and D2). The hollow microspheres have a hollow core with a diameter of about 60% of the overall microsphere diameter. The shell wall consists of two distinct layers: a denser external layer, about ~ 5 μm thick, and a more porous internal layer. Figure 2 shows representative high-resolution images of the inner and outer surfaces of open microspheres. The outer surfaces consist of uniform

distributions of nanoparticles, and the inner surfaces appear to have rougher agglomerations of similar nanoparticles.

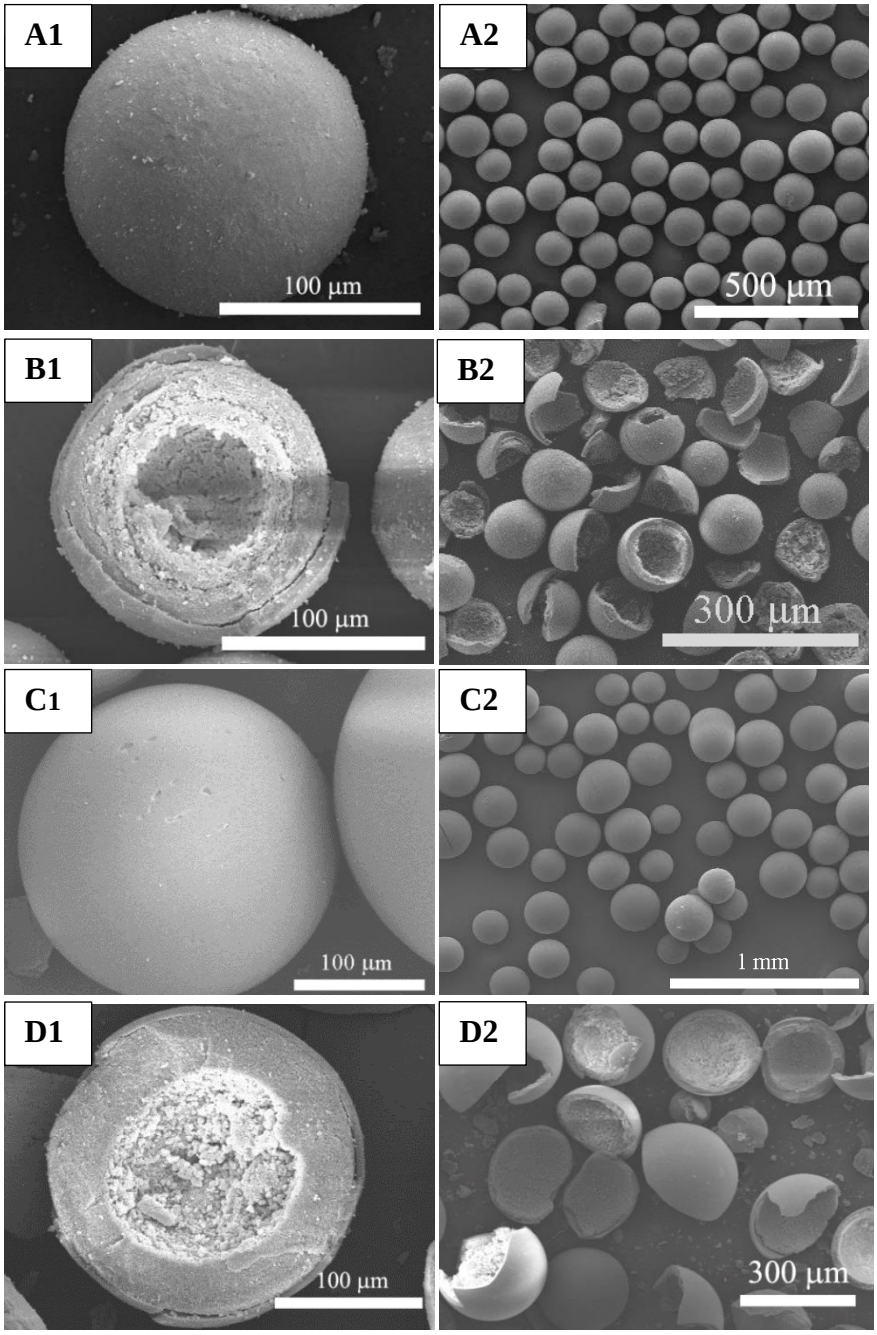

Figure 1. SEM images of 106-150 µm closed CDHA microspheres (A1, A2) and open CDHA microspheres (B1, B2) and 212-250 µm closed CDHA microspheres (C1, C2) and open CDHA microspheres (D1, D2).

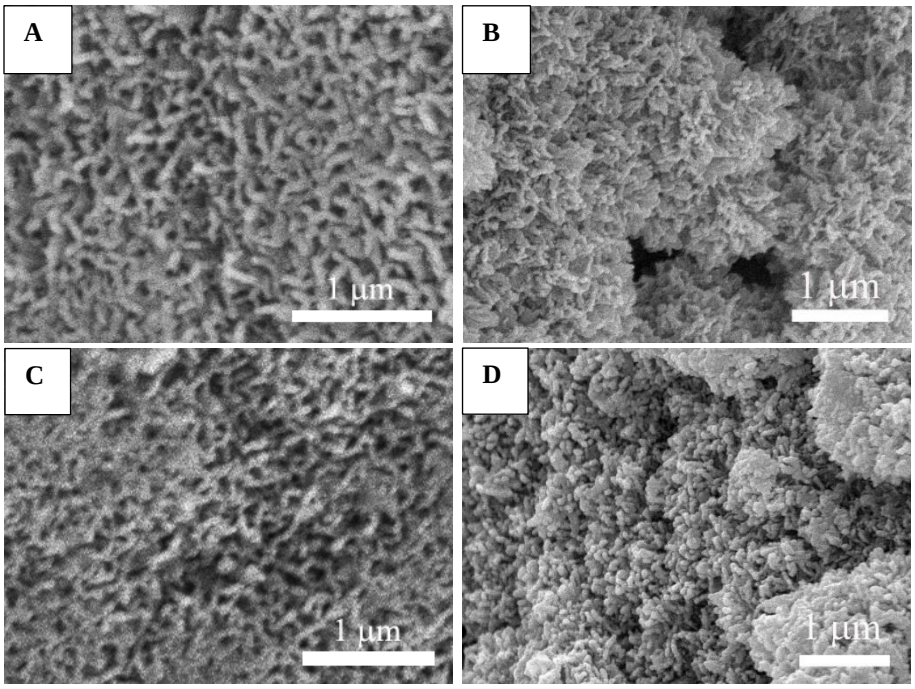

Figure 2. SEM images of an external surface (A) and internal surface (B) from a 106-150 μm open CDHA microsphere, and an external surface (C) and internal surface (D) of a 212-250 μm open CDHA microsphere.

Table 2. Surface area and average pore size of closed 106-150 μm and 212-250μm CDHA microspheres.

HA microspheres	Surface area (m^2/g)	Average pore size (nm)
106-150 μm	101	13
212-250 μm	168	10

The BET surface area and average pore size of the two sets of closed CDHA microspheres are summarized in Table 2. The surface areas of small and large closed CDHA microspheres were 101 m^2/g and 168 m^2/g, respectively. The average pore sizes of small and large closed CDHA microspheres were 13 nm and 10 nm, respectively. The

surface area was greater in the large CDHA microspheres, whereas the average pore size was greater in the small CDHA microspheres.

3.2. COMPOSITION OF THE CLOSED AND OPEN CDHA MICROSPHERES

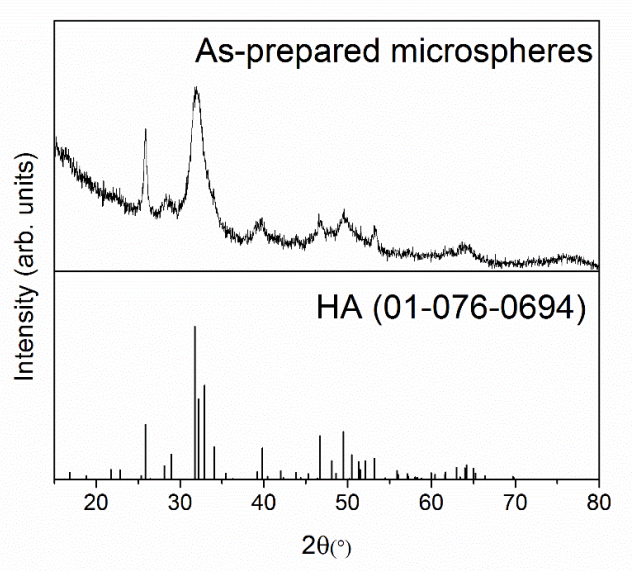

Figure 3. X-ray diffraction pattern of CDHA microspheres prepared by glass conversion technique. The pattern of a reference hydroxyapatite (HA, 01-076-0694) is also shown.

The board peak in XRD pattern of CDHA (Figure 3) indicated that the materials is poorly crystallized, or nanocrystal, or a combination of both. High-resolution cross-sectional SEM images of representative hollow CDHA microspheres are shown in Figure 4. The shell walls of the microspheres were divided into three regions: external layer, middle layer and inner layer. The Ca/P atomic ratio at the midpoint of each region was analyzed by EDS (Table 3). There was no significant difference between the Ca/P ratios

within the three regions or between the two size ranges of CDHA microspheres (n=10, p>0.05). The Ca/P atomic ratio of stoichiometric hydroxyapatite is 1.67.

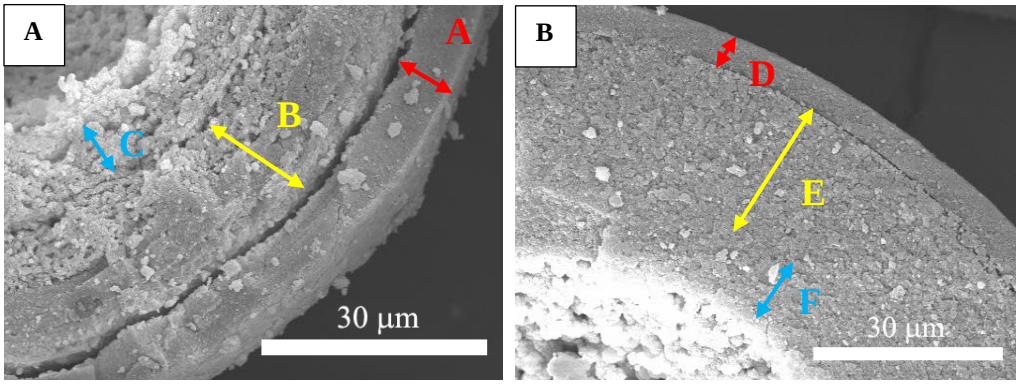

Figure 4. SEM images of cross section of 106-150 µm open CDHA microspheres (A) and 212-250µm open CDHA microspheres (B).

Table 3. Ca/P atomic ratio (n = 10; mean ± SD) for the three layers that constitute the walls of hollow CDHA microspheres.

CDHA microspheres	Cross-sectional zone	Ca/P atomic ratio
106-150 µm	Surface layer (A) Middle layer (B) Inner layer (C)	1.63 ± 0.11 1.63 ± 0.11 1.60 ± 0.14
212-250 µm	Surface layer (D) Middle layer (E) Inner layer (F)	1.67 ± 0.10 1.63 ± 0.08 1.63 ± 0.06

3.3. EVALUATION OF BONE REGENERATION IN RAT CALVARIAL DEFECTS

H&E and von Kossa stained sections of the implants with closed and open hollow CDHA microspheres after 6 weeks in rat calvarial defects are shown in Figures 5 and 6. Bone regeneration was limited and confined mainly to the edge of the defects and some

bone bridging along the bottom of implants. Fibrous tissues (light blue in H&E stained sections) filled the space between the microspheres. New bone formation in the implants with the smaller closed and open CDHA microspheres was 12 ± 3% and 17 ± 6%, respectively (Figure 5 and Table 4). The von Kossa positive areas in in the implants with the smaller closed and open CDHA microspheres were 41 ± 3% and 49 ± 5%, respectively (Table 5). The percentages of new bone in the implants with the larger closed and open CDHA microspheres were 6 ± 2 % and 12 ± 3%, respectively (Figure 6). The von Kossa positive areas in the implants with the larger size of closed and open CDHA microspheres were 30 ± 3% and 35 ± 3%, respectively. Open CDHA microspheres showed significant improvement in bone regeneration compared with closed CDHA microspheres for both size ranges at 6 weeks in rat calvarial defects ($n = 5$, $p < 0.05$ for both sizes, Figures 9 and 10). Smaller closed CDHA microspheres showed a significant increase in bone regeneration than the larger closed CDHA microspheres ($n = 5$, $p < 0.05$). Based on the H&E results, there was a borderline difference in new bone formation between the two size ranges of open CDHA microspheres ($n = 5$, $p = 0.050$). However, based on von Kossa results, the smaller open CDHA microspheres showed a significant enhancement in bone growth compared to the larger open CDHA microspheres ($n = 5$, $p < 0.001$).

Higher magnification images of the closed and open HA microspheres are shown in Figure 5C and D (from the boxed areas of Figure 5A1 and A2) and Figure 6C and D (from the boxed areas in Figure 6A1 and A2). For the closed HA microspheres with both size ranges, little bone formation was noted, fibrous tissue filled the pore spaces between the closed CDHA microspheres and infiltrated into the hollow cores of some broken

closed HA microspheres. In comparison, more bone regeneration was observed in the micro-concavity of open CDHA microspheres (indicated by blue arrows) in both sizes (ϕ106-150 μm and ϕ212-250 μm).

The outcomes from the implants with the closed and open CDHA microspheres of the two size ranges after 12 weeks in rat calvarial defects are shown in Figures 7 and 8. New bone tissue formed from the edge of the defects and on the bottom of the implants. For the open CDHA microspheres, more new bone growth in the micro-concavities can be found; the remaining open CDHA microspheres can be observed in the new bone bridging the ends of defects. For the smaller closed and open CDHA microspheres (Figure 7), the percentages of new bone formation were 26 ± 8% and 49 ± 7%, respectively; the von Kossa positive areas were 55 ± 5% and 76 ± 4%, respectively. For the larger closed and open CDHA microspheres (Figure 8), the percentages of new bone were 30 ± 9% and 40 ± 8%, respectively; the von Kossa positive areas were 56 ± 5% and 65 ± 5%, respectively. The open CDHA microspheres showed significant improvement in bone regeneration when compared to the closed CDHA microspheres, for both size ranges, after 12 weeks in rat calvarial defects ($n = 5$, $p < 0.001$ for small size; $n = 5$, $p < 0.05$ for large size). There was no significant difference in new bone formation between the two size ranges for the closed CDHA microspheres ($n = 5\sim10$, $p > 0.05$). However, smaller open CDHA microspheres showed a more significant increase in bone regeneration than larger open CDHA microspheres ($n = 5$, $p < 0.05$). Bone regeneration was time-dependent for both size ranges; new bone formation increased significantly from 6 weeks to 12 weeks in rat calvarial defects ($n = 5$, $p < 0.001$ for closed CDHA microspheres; $n = 5\sim10$, $p < 0.001$ for open CDHA microspheres).

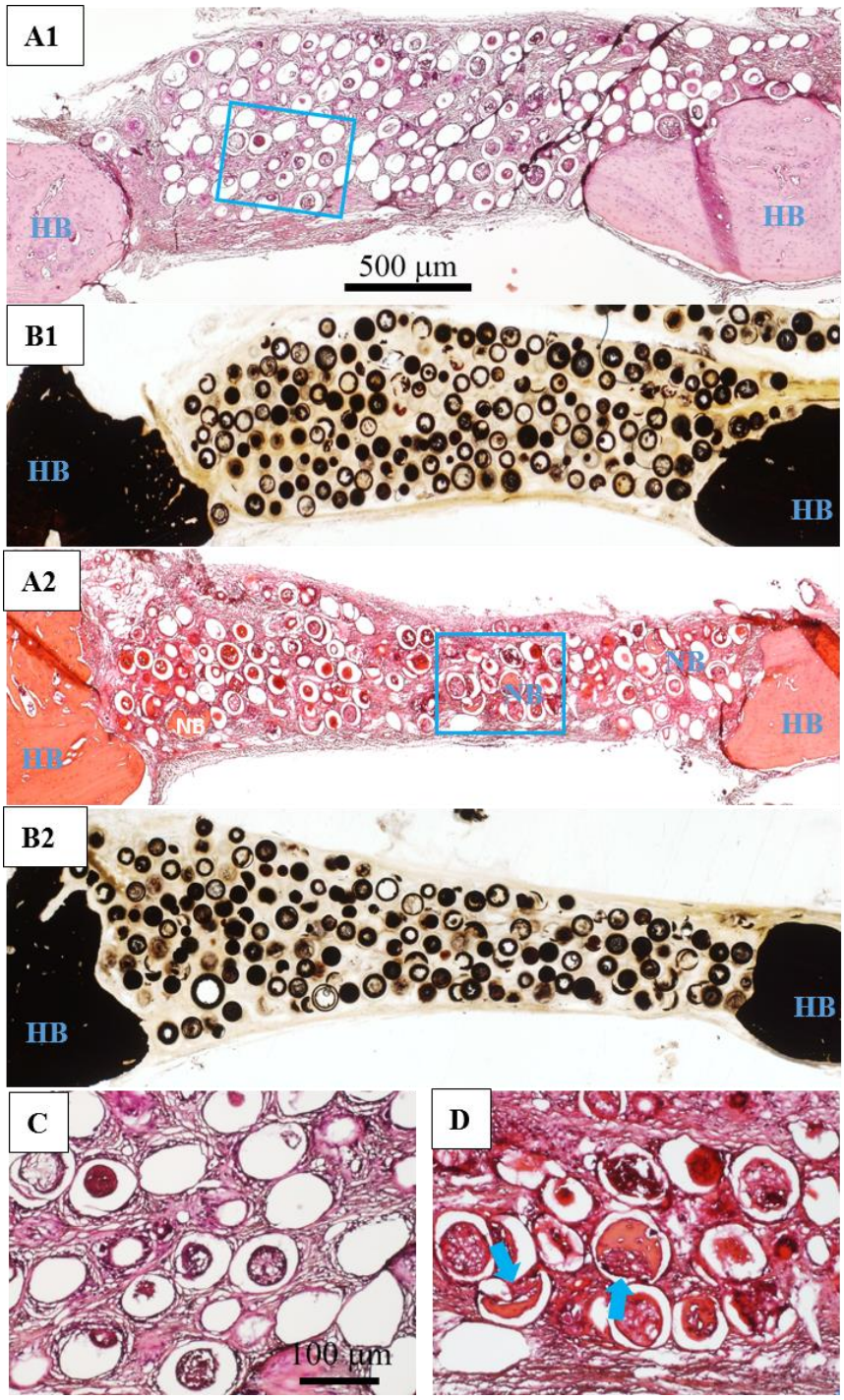

Figure 5. H&E stained and von Kossa sections of implants composed of closed (A1, B1) and open (A2, B2) CDHA microspheres (ϕ106-150 μm) after 6 weeks in rat calvarial defects; (C, D) higher-magnification images of boxed area in (A1, A2). HB: host bone; NB: new bone. Blue arrow: new bone growth in micro-concavity.

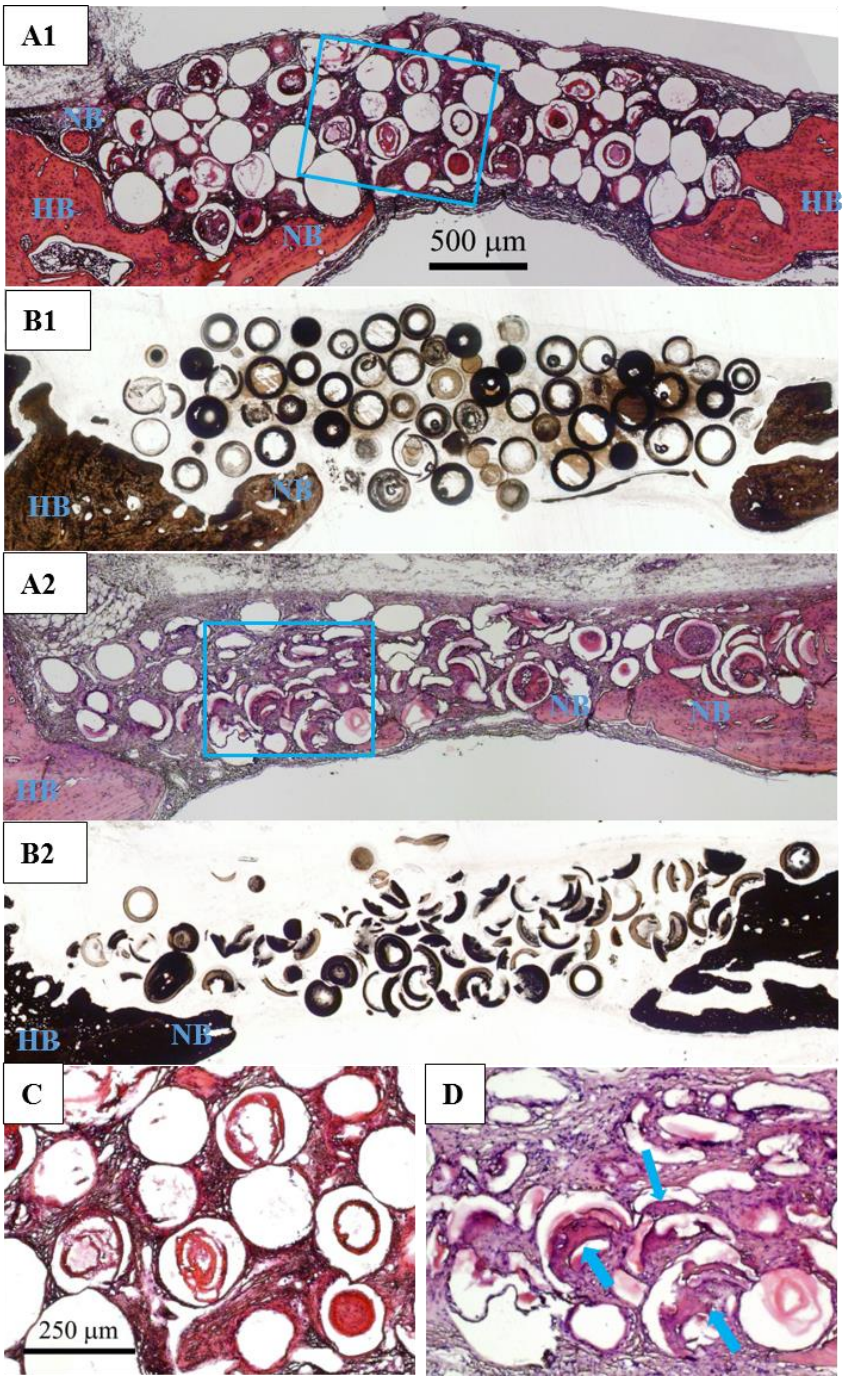

Figure 6. H&E and von Kossa stained sections of implants composed of closed (A1, B1) and open (A2, B2) CDHA microspheres (ϕ212-250 μm) after 6 weeks in rat calvarial defects; (C, D) higher-magnification images of boxed area in (A1, A2). HB: host bone; NB: new bone. Blue arrow: new bone growth in micro-concavity.

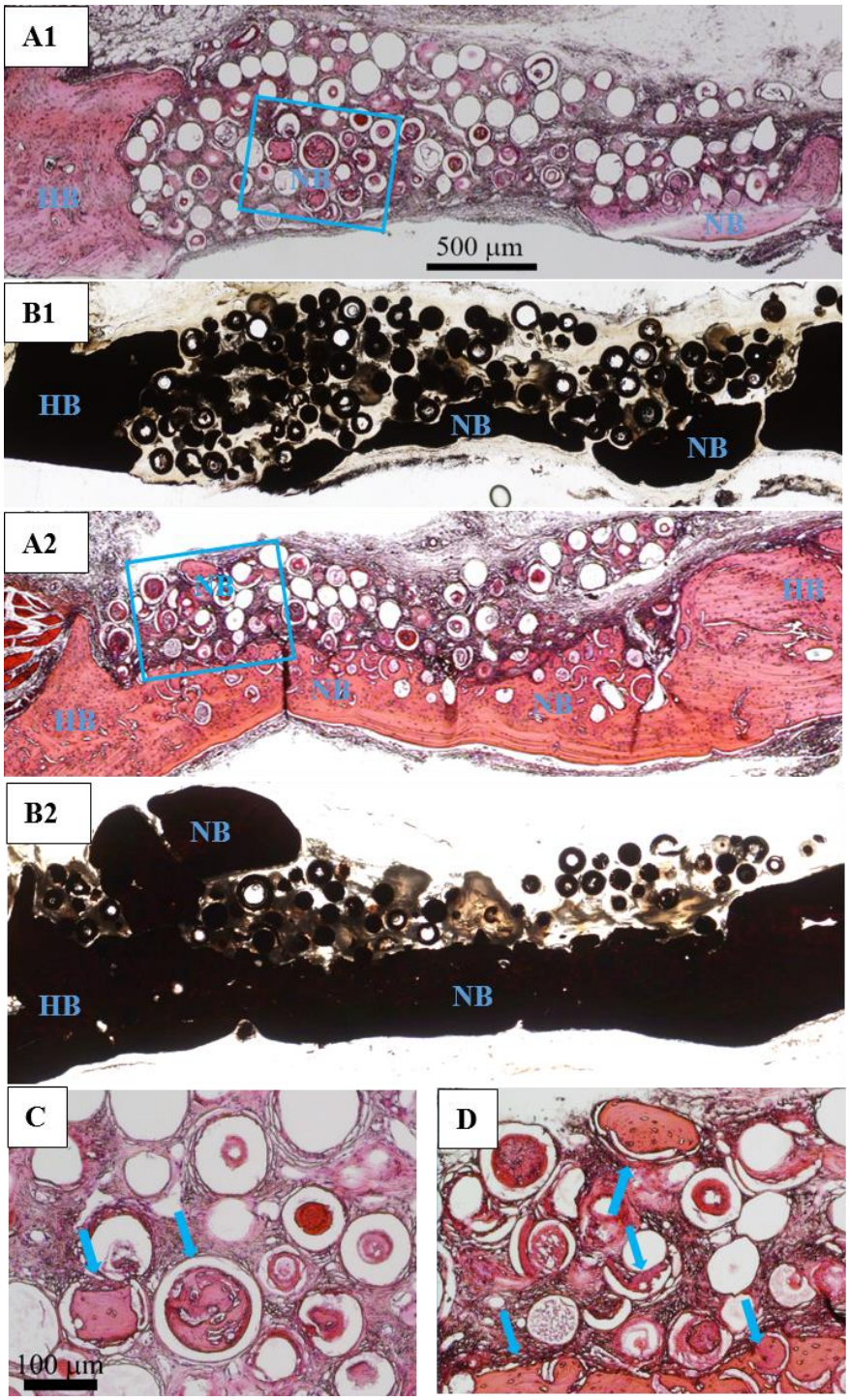

Figure 7. H&E and von Kossa stained sections of implants composed of closed (A1, B1) and open (A2, B2) CDHA microspheres (ϕ106-150 μm) after 12 weeks in rat calvarial defects; (C, D) higher-magnification images of boxed area in (A1, A2). HB: host bone; NB: new bone. Blue arrow: new bone growth in micro-concavity.

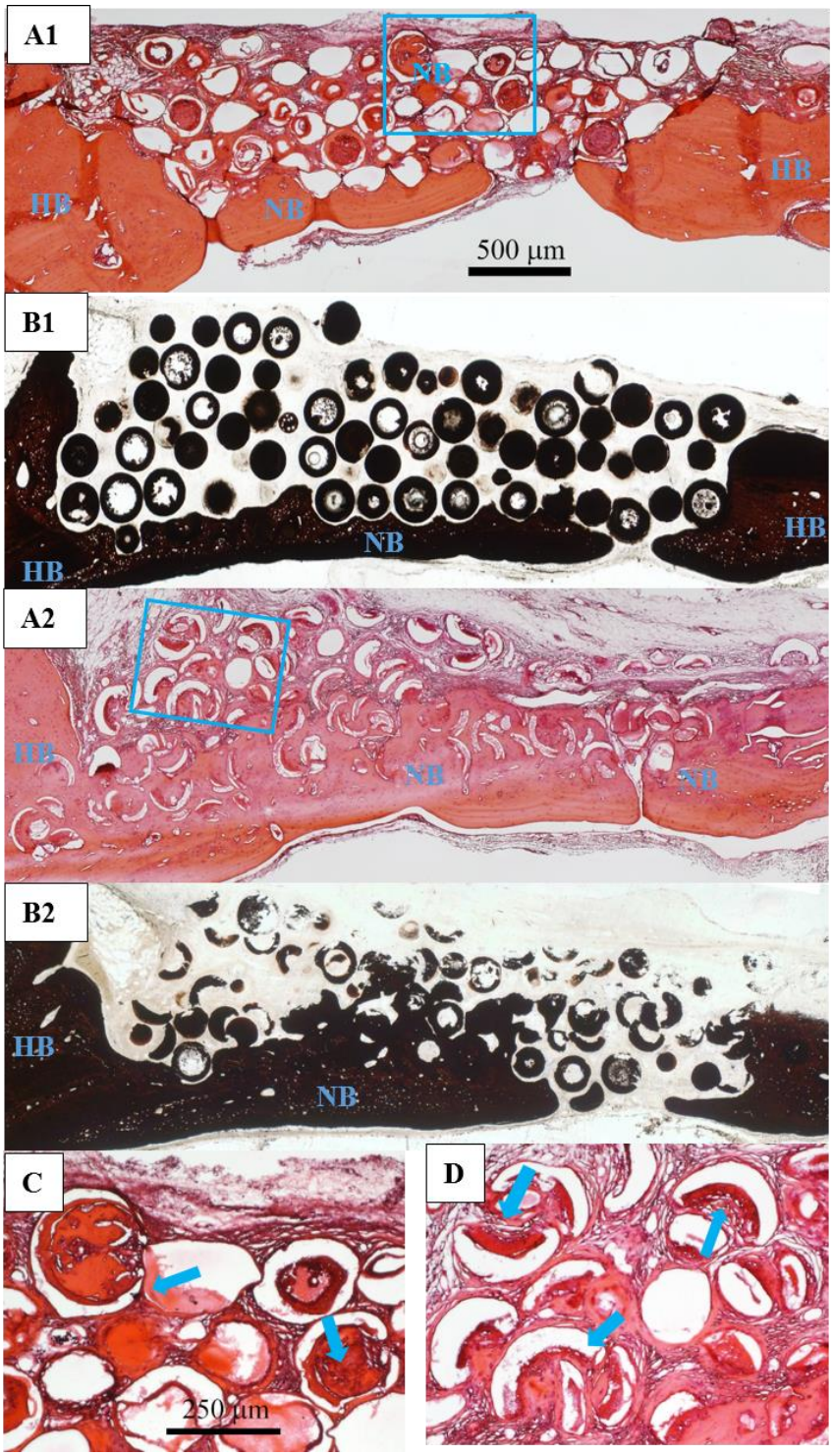

Figure 8. H&E and von Kossa stained sections of implants composed of closed (A1, B1) and open (A2, B2) CDHA microspheres (ϕ212-250 μm) after 12 weeks in rat calvarial defects; (C, D) higher-magnification images of boxed area in (A1, A2). HB: host bone; NB: new bone. Blue arrow: new bone growth in micro-concavity.

Table 4. Comparative new bone formation in all implants after 6 or 12 weeks based on H&E staining. The amount of new bone is expressed as a percent of the total defect area (mean ± SD).

CDHA microspheres		New bone (%)	
		6 weeks	12 weeks
ϕ106-150 μm	Closed	12 ± 3	26 ± 8
	Open	17 ± 6	49 ± 7
ϕ212-250 μm	Closed	6 ± 2	30 ± 9
	Open	12 ± 3	40 ± 8

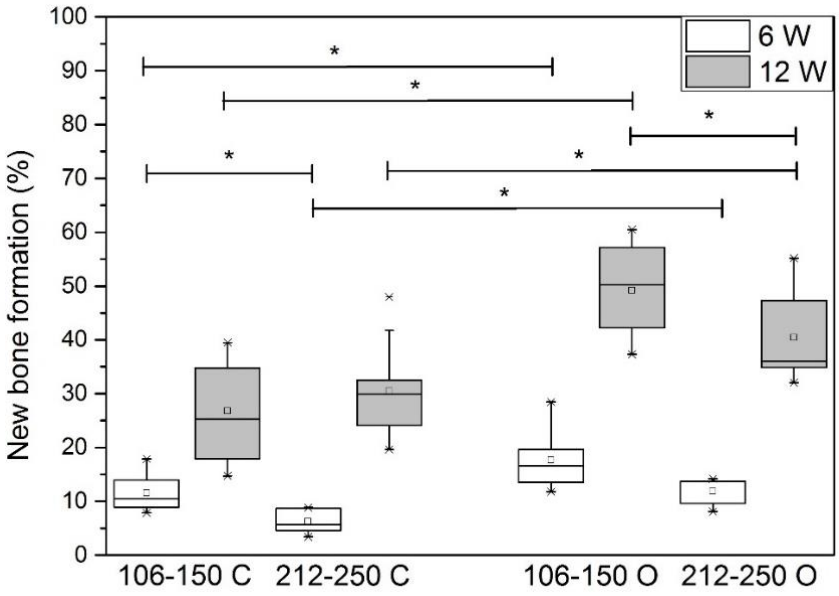

Figure 9. Comparative new bone formation in implants with closed and open CDHA microspheres with diameter of 106-150 μm or 212-250 μm after 6 weeks (6 W) and 12 weeks (12 W) in rat calvarial defects (Mean ± SD; n = 5~10, * significant difference between groups; $p < 0.05$).

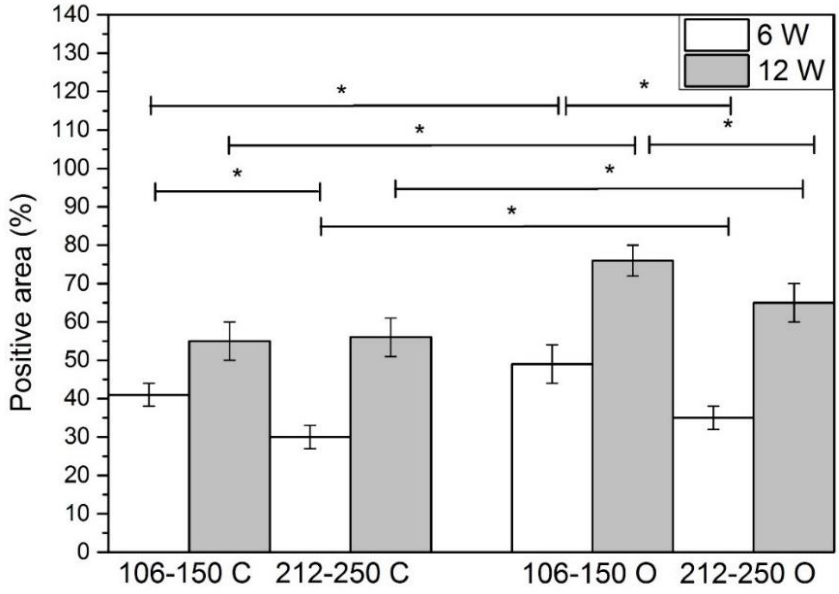

Figure 10. Comparative von Kossa positive area for implants of closed and open CDHA microspheres with diameter of 106-150 μm or 212-250 μm after 6 weeks (6 W) and 12 weeks (12 W) in rat calvarial defects (Mean ± SD; n = 5~10, * significant difference between groups; $p < 0.05$).

A comparison of closed and open HA microspheres in both sizes at 12 weeks is shown in higher magnified images in Figure 6C and D (from the boxed areas of Figure 6A1 and A2) and Figure 7C and D (from the boxed areas of Figure 7A1 and A2). Bone regeneration in the cores of some broken closed CDHA microspheres was identified. A higher degree of new bone formation in the micro-concavity of open CDHA microspheres was observed.

4. DISCUSSION

The ability of CDHA microspheres to regenerate bone can presumably be affected by the differences between closed and open CDHA microspheres in microstructure. In

this study, the microstructure of closed and open CDHA microspheres in two size ranges (ϕ106-150 μm vs. ϕ212-250 μm) were analyzed. To test CDHA microspheres in facilitating bone regeneration, rat calvarial defects were created and CDHA microspheres were implanted. Bone regeneration was evaluated in weeks 6 & 12.

For both size ranges, the thickness of the denser (outer) layer was ~ 5 μm, while the ratio of the hollow core diameter to the microsphere diameter is ~0.6. The factors leading to these two distinct layers are still unclear. In the glass conversion process [17, 22-24], ions are released from the soluble glass (i.e., Ca^{2+}, Li^{+}, B^{3+}) to the aqueous phosphate solution. When the concentration of Ca^{2+} ions exceeds the local solubility limit, those ions react with phosphate anions solution to form calcium phosphate. As the glass dissolves, the calcium phosphate layer continues to thicken until the glass is completely converted to calcium phosphate. The kinetics and mechanism of the formation of the calcium phosphate layer in borate glass have been investigated in several studies [23, 25-27]. The conversion rate is initially described by a reaction-controlled model (linear kinetics); however, at the later stage, a three-dimensional diffusion model (parabolic kinetics) better explains the conversion rate. Presumably, the denser outer layer and porous inner layers result from these two kinetic models. Additional experiments can be set-up to further investigate the dynamic changes of SSA and pore size.

The *in vivo* experiments showed that the open CDHA microspheres were effective in promoting bone formation. For both size ranges of the open CDHA microspheres, new bone formation was observed in both 6 weeks and 12 weeks post-implantation. The amount of new bone growth increased from 6 weeks to 12 weeks. In the study of 12-

week implantation with small microspheres, new bone formation with the implants of open microsphere was about twice that of the closed microspheres; for large microspheres, new bone formation in the implants of open microspheres was about 30% higher than that of the closed microspheres. Thus, the open microspheres were more effective in facilitating bone regeneration than the closed microspheres. Compared to the closed microsphere, the open microsphere had a micro-concave region with a more porous and rougher surface (see Figures 1 and 2). These characters (i.e., micro-concavity, porosity, roughness) could contribute to the difference in bone regeneration between the closed and open microspheres.

The effectiveness of micro-concave surfaces in promoting bone regeneration has been investigated by others [28-33]. For example, substantial mineralization was observed within the concavities, but not at the planar surfaces, of calcium phosphate ceramic discs in simulated body fluid, and smaller concavities (0.4 mm diameter) induced more mineralization than larger concavities (0.8 mm or 1.8 mm diameter) [32]. An *in vivo* study demonstrated that concavities stimulated the formation of blood vessels, a critical process for bone formation [33]. Stem cells showed better outcomes on a concave surface than a flat surface in terms of cell maturation, osteodifferentiation, and specific protein production [29]. Bone formation by intramembranous ossification was favored on a concave surface as well [31]. Concavity is also conducive to the accumulation of growth factors such as BMPs [28]. Differences in microstructure may also be a contributing factor to the outcome of bone regeneration. The internal concave surface was more porous and rougher compared to external convex surface (Figure 2).

The differences in porosity and roughness could influence dissolution/degradation of biomaterials, adsorption of growth factors, and mineral deposition from body fluids [34-41]. For instance, the degradation of a porous surface could lead to faster Ca^{2+} release which is a key factor in facilitating angiogenesis [42]. Further, a more porous and rougher surface could be a more suitable substrate for adsorption of biologically active molecules, such as BMPs and growth factors. Together, these lead to enhanced cell attachment, proliferation and differentiation.

Dissolution/degradation rates of calcium phosphates have been shown to be affected by the ratio of Ca/P of the material [43-45]. For example, the dissolution rate of a calcium phosphate in water increased as the Ca/P ratio decreased [43]. Higher dissolution/degradation of HA could release more Ca^{2+} and phosphate ions, which could facilitate bone regeneration. It is possible that the Ca/P ratio of the CDHA can be manipulated to achieve varying degree of dissolution. In this study, there was no significant difference in Ca/P ratio within the three regions or between the two size ranges of CDHA microspheres.

The current study demonstrated that the small open microspheres induced a more significant increase in bone regeneration than the large open microspheres at both 6 weeks and 12 weeks. One reason for this difference may be attributed to the greater total surface area made available by the open microspheres for cell attachment. For equivalent masses of particles, there will be nearly twice as much available surface area for the open particles compared to the closed particles. Another reason for the difference in bone regeneration could be due to the inner surface curvature of the open microspheres. The small microspheres have higher curvature than the large microspheres. It remains to be

investigated how the curvature of the microspheres affect cellular physiology leading to the differential outcome of bone regeneration.

An apparent observation is that new bone formation with implants of the small open microspheres was able to completely bridge the defects at the bottoms of all the implants (Figure 7). In comparison, few of the defects with closed microspheres were bridged. During the regeneration process, new bone formation started from the edge of the host bone and from the bottom of the defect (dura matter), where osteogenic cells and blood supply were abundant. The open microspheres might absorb the osteogenic factors by diffusion or fluid transport and trigger bone growth in the micro-concavity. The open microspheres at the bottom of the implants had the best chance of contact with the osteogenic factors not only from dura matter but also from the edges induced by the open microsphere in periphery.

In the present study, the smaller (ϕ106-150 μm) open CDHA microspheres promoted more new bone formation than the larger open microspheres (ϕ212-250 μm) in rat calvarial defects. However, the optimum size of the open microspheres still needs to be determined. Furthermore, the open CDHA microspheres with high surface area could be applied as a device for protein/drug delivery and should be evaluated in future studies. Overall, this study demonstrated that open CDHA microspheres have better capacity to enhance bone formation than the closed CDHA microspheres, and their efficiency to simulate bone regeneration depends on particle size.

5. CONCLUSIONS

The open CDHA microspheres significantly enhance bone regeneration compared to the closed CDHA microspheres at both 6 weeks and 12 weeks in rat calvarial defects. Compared with the larger size of open CDHA microspheres (smaller curvature), the smaller size of open CDHA microspheres (larger curvature) resulted in a more significant increase in bone regeneration. The differences in the microstructures of the CDHA microspheres (i.e., curvature, concavity, porosity, surface roughness, total surface area available for cell attachment) may deserve future attention.

ACKNOWLEDGEMENTS

The work was financially supported by the National Institutes of Health [Grant #1R15DE023987-01]. We appreciate the technical support of members of the Missouri S&T Materials Research Center and the Department of Biological Sciences, and the assistance of Richard Watters of the Animal Research Facility.

REFERENCES

[1] V. Campana, G. Milano, E. Pagano, M. Barba, C. Cicione, G. Salonna, W. Lattanzi, and G. Logroscino, *Bone substitutes in orthopaedic surgery: from basic science to clinical practice.* Journal of Materials Science: Materials in Medicine, 2014. **25**(10): p. 2445-2461.

[2] F. Deschaseaux, L. Sensébé, and D. Heymann, *Mechanisms of bone repair and regeneration.* Trends in Molecular Medicine, 2009. **15**(9): p. 417-429.

[3] F. Loi, L.A. Córdova, J. Pajarinen, T.-h. Lin, Z. Yao, and S.B. Goodman, *Inflammation, fracture and bone repair.* Bone, 2015. **86**: p. 119-130.

[4] I.H. Kalfas, *Principles of bone healing.* Neurosurg Focus, 2001. **10**(4): p. E1.

[5] A. Scarano, M. Degidi, G. Iezzi, G. Pecora, M. Piattelli, G. Orsini, S. Caputi, V. Perrotti, C. Mangano, and A. Piattelli, *Maxillary sinus augmentation with different biomaterials: a comparative histologic and histomorphometric study in man.* Implant dentistry, 2006. **15**(2): p. 197-207.

[6] L. Trombelli, *Which reconstructive procedures are effective for treating the periodontal intraosseous defect?* Periodontology 2000, 2005. **37**(1): p. 88-105.

[7] R.T. Kao, G. Conte, D. Nishimine, and S. Dault, *Tissue engineering for periodontal regeneration.* Journal of the California Dental Association, 2005. **33**(3): p. 205-215.

[8] N. Pandit, R. Malik, and D. Philips, *Tissue engineering: A new vista in periodontal regeneration.* Journal of Indian Society of Periodontology, 2011. **15**(4): p. 328-337.

[9] C. Dahlin, A. Johansson, a. Sahlgrenska, S.f.A.B. Institute of Clinical Sciences, D.o.B. Orthopaedics, u. Göteborgs, U. Gothenburg, s.f.a.b.o.o.A.f.b. Institutionen för kliniska vetenskaper, and A. Sahlgrenska, *Iliac crest autogenous bone graft versus alloplastic graft and guided bone regeneration in the reconstruction of atrophic maxillae: a 5-year retrospective study on cost-effectiveness and clinical outcome.* Clinical Implant Dentistry and Related Research, 2011. **13**(4): p. 305-310.

[10] P.V. Giannoudis, H. Dinopoulos, and E. Tsiridis, *Bone substitutes: an update.* Injury, 2005. **36**(3): p. S20-S27.

[11] J.A. McAuliffe, *Bone graft substitutes.* Journal of Hand Therapy, 2003. **16**(2): p. 180-187.

[12] O. Reikerås, H. Shegarfi, C. Naper, F.P. Reinholt, and B. Rolstad, *Impact of MHC mismatch and freezing on bone graft incorporation: An experimental study in rats.* Journal of Orthopaedic Research, 2008. **26**(7): p. 925-931.

[13] A. Von Recum and J.E. Jacobi, *Handbook of biomaterials evaluation: scientific, technical, and clinical testing of implant materials*. 1999, Taylor & Francis: Philadelphia, PA.

[14] H. Fu, M.N. Rahaman, and D.E. Day, *Effect of process variables on the microstructure of hollow hydroxyapatite microspheres prepared by a glass conversion method.* Journal of the American Ceramic Society, 2010. **93**(10): p. 3116-3123.

[15] H. Fu, M.N. Rahaman, R.F. Brown, and D.E. Day, *Evaluation of bone regeneration in implants composed of hollow HA microspheres loaded with transforming growth factor β1 in a rat calvarial defect model.* Acta Biomaterialia, 2013. **9**(3): p. 5718-5727.

[16] W. Xiao, H. Fu, M.N. Rahaman, Y. Liu, and B.S. Bal, *Hollow hydroxyapatite microspheres: A novel bioactive and osteoconductive carrier for controlled release of bone morphogenetic protein-2 in bone regeneration.* Acta Biomaterialia, 2013. **9**(9): p. 8374-8383.

[17] H. Fu, *Hollow hydroxyapatite microspheres as devices for controlled delivery of proteins and as scaffolds for tissue engineering*. Doctoral Dissertations, Missouri University of Science and Technology, 2012.

[18] M.N. Rahaman, W. Xiao, Y. Liu, and B. Sonny Bal, *Osteoconductive and Osteoinductive Implants Composed of Hollow Hydroxyapatite Microspheres*, in *Advances in Bioceramics and Porous Ceramics VII*. 2014, John Wiley & Sons, Inc: Hoboken, NJ, USA. p. 65-79.

[19] E.P. Barrett, E.P. Barrett, L.G. Joyner, L.G. Joyner, P.P. Halenda, and P.P. Halenda, *The determination of pore volume and area distributions in porous substances. I. Computations from nitrogen isotherms.* Journal of the American Chemical Society, 1951. **73**(1): p. 373-380.

[20] J.Q. Feng, J. Zhang, S.L. Dallas, Y. Lu, S. Chen, X. Tan, M. Owen, S.E. Harris, and M. Macdougall, *Dentin matrix protein 1, a target molecule for cbfa1 in bone, ss a unique bone marker gene.* Journal of Bone and Mineral Research, 2002. **17**(10): p. 1822-1831.

[21] L.F. Bonewald, S.E. Harris, J. Rosser, M.R. Dallas, S.L. Dallas, N.P. Camacho, B. Boyan, and A. Boskey, *Von Kossa staining alone is not sufficient to confirm that mineralization in vitro represents bone formation.* Calcified Tissue International, 2003. **72**(5): p. 537-547.

[22] K.P. Fears, *Formation of hollow hydroxyapatite microspheres*. Masters Theses, Missouri University of Science and Technology, 2001.

[23] G.H. Nancollas and J. Zhang, *Formation and dissolution mechanisms of calcium phosphates in aqueous systems*, in *Hydroxyapatite and related materials*, P.W. Brown and B. Constantz, Editors. 1994, CPC Press, Inc.: United State of America. p. 73-81.

[24] Q. Wang, W. Huang, D. Wang, B.W. Darvell, D.E. Day, and M.N. Rahaman, *Preparation of hollow hydroxyapatite microspheres.* Journal of Materials Science: Materials in Medicine, 2006. **17**(7): p. 641-646.

[25] Y. Gu, W. Xiao, L. Lu, W. Huang, M.N. Rahaman, and D. Wang, *Kinetics and mechanisms of converting bioactive borate glasses to hydroxyapatite in aqueous phosphate solution.* Journal of Materials Science, 2011. **46**(1): p. 47-54.

[26] W. Huang, M.N. Rahaman, D.E. Day, and Y. Li, *Mechanisms for converting bioactive silicate, borate, and borosilicate glasses to hydroxyapatite in dilute phosphate solution.* Physics and Chemistry of Glasses-European Journal of Glass Science and Technology Part B, 2006. **47**(6): p. 647-658.

[27] A.-H. Yao, J. Lin, X. Duan, and W.-H. Huang, *Formation mechanism of multilayered structure on surface of bioactive borosilicate glass.* Chinese Journal of Inorganic Chemistry, 2008. **24**(7): p. 1132-1136.

[28] U. Ripamonti, *Functionalized Surface Geometries Induce:"Bone: Formation by Autoinduction".* Frontiers in physiology, 2018. **8**: p. 1084.

[29] A. Graziano, R. d'Aquino, M.G. Cusella-De Angelis, G. Laino, A. Piattelli, M. Pacifici, A. de Rosa, and G. Papaccio, *Concave Pit-Containing Scaffold Surfaces Improve Stem Cell-Derived Osteoblast Performance and Lead to Significant Bone Tissue Formation.* PLoS ONE, 2007. **2**(6): p. e496.

[30] C. Gray, A. Boyde, and S. Jones, *Topographically induced bone formation in vitro: implications for bone implants and bone grafts.* Bone, 1996. **18**(2): p. 115-123.

[31] M.J. Coathup, K.A. Hing, S. Samizadeh, O. Chan, Y.S. Fang, C. Campion, T. Buckland, and G.W. Blunn, *Effect of increased strut porosity of calcium phosphate bone graft substitute biomaterials on osteoinduction.* Journal of Biomedical Materials Research Part A, 2012. **100A**(6): p. 1550-1555.

[32] M. Bianchi, E.R. Urquia Edreira, J.G.C. Wolke, Z.T. Birgani, P. Habibovic, J.A. Jansen, A. Tampieri, M. Marcacci, S.C.G. Leeuwenburgh, and J.J.J.P. van den Beucken, *Substrate geometry directs the in vitro mineralization of calcium phosphate ceramics.* Acta Biomaterialia, 2014. **10**(2): p. 661-669.

[33] A. Scarano, V. Perrotti, L. Artese, M. Degidi, D. Degidi, A. Piattelli, and G. Iezzi, *Blood vessels are concentrated within the implant surface concavities: a histologic study in rabbit tibia.* Odontology, 2014. **102**(2): p. 259-266.

[34] H. Yuan, Z. Yang, Y. Li, X. Zhang, J.D. De Bruijn, and K. De Groot, *Osteoinduction by calcium phosphate biomaterials.* Journal of Materials Science: Materials in Medicine, 1998. **9**(12): p. 723-726.

[35] C.B. Danoux, D. Barbieri, H. Yuan, J.D. de Bruijn, C.A. van Blitterswijk, and P. Habibovic, *In vitro and in vivo bioactivity assessment of a polylactic acid/hydroxyapatite composite for bone regeneration.* Biomatter, 2014. **4**(1): p. e27664.

[36] S. Fujibayashi, M. Neo, H.-M. Kim, T. Kokubo, and T. Nakamura, *Osteoinduction of porous bioactive titanium metal.* Biomaterials, 2004. **25**(3): p. 443-450.

[37] E. García-Gareta, J. Hua, J.C. Knowles, and G.W. Blunn, *Comparison of mesenchymal stem cell proliferation and differentiation between biomimetic and electrochemical coatings on different topographic surfaces.* Journal of Materials Science: Materials in Medicine, 2013. **24**(1): p. 199-210.

[38] D. Barbieri, A.J.S. Renard, J.D. de Bruijn, and H. Yuan, *Heterotopic bone formation by nano-apatite containing poly (D,L-lactide) composites.* European cells & materials, 2010. **19**: p. 252-261.

[39] K.L. Kilpadi, P.-L. Chang, and S.L. Bellis, *Hydroxylapatite binds more serum proteins, purified integrins, and osteoblast precursor cells than titanium or steel.* Journal of Biomedical Materials Research, 2001. **57**(2): p. 258-267.

[40] F.B. Bagambisa and U. Joos, *Preliminary studies on the phenomenological behaviour of osteoblasts cultured on hydroxyapatite ceramics.* Biomaterials, 1990. **11**(1): p. 50-56.

[41] K.A. Hing, *Bioceramic bone graft substitutes: Influence of porosity and chemistry.* International Journal of Applied Ceramic Technology, 2005. **2**(3): p. 184-199.

[42] A. Aguirre, A. González, M. Navarro, Ó. Castaño, J.A. Planell, and E. Engel, *Control of microenvironmental cues with a smart biomaterial composite promotes endothelial progenitor cell angiogenesis.* European Cells and Materials, 2012. **24**: p. 90-106.

[43] E. Mavropoulos, A.M. Rossi, N.C.C. da Rocha, G.A. Soares, J.C. Moreira, and G.T. Moure, *Dissolution of calcium-deficient hydroxyapatite synthesized at different conditions.* Materials Characterization, 2003. **50**(2): p. 203-207.

[44] F. Driessens, *Formation and stability of calcium phosphates in relation to the phase composition of the mineral in calcified tissues*, in *Bioceramics Calcium Phosphate*. 2018, CRC Press. p. 1-32.

[45] A. Tofighi, K. Schaffer, and R. Palazzolo. *Calcium phosphate cement (CPC): a critical development path*. in *Key Engineering Materials*. 2008. Trans Tech Publ.

II. HOLLOW BIPHASIC CALCIUM PHOSPHATE MICROSPHERES FROM GLASS DISSOLUTION AND REPRECIPITATION; PART I: PARTICLE FORMATION AND CHARACTERIZATION

Youqu Shen[1], Richard K. Brow[1]

[1]Department of Materials Science and Engineering, Missouri University of Science and Technology Rolla, MO, 65409

ABSTRACT

Hollow biphasic calcium phosphate (BCP) microspheres have been prepared with different fractions of hydroxyapatite (HA) and β-tricalcium phosphate (β-TCP) and their *in vitro* reactivities determined. The microspheres were prepared by reacting soluble borate glasses in phosphate solutions (0.1 M or 0.25M K_2HPO_4) with different values of pH (7-12) to produce hollow calcium-deficient hydroxyapatite (CDHA) microspheres with Ca/P ratios that increased with solution pH. Heating the CDHA microspheres to 800°C produced hollow, nanoporous BCP microspheres with ratios of nanocrystalline HA and β-TCP that correspond to the Ca/P ratio of the CDHA precursors. CDHA particles converted in pH=7 solutions (Ca/P≈1.55) and pH=12 solutions (Ca/P≈1.59) produced BCP microspheres with β-TCP/HA=70/30 and β-TCP/HA=44/56, respectively. The CDHA microspheres reacted more quickly in acetic acid than the BCP microspheres, and for the latter, those with a greater β-TCP/HA ratio were more reactive. CDHA and BCP microspheres converted to nanocrystalline carbonated hydroxyapatite when immersed in 37°C simulated body fluid (SBF).

1. INTRODUCTION

Carbonated-hydroxyapatite, with the general formula $(Ca, Na, Mg)_{10}(PO_4, HPO_4, CO_3)_6(OH, Cl, F)_2$ [1-4], is the mineral phase in hard tissue. Because of their biocompatibility and bioactivity, synthetic calcium phosphate ceramics, including hydroxyapatite (HA, $Ca_{10}(PO_4)_6(OH)_2$) and β-tricalcium phosphate (β-TCP, $Ca_3(PO_4)_2$) are widely used as biomedical implant materials [5].

Synthetic HA is osteoconductive and produces no systemic toxicity or immunological reactions. However, HA has found limited use as an allograft or autograft implant material, principally because HA lacks the osteoinductivity and osteogenicity possessed by allografts or autografts [6-9]. In practice, mixing HA with osteogenic growth factors is often needed to achieve desirable bone regeneration [6-8]. Compared to HA, β-TCP is both osteoconductive and osteoinductive, and due to its low interfacial energy with respect to apatite, it can provoke the precipitation of an apatite layer upon incubation in aqueous ionic solutions [10]. β-TCP cannot be precipitated from aqueous solutions; instead, it forms when other phases[11], like calcium deficient hydroxyapatite [12] or mixtures of materials like dicalcium phosphate anhydrous and CaO [13], are heated above about 800°C. β-TCP can also be prepared at relatively low temperatures (~150 °C) by precipitation in water-free mediums, such as ethylene glycol [14].

Calcium phosphate microspheres can be produced by reacting Ca-containing soluble borate glass microspheres in a phosphate solution. By varying the glass composition [15], solution pH value [16], solution chemistry [17-19], and temperature [17, 20], the compositions and structures of the calcium phosphate microspheres can be

modified. For example, by adjusting the solution pH, the glass conversion process can produce semi-crystalline forms of dicalcium phosphate dehydrate (DCPD, pH=4.4), dicalcium phosphate anhydride (DCPA, pH=5.5), and calcium-deficient hydroxyapatite (pH=9.2) [16].

The objective of the present study is to create hollow biphasic calcium phosphate microspheres with controlled degradation rates and to characterize their performance *in vitro* and *in vivo*. In Part I of this study, the glass conversion process used in previous studies to produce HA microspheres from CDHA microspheres with a range of Ca/P ratios is described, as is their conversion by heat treatments to hollow BCP microspheres with a range of β-TCP/HA ratios. Compositions and phase distributions were determined by analytical scanning electron microscopy, x-ray diffraction, and Raman spectroscopy. The relative reactivity of CDHA and BCP particles, in acetic acid and in simulated body fluid (SBF), is described. In Part II [21], the results of *in vivo* implantations of CDHA and BCP microspheres in rat calvarial defects (8 weeks) and subcutaneous defects (8 and 12 weeks) are described. BCP microspheres with greater fractions of β-TCP were found to promote a greater fractions of new bone formation in the calvarial defects and new blood vessel formation in the subcutaneous defects than CDHA particles and BCP particles with lower fractions of β-TCP.

2. MATERIALS AND METHODS

2.1. PREPARATION AND CHARACTERIZATION OF HOLLOW BIPHASIC CALCIUM PHOSPHATE MICROSPHERES

A schematic diagram for making hollow CDHA and BCP microspheres is shown in Figure 1.

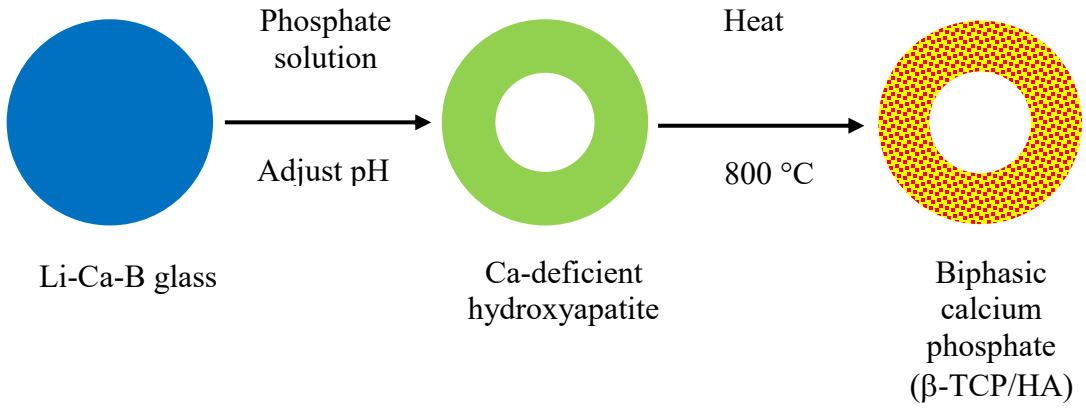

Figure 1. Schematic diagram illustrating the formation of hollow calcium deficient hydroxyapatite microspheres and hollow biphasic calcium phosphate microspheres.

Hollow CDHA microspheres were obtained by the glass conversion technique described in previous studies [17]. Briefly, a lithium-calcium- borate glass with the nominal composition $11Li_2O$, 15CaO, and $74B_2O_3$ (wt%) was prepared by melting appropriate amounts of Li_2CO_3, $CaCO_3$, and H_3BO_3 (Alfa Aesar, Haverhill, MA, USA) in a platinum crucible at 1200 °C for 45 min, then quenching the melt between stainless steel plates. Glass particles with sizes between 150 and 250 μm were obtained by grinding the glass in a shatter box and sieving through 60 and 100 mesh sieves. Glass microspheres were obtained by dropping the crushed particles through a vertical furnace

at 1200 °C. The glass microspheres were reacted in K_2HPO_4 solutions (0.1 M or 0.25M) with pH values ranging between 7 and 12 at 37°C for 2-4 days, at a ratio of 1 g glass in 200 ml phosphate solution, while stirring continuously. The initial pH of the phosphate solution was set using appropriate amounts of HCl or NaOH. The converted microspheres were washed with distilled water and anhydrous ethanol, and then dried at room temperature for at least 12 h, and then at 90 °C for at least 12 h. After conversion, some CDHA microspheres were converted to BCP microspheres by heating them in a platinum dish in air at 800°C for 5 hours.

2.2. CHARACTERIZATION OF MICROSPHERES

The microstructures of as-prepared and heat-treated microspheres were characterized by scanning electron microscopy (SEM) (S4700, Hitachi, Tokyo, Japan), at an accelerating voltage of 15 kV and working distance of 12.5 mm. Phase compositions were analyzed using X-ray diffraction (XRD) (PANalytical X'Pert Pro multi-purpose diffractometer). The XRD data were acquired in the 2θ range of 5-90° at a scanning speed of 2.8°/min using Cu K_α radiation (λ=0.15406 nm). The diffraction data were compared with JCPDS cards of HA (01-076-0694) and β-TCP (01-070-2065), respectively. The weight fractions of HA and β-TCP in the heat-treated microspheres were estimated by matching the intensities of respective peaks with the intensity of each pure phase. The Ca/P ratios of the microspheres were determined by dissolving them in 10% HNO_3 solution and then measuring the respective concentrations of calcium and phosphorus using inductively-coupled optical emission spectroscopy (ICP-OES) (Avio 200; Perkin Elmer, Waltham, MA).

Nitrogen absorption techniques (Surface Area & Pore Size Analyzer; NOVA 2000e; Quantachrome, Boyton Beach, FL) were used to determine specific surface areas (SSA) of the microspheres (Brunauer-Emmett-Teller (BET) analyses) and the pore size distributions in their respective shell walls (Barrett-Joiner-Halenda (BJH) method). Three replicates for each group were measured and average values are reported.

2.3. *IN VITRO* DEGRADATION BEHAVIOR OF CDHA AND BCP MICROSPHERES

The aqueous degradation rates of microspheres were determined using two methods. For the accelerated degradation tests, 15 mg of the microspheres were immersed in 50 ml of a potassium acetate acidic buffer (0.1M, pH=5.0) at 37 °C. Calcium and phosphorus concentrations in the solution were determined as a function of immersion time (0-3 days) using ICP-OES. In the second test, microspheres were immersed in SBF [22] with starting pH of 7.4 at 37 °C. Changes in microsphere mass and solution pH values were measured at various times. Both tests were run in triplicate, and averages and standard deviations are reported.

After 14-days of immersion in SBF solution, the microspheres were removed, washed gently using deionized water, dried, and analyzed using SEM, as described above. The Raman spectra of the microspheres before and after SBF immersion were analyzed by μ-Raman spectrometer (ARAMIS; Horiba-Jobin Yvon, Inc.; Edison, NJ) using a He-Ne laser (632.8 nm). Finally, these microspheres were analyzed by Fourier transform infrared (FTIR) spectroscopy (Nicolet iS50; Thermo Scientific; Madison, WI) using the single-bounce attenuated total reflectance accessory.

3. RESULTS

3.1. MICROSTRUCTURES OF AS-PREPARED AND HEAT-TREATED MICROSPHRES

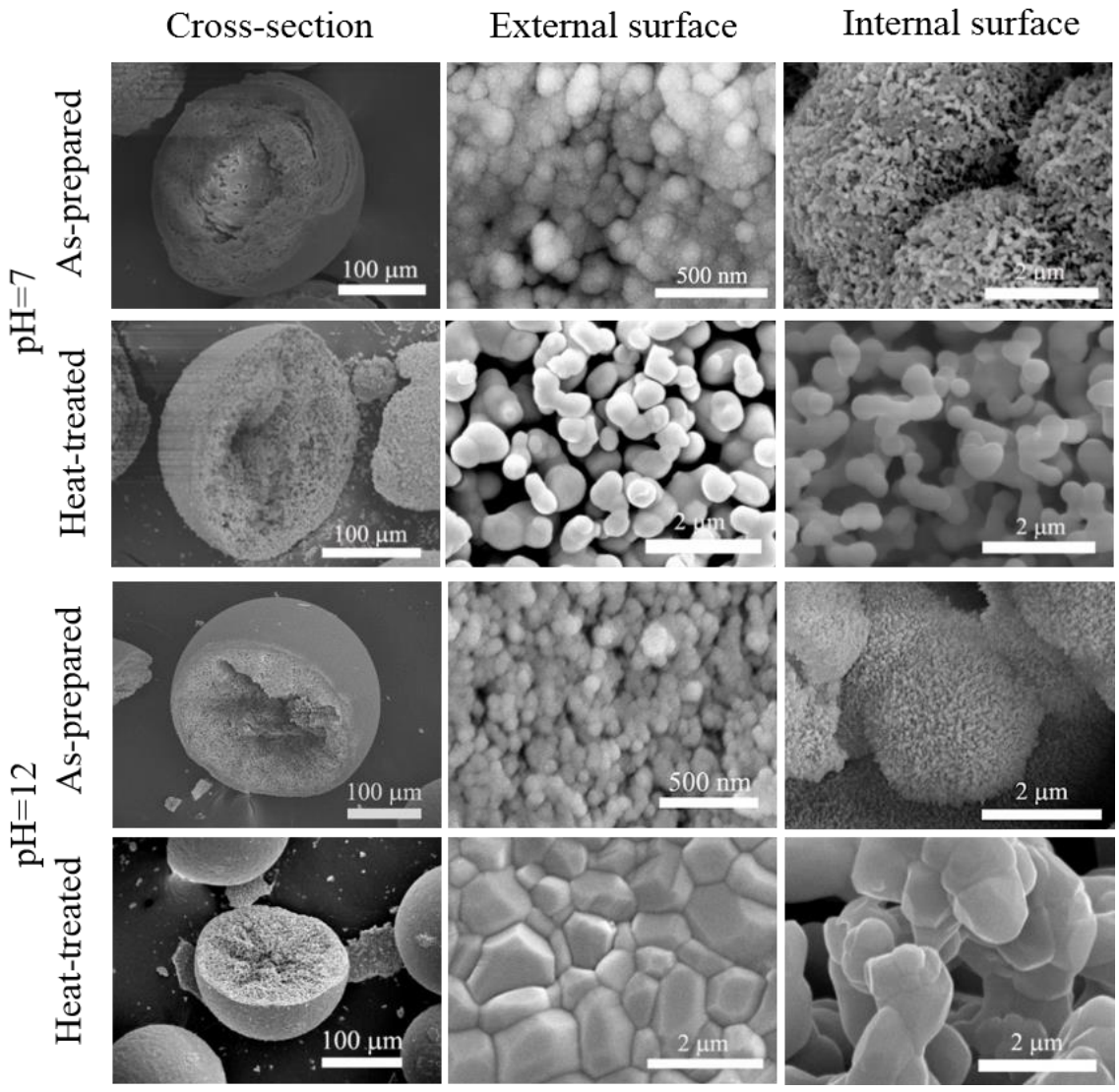

Figure 2. SEM images of hollow microspheres produced in 0.25M K_2HPO_4 solution at pH=7 and 12, showing representative cross-sections (left), external surfaces (middle), and internal surfaces (right).

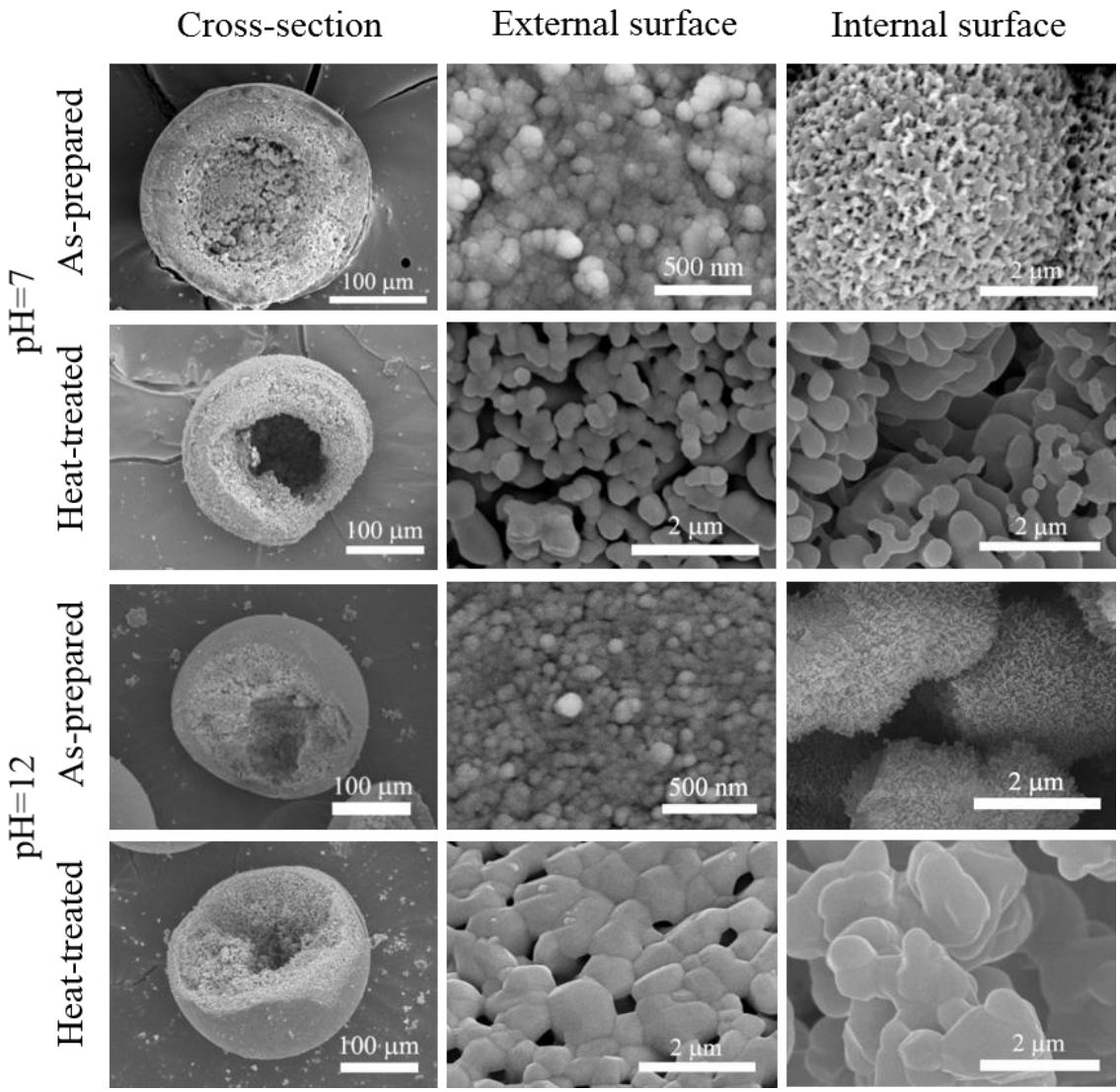

Figure 3. SEM images of hollow microspheres produced in 0.1M K_2HPO_4 solution at pH=7 and 12, showing representative cross-sections (left), external surfaces (middle), and internal surfaces (right).

Micrographs of representative as-prepared and heat-treated microspheres, produced by conversion in 0.25 M and 0.1 M K_2HPO_4 solutions, are shown in Figures 2 and 3, respectively. SEM images of the cross-sections indicate that the microspheres have porous shells and a hollow core. In general, the diameters of the hollow cores in

microspheres produced in 0.1 M K_2HPO_4 solution were larger than those of the microspheres produced in 0.25 M K_2HPO_4 solution. The diameter ratio of the hollow core (d) to the microspheres size (D) for microspheres produced in 0.1 M K_2HPO_4 solution was in the range 0.52-0.54, whereas the d/D ratio was in the range 0.35-0.37 for the microspheres produced in 0.25 M K_2HPO_4 solution (Table 1).

Table 1. The diameter ratio of the hollow core (d) to the outer surface (D) of the microspheres prepared under the conditions indicated, along with their average particle sizes, surface areas, and pore sizes.

Microspheres			d/D	Particle size (nm)	Surface area (m^2/g)	Average pore size (nm)
pH	K_2HPO_4 solution (M)	Heat-treatment				
7	0.25	-	0.374 ± 0.011	133 ± 13	152.0 ± 2.0	13.1 ± 0.2
7	0.25	800°C/5h	0.353 ± 0.013	530 ± 90	1.5 ± 0.2	7.7 ± 0.2
12	0.25	-	0.371 ± 0.006	90 ± 13	137.2 ± 5	9.1 ± 0.1
12	0.25	800°C/5h	0.363 ± 0.011	770 ± 294	0.6 ± 0.1	6.9 ± 0.2
7	0.1	-	0.543 ± 0.007	113 ± 16	147.4 ± 1.4	14 ± 0.1
7	0.1	800°C/5h	0.536 ± 0.011	365 ±130	3.6 ± 0.1	6.8 ± 0.6
12	0.1	-	0.534 ± 0.013	84 ± 22	148.2 ± 2.3	13.3 ± 0.5
12	0.1	800°C/5h	0.518 ± 0.016	748 ± 253	6.6 ± 0.2	6.2 ± 0.3

The as-prepared microspheres appear to be composed of nanoparticles with nearly spherical morphologies, and the particle sizes of the heat-treated samples are greater than those of the “as-prepared” samples. Image J [23] was used to characterize the average

sizes of the particles that form the shell walls of the microspheres shown in Figures 2 and 3, and those values are given in Table 1. In general, the particle sizes of the as-prepared microspheres were similar, ranging from about 80 to about 130 nm, whereas the particle sizes of the heat-treated microspheres were significantly larger, ranging from 365 to 770 nm.

The surface areas and average pore sizes of the microspheres decreased significantly after the heat treatments, as shown in Table 1. After heat-treatment, the surface areas of the microspheres produced in 0.25 M K_2HPO_4 solution were lower (0.6 and 1.5 m^2/g) than those produced in 0.1 M K_2HPO_4 solution (3.6 and 6.6 m^2/g).

3.2. PHASE DISTRIBUTIONS AND COMPOSITIONS OF THE AS-PREPARED AND HEAT-TREATED MICROSPHERES

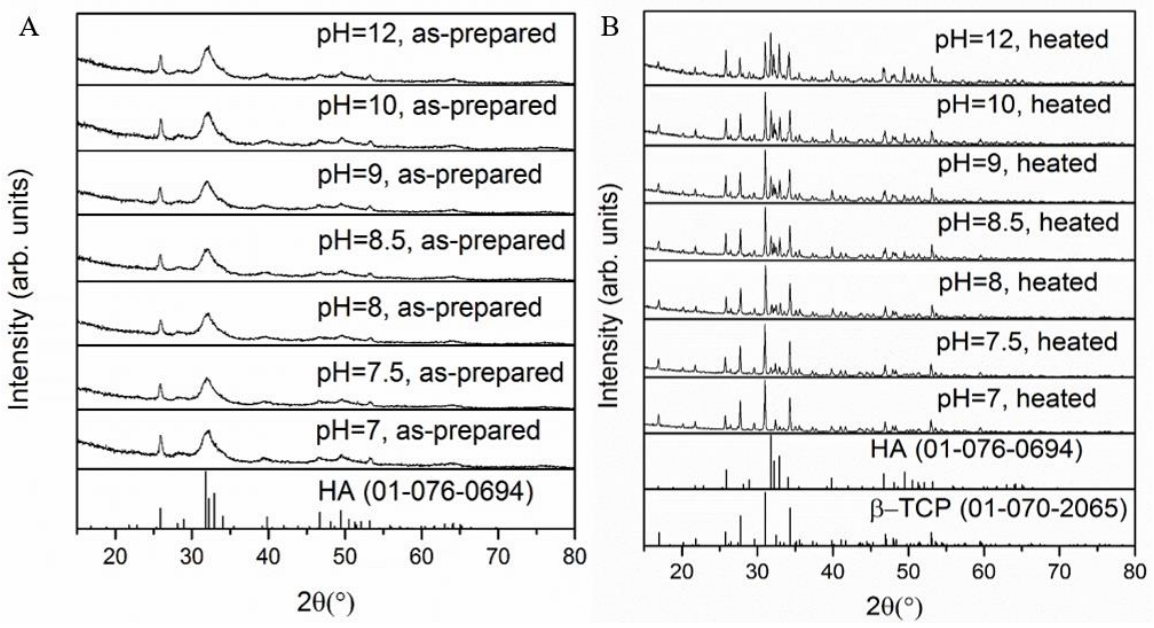

Figure 4. XRD patterns from the (A) as-prepared and (B) heat-treated microspheres produced in 0.25M K_2HPO_4 solution at various pH values.

Figure 4 shows the XRD patterns of the as-prepared and heat-treated microspheres produced in 0.25 M KH_2PO_4 solutions. Similar patterns were collected from the particles prepared in 0.1 M KH_2PO_4 solutions. The broad peaks in the XRD patterns of the as-prepared microspheres may indicate that the material was poorly crystallized, or consisted of nanometer-sized crystals, or a combination of both. These patterns are typical for Ca-deficient hydroxyapatite (CDHA) [24, 25].The intensity of the peaks increased markedly for the heat-treated microspheres, presumably as the result of increased crystal fraction or crystal size. The XRD patterns of heat-treated microspheres indicated the presence of various weight ratios of hydroxyapatite (HA) and tricalcium phosphate (β-TCP). The weight fractions of the two phases (β-TCP and HA) in the heat-treated microspheres produced in 0.25 M and 0.1 M K_2HPO_4 solutions are summarized in Table 2. For the heat-treated microspheres produced in 0.25 M K_2HPO_4 solution, the β-TCP/HA weight ratios varied from >99/1 at pH=7 to 49/51 at pH=12. For the heat-treated microspheres produced in 0.1 M K_2HPO_4 solution, the β-TCP/HA ratios varied from 70/30 at pH=7 to 44/56 at pH=12.

The quantitative XRD data was used to estimate the Ca/P atomic ratios of heat-treated microspheres from the relative fractions of β-TCP (Ca/P=1.50) and HA (Ca/P=1.67), and is compared with the Ca/P ratios determined by ICP-OES on microspheres dissolved in nitric acid (Table 2). There is a good agreement between the two sets of measurements.

Figure 5 shows the Ca/P values determined for as-prepared microspheres (ICP only) and heat-treated microspheres (ICP and XRD), prepared in 0.25M and 0.1 M KH_2PO_4 solutions at different values of pH. There are no significant differences in the

compositions of the respective as-prepared and heat-treated particles, and the Ca/P ratios for both sets of particles increases with increasing solution pH.

Table 2. Fractions of HA and β-TCP (wt%) and the Ca/P atomic ratios, from XRD and ICP, for heat-treated microspheres produced in 0.25 M and 0.1 M K_2HPO_4 solutions at various pH values.

	0.25 M			0.1 M		
	XRD		ICP	XRD		ICP
	β-TCP/HA (wt%)	Ca/P	Ca/P	β-TCP/HA (wt%)	Ca/P	Ca/P
pH=7	>99/1	1.50	1.51 ± 0.02	70/30	1.55	1.55 ± 0.01
pH=7.5	86/14	1.52	1.51 ± 0.02	-	-	-
pH=8	82/18	1.53	1.53 ± 0.01	56/44	1.57	1.57 ± 0.01
pH=8.5	73/27	1.54	1.55 ± 0.02	-	-	-
pH=9	70/30	1.55	1.56 ± 0.01	51/47	1.58	1.58 ± 0.01
pH=10	65/35	1.56	1.57 ± 0.02	-	-	
pH=11	-	-	-	46/54	1.59	1.58 ± 0.01
pH=12	49/51	1.58	1.59 ± 0.01	44/56	1.59	1.58 ± 0.03

Therefore, based on XRD and ICP-OES analysis, we can confirm that the as-prepared microspheres produced by glass conversion technique are CDHA microspheres, and the heat-treated microspheres were BCP microspheres.

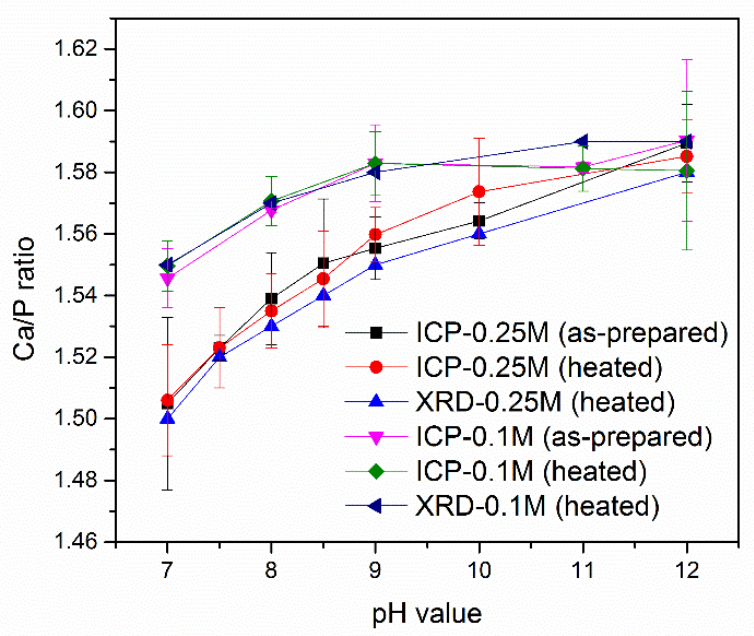

Figure 5. Ca/P ratios of as-prepared and heat-treated microspheres produced in 0.25 M and 0.1 M K_2HPO_4 solutions measured by ICP-OES and estimated by XRD.

3.3. *IN VITRO* DEGRADATION

3.3.1. Ion Release Kinetics in Potassium Acetate Solutions. KAc solution was chosen to evaluate the relative reactivities of the CDHA and BCP microspheres, following procedures similar to those reported elsewhere [18, 26]. The calcium and phosphate ions released to the KAc solution are shown in Figure 6 A and B, respectively. Similar release kinetics were observed for each of the four sets of microspheres evaluated, with faster ion release rates over the first ten hours of reaction, and slower release rates thereafter. In general, the CDHA microspheres released phosphate anions at faster rates than their respective BCP microspheres, (Figure 6B), but the fastest Ca-release occurred from the BCP/pH=7 microspheres (Figure 6A). The Ca/P ion ratios, released to the KAc solutions, normalized to the initial Ca/P ratios in the respective

particles, are shown as a function of immersion time in Figure 6 C. If this ratio equals 1, then the particles dissolve congruently. If the ratio is less than 1, then phosphate is preferentially released to the solution. This analysis indicates that the CDHA microspheres (pH=7 and pH=12) dissolve congruently, at least for the first 24 hours. The BCP (pH=7) particles, have Ca/P release ratios lower than what would be expected from congruent dissolution. As discussed below, this can be explained by a faster dissolution of the β-TCP phase (Ca/P=1.5) in these BCP particles than the HA phase (Ca/P=1.67).

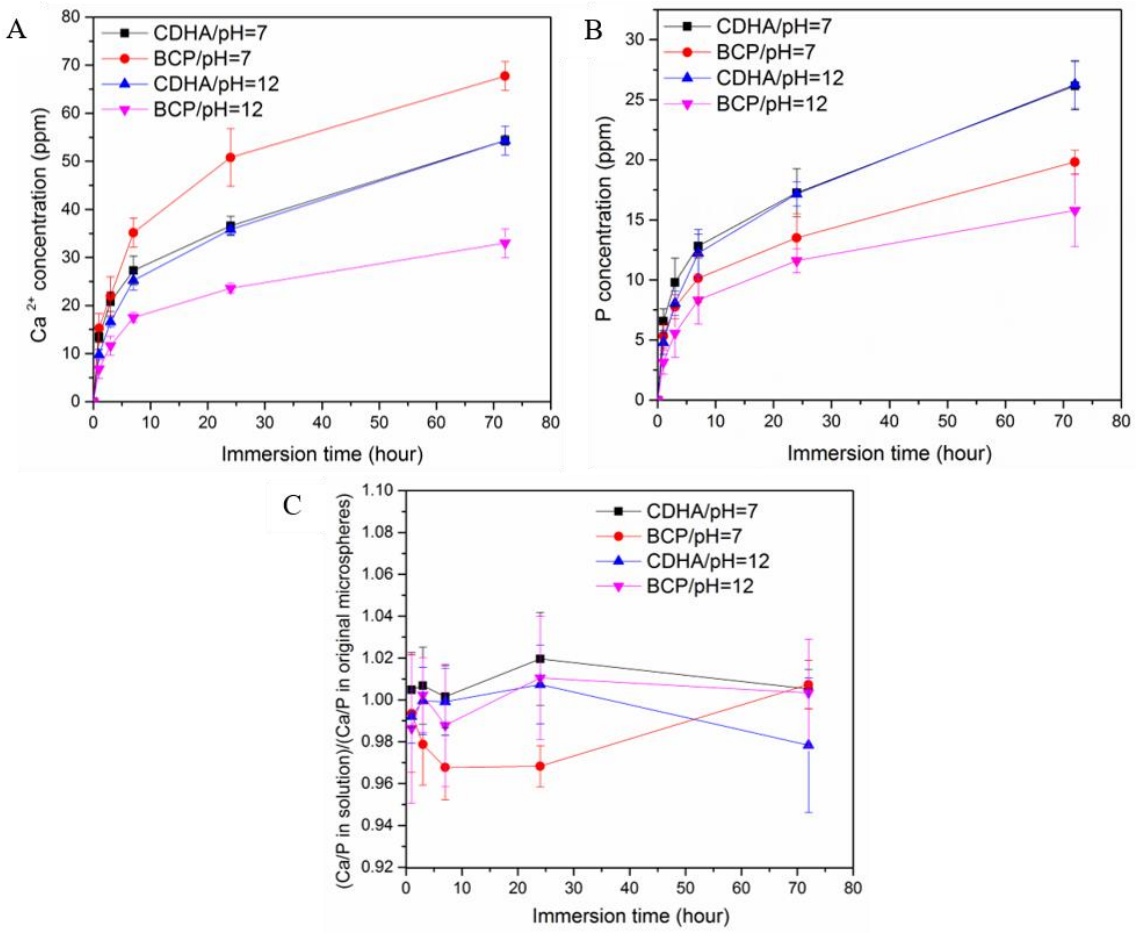

Figure 6. Time dependences of the release of (A) Ca and (B) P from different microspheres to the KAc solution. (C) The Ca/P ion ratios released from different microspheres to the KAc solutions.

3.3.2. Apatite Formation in Simulated Body Fluid. The microspheres were immersed in SBF solution at 37°C for two weeks. The mass of each set of microspheres initially decreased, then increased over the course of the experiment (Figure 7), an indication of occurrence of some initial dissolution and subsequent precipitation processes. The pH of the SBF increased slightly, from 7.4 to ~7.6, over the two-week experiment (Figure B.3).

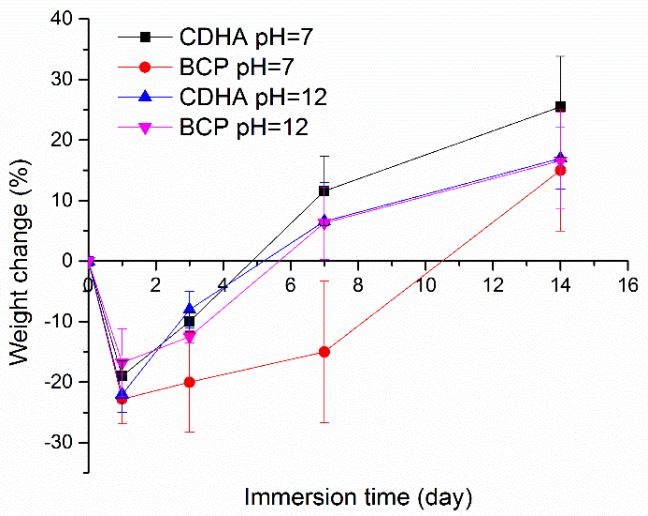

Figure 7. Weight changes in SBF solution at 37°C of the microspheres produced in 0.1 M K_2HPO_4 solution.

Scanning electron micrographs of the surfaces of microspheres before and after immersion in SBF solution are shown in Figure 8. After immersion, the surfaces of the grains that constitute the structures of BCP/pH=7 and BCP/pH=12 microspheres are covered by smaller (<100 nm) crystals and some of these smaller crystals have formed clusters. Smaller crystals appear to have also formed on the surfaces of the CDHA

microspheres immersed in SBF, although these changes in surface topologies are less obvious than they are for the BCP microspheres with their larger initial grain sizes.

Figure 9A and B shows the FTIR spectra collected from the different sets of microspheres, before and after immersion in SBF. The absorption bands corresponding to PO_4^{3-} groups were observed in all spectra at approximately 1000-1120 cm^{-1} (v_3), 945-970 cm^{-1} (v_1), 550-600 cm^{-1} (v_4), and these are consistent with the presence of apatitic phases [27]. A peak ~875 cm^{-1} in the spectra from the CDHA samples is assigned to HPO_4^{2-} groups in these materials. The spectra of the CDHA samples also revealed the presence of water (or -OH) species, including the sharp peak ~3570 cm^{-1} due to isolated OH groups [27, 28], and the board peaks in the ranges 1600-1700 cm^{-1} and 3200-3600 cm^{-1}, assigned to various water vibrations [27]. The spectra from the CDHA particles also have peaks in the range 1420-1460 cm^{-1} that can be assigned to the v_2 modes of CO_3^{2-} [27], characteristic of the B type substitution of phosphate anions by carbonate anions in carbonated hydroxyapatites. This carbonate component may have formed from atmospheric CO_2 dissolved in phosphate solution during the glass conversion process. Heat treating the CDHA microspheres to create the BCP microspheres eliminates the carbonate from the β-TCP/HA structures, along with the water and the HPO_4^{2-} anions. The peaks at 974 cm^{-1} and 947 cm^{-1} assign to the phosphate mode transformed from the peak at 962 cm^{-1}, which indicate the presence of β-TCP [27]. After immersion in SBF solution, there is clear evidence for CO_3^{2-} incorporation into the structures of all four sets of microspheres, CDHA and BCP, indicating the formation of possible B-site carbonate-substituted apatite.

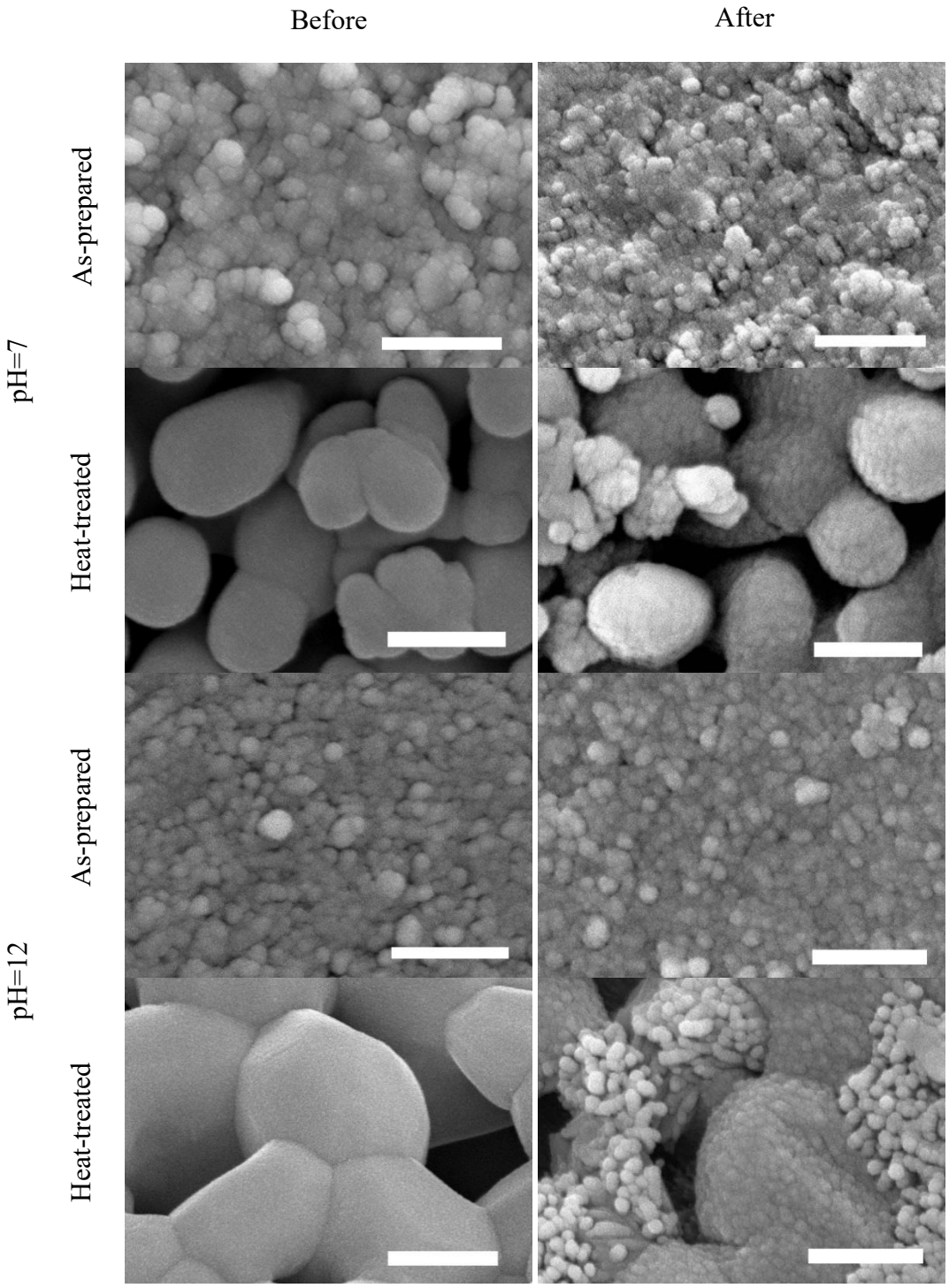

Figure 8. SEM images of the external surfaces of the microspheres produced in 0.1 M K_2HPO_4 solutions before (left) and after (right) two-weeks of immersion in SBF solution at 37°C. (scale bar=500 nm)

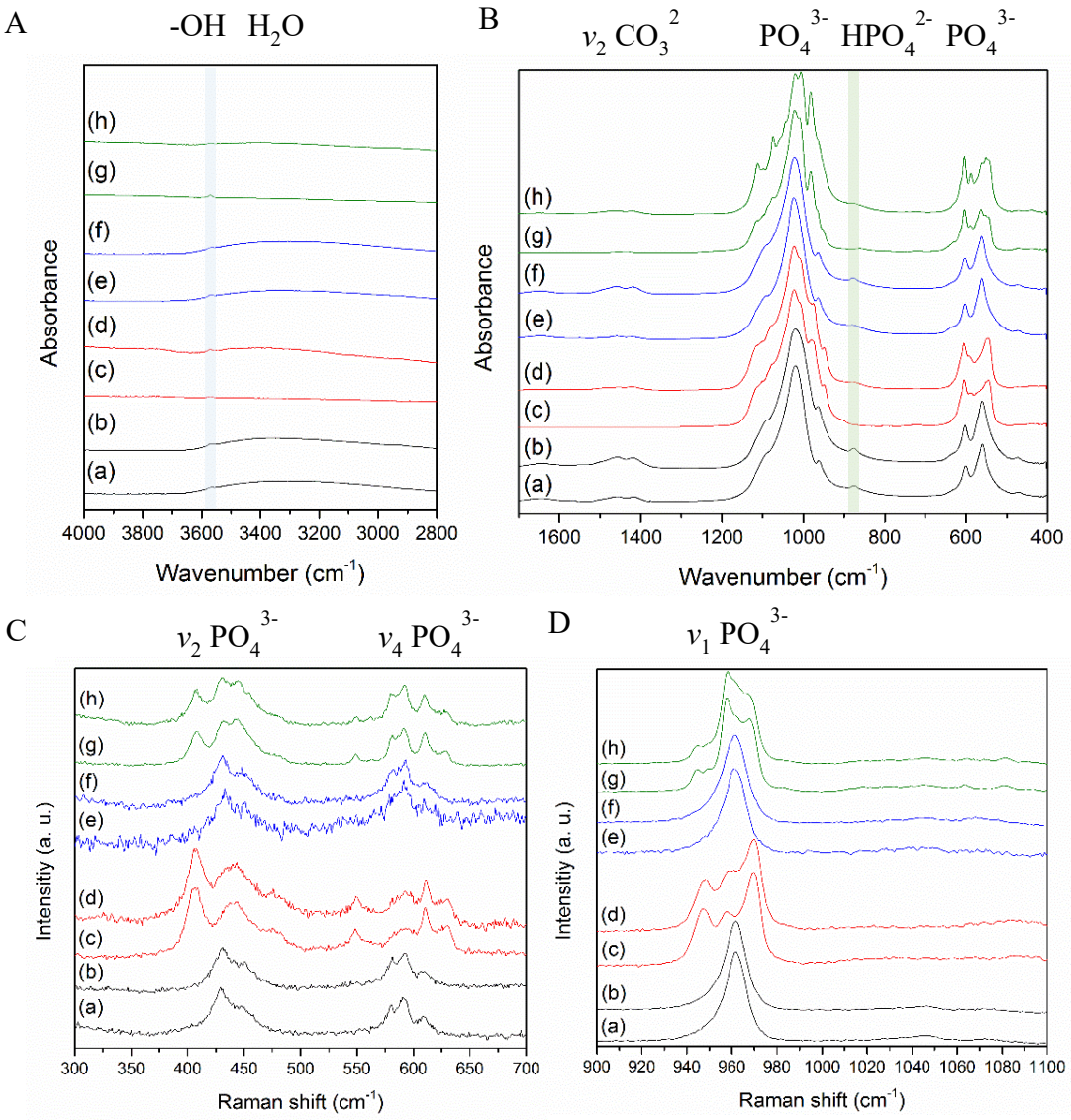

Figure 9. FTIR (A, B) and Raman (C, D) spectra of the microspheres before and after immersion in SBF solution for 14 days. CDHA/pH=7: (a) before and (b) after; BCP/pH=7: (c) before and (d) after; CDHA/pH=12: (e) before and (f) after; BCP/pH=12: (g) before and (h) after.

Figure 9C and B shows the Raman spectra collected from CDHA spheres prepared at pH=7 and pH=12, before and after two weeks of immersion in SBF, and the related BCP microspheres, also before and after SBF immersion. The spectra from the CDHA microspheres are dominated by a peak at ~960 cm^{-1}, assigned to the symmetric P-

O stretching mode (v_1) of PO_4^{3-} species, whereas two peaks evident in the spectra from the BCP microspheres, at 948 cm^{-1} and 970 cm^{-1}, are assigned to v_1 stretching modes of the PO_4^{3-} anions in β-TCP [29-31]. Peaks in the ranges 570-625 cm^{-1} and 400-490 cm^{-1} are attributed to the v_4 and v_2 modes of PO_4^{3-}, respectively. The v_4 and v_2 vibrational modes of PO_4^{3-} are well-separated in the spectrum for HA, whereas these two modes are less separated in the spectrum for β-TCP [30]. The low intensity, asymmetric v_3 stretching mode is located in the 1000-1100 cm^{-1} range [32, 33].

The Raman spectra collected from the CDHA microspheres are similar to those collected from HA, whereas the Raman spectra from the BCP microspheres are a mixture of the characteristic spectra of HA and β-TCP [30]. Moreover, the intensity of the characteristic peak of HA at 960-962 cm^{-1} is relatively lower than the characteristic peaks of β-TCP at 948 cm^{-1} and 970 cm^{-1} for BCP microspheres with greater β-TCP contents, (e.g., see the XRD data in Table 2), whereas the relative intensity of the characteristic peak of HA is greater than those for β-TCP from BCP microspheres with lower contents of β-TCP.

After immersion of the BCP microspheres in SBF solution, there is an increase in the relative intensity of the characteristic Raman peak of HA at 960-962 cm^{-1}, compared to the β-TCP peak intensities at 948 cm^{-1} and 970 cm^{-1}. This might indicate that the β-TCP phase dissolved from the BCP microspheres, to reprecipitate as nanocrystalline HA.

Finally, the low intensity peak at ~1070 $cm^{-1,}$ assigned to the v_1 CO_3^{2-} symmetric vibrational mode, provides some additional evidence for the presence of carbonate species in the CDHA microspheres [34, 35].

4. DISCUSSION

4.1. SYNTHESIS OF CDHA AND BCP MICROSPHERES

The hollow calcium phosphate microspheres formed using the borate glass conversion technique are similar to those described in previous studies [17, 36, 37]. When the calcium ions released from the dissolving Li-Ca-borate glass exceed the local solubility limit, they react with phosphate anions in solution to form an insoluble CDHA phase that precipitates on the glass surface. As the glass further dissolves, the calcium ions react with phosphate anions that diffuse through the CDHA surface layer, causing that layer to thicken by growing inward towards the center of the microsphere. When the glass is completely dissolved, a hollow CDHA microsphere will have formed if the initial CaO-content of the glass is low, as it was in the present study (20 mole%). Filled CDHA microspheres form when the initial CaO-contents are greater; e.g., 40 wt% [37].

The compositions and morphologies of the CDHA microspheres in the present study depend on the pH and phosphate concentration of the conversion solution. For example, the Ca/P ratio of the microspheres increases with increasing solution pH and with lower solution phosphate concentration (Figure 5). The relative diameter of the hollow core is greater for microspheres produced in solutions with lower phosphate concentrations (Table 1).

Variations in CDHA composition can be understood by considering the effects of pH on phosphate speciation in solution. For example, the phosphate anion speciation equilibria at 25°C are given by

$$H_3PO_4 + H_2O \overset{pKa=2.21}{\longleftrightarrow} H_2PO_4^- + H_3O^+ \quad (1)$$

$$H_2PO_4^- + H_2O \overset{pKa=7.21}{\longleftrightarrow} HPO_4^{2-} + H_3O^+ \quad (2)$$

$$HPO_4^{2-} + H_2O \overset{pKa=12.67}{\longleftrightarrow} PO_4^{3-} + H_3O^+ \quad (3)$$

These are the phosphate species that react with the Ca-ions released from the dissolving Li-Ca-borate glass to precipitate CDHA. Speciation of phosphate anions in aqueous solutions depends on pH; $H_2PO_4^-$ and HPO_4^{2-} are the dominant anions in solutions with pH<10, and PO_4^{3-} anions become increasingly significant in more alkaline solutions. Ignoring the incorporation of carbonate anions, CDHA has the general chemical formula $Ca_{10-x}(HPO_4)_x(PO_4)_{6-x}(OH)_{2-x}$. The fraction of HPO_4^{2-} anions incorporated in the CDHA structure is thus related to the Ca/P according to

$$\frac{\text{Ca}}{\text{P}} = \frac{10-x}{x+(6-x)} = \frac{10-x}{6} \quad (4)$$

From equation (3), for the pH range used in this study to prepare the CDHA microspheres, the fraction of HPO_4^{2-} anions in solution decrease with increasing pH. If the fraction of HPO_4^{2-} incorporated into the CDHA ('x') depends on the concentration of HPO_4^{2-} in the conversion solution, then from equation (4), the Ca/P ratio in the resulting CDHA should increase with increasing solution pH, as shown in Figure 5. Similar effects of solution pH on the precipitation of Ca-phosphate phases have been reported in the literature [30, 38], where pure β-TCP (Ca/P=1.5) could be obtained by precipitation reactions from solutions with pH ~7 and subsequent heat treatments, whereas BCP particles with increasing fractions of HA (Ca/P=1.67) were produced from particles precipitated under more basic conditions (pH ≥ 8), followed by heat treatments.

The CDHA particles produced from the 0.25M KH_2PO_4 solutions generally had lower Ca/P ratios than those produced from the 0.1M KH_2PO_4 solutions, particularly at

the lower pH values (Figure 5). That might be due to the pH changes in the 0.25M KH_2PO_4 solutions caused by glass conversion were less than those in 0.1M KH_2PO_4 solutions. Moreover, the saturation index (SI) of precipitated hydroxyapatite is affected by the phosphate concentration [39]. When SI>0, the precipitation occurs spontaneously. It is reported that SI increase as phosphate concentration and pH of the solution increase[39]. Therefore, at a certain pH of the solution, precipitation of CDHA is easier in higher concentrated phosphate solution than in lower concentrated phosphate solution.

The relative diameters of the hollow cores in the microspheres produced in the 0.25M KH_2PO_4 solutions are smaller than those in the microspheres produced in the 0.1M KH_2PO_4 solutions (Table 1), consistent with a previous study [17]. The average size of the individual grains on the surfaces of the CDHA microspheres and the microsphere surface areas and nanopore sizes are similar. The lower phosphate concentration likely leads to slower growth of calcium phosphate nuclei which may result in more efficient packing of the calcium phosphate crystals. In addition, the nanoparticle size observed on the external surface of the microspheres decreased from pH=7 to pH=12 for both concentrations of phosphate solutions (Table A.1). Based on some dissolution behavior studies of borate glass [40, 41], the dissolution rate of the glass was found to be pH-dependent. For binary Li-B glass, the glass dissolution rate decreased as the pH value of buffer solution increased from 4 to 10 [40]. For Na-Ca-B glass in pH=4, 7 and 10 buffer solutions, the glass was found to dissolve faster in lower pH solutions [41]. We conjectured that the dissolution rate of our Li-Ca-B glass increased as the pH value decreased, which may lead to faster formation of calcium phosphate nuclei. In addition, the faster dissolution of the glass may provide a higher concentration of Ca^{2+}. The higher

concentration of calcium and phosphate ions may accelerate the aggregation of initial amorphous calcium phosphate [11, 42], which may lead to a larger particle size of calcium phosphate.

Heat-treatments have been used in previous studies of Ca-phosphate microspheres to increase their mechanical strength [36, 43], although the development of biphasic ceramic microspheres with different concentrations of β-TCP and HA has not been previously described. In the present study, heating the microspheres at 800 °C for 5 hours clearly transformed the CDHA to β-TCP and HA. FTIR spectra (Figure 10A and B) show the disappearance of HPO_4^{2-} and CO_3^{2-} species from the CDHA, and the appearance of characteristic peaks of β-TCP after the heat treatment. XRD (Figures 4 and 5) confirmed the formation of crystalline HA and β-TCP, with fractions that depended on the initial composition of the CDHA materials (Figure 5).

When heated above about 700°C, CDHA decomposes to stoichiometric compounds, the relative fractions of which depend on the starting Ca/P ratio [26, 44]:

$$Ca_{10-x}(HPO_4)_x(PO_4)_{6-x}(OH)_{2-x} \rightarrow$$

$$3x\beta - Ca_3(PO_4)_2 + (1-x)Ca_{10}(PO_4)_6(OH)_2 + xH_2O \quad (6)$$

When x=1 (Ca/P=1.5), the decomposition of CDHA produces β-TCP, when x=0, hydroxyapatite is produced, and when 0 < x <1 (1.5<[Ca/P]<1.67), BCP particles with mixtures of β-TCP and HA are produced. For example, CDHA particles with x=0.50, ($Ca_{9.5}(HPO_4)_{0.5}(PO_4)_{5.5}(OH)_{1.5}$), where Ca/P=1.58, will decompose to BCP particles with 48 wt% TCP: 52 wt% HA. Therefore, the ultimate composition of the BCP particles is tailored by controlling the pH of the phosphate solution used in the conversion process,

which controls the speciation of phosphate anions that react with the Ca-ions released from the glass, and so control the Ca/P ratio of the precipitated particles.

The heat treatment not only leads to the development of the distribution of phases that constitute the microspheres, but also affects their microstructure. The surface areas of the microspheres decreased dramatically after the heat-treatment and the particle size in the external surface increased after heat treatment (Table 1). In addition, the average size of the particles that constitute the microstructures of the BCP microspheres increased with increasing HA content.

4.2. *IN VITRO* DEGRADATION OF CDHA AND BCP MICROSPHERES

The *in vitro* degradation of calcium phosphate is affected by the composition and microstructure (i.e. surface area, porosity, pore size) of the microspheres, and the composition and pH of the solution. In general, the solubility of calcium phosphates in aqueous solutions decreases in order β-TCP (Ca/P=1.5, solubility at 37 °C, $-\log(K_{sp})=29.5$) > CDHA (Ca/P=1.5~1.67, solubility at 37 °C, $-\log(K_{sp})$ =~85.1)>HA (Ca/P=1.67, solubility at 37 °C, $-\log(K_{sp})=116.8$) [5]. The comparative solubility in acidic buffer increases in order: β-TCP>CDHA>>HA [5]. A greater specific surface area (SSA) for a particle could lead to a greater dissolution rate. In this study, the SSA of the CDHA microspheres are significantly greater than those of the BCP microspheres (Table 1).

In the accelerated degradation test, the release profiles of the calcium and phosphate ions from the microspheres were determined (Figure 6). The differences between the respective release rates of calcium and phosphate ions can be related to the

different Ca/P ratios of the microspheres and their microstructures. Although the P-release rates from the CDHA microspheres were generally greater than from the BCP microspheres, this might be understood from the much greater surface areas of the former particles (Table 1); normalized to surface area, the BCP particles are more reactive than the CDHA particles. For the two different BCP particles tested in Figure 6, the ones with the greater β-TCP/HA ratio (pH=7, 70/30) released Ca and phosphate species at a greater rate than the particles with the lower β-TCP/HA ratio (pH=12, 44/56), consistent with what is reported about the relative solubility of β-TCP and HA ratio [26, 45]. The initial normalized Ca/P ratio of ions released from the β-TCP/HA=70/30 particles was lower than the normalized Ca/P ratios from the other particles, indicating that the β-TCP phase was dissolving preferentially (Figure 6C).

Apatite-formation is a criterion used to evaluate the *in vitro* bioactivity of implant materials [46]. When the microspheres were immersed in SBF solution, their masses at first decreased and then increased with immersion time (Figure 7). Calcium and phosphate ions released from the microspheres re-precipitated as nanocrystalline hydroxyapatite particles on the surfaces of the microspheres, as indicated in the SEM images in Figure 8. The FTIR spectra in Figure 9B are consistent with the formation of carbonate-substituted hydroxyapatite. For BCP microspheres, the changes in the relative intensities of characteristic Raman peak of HA at 960-962 cm^{-1} to the β-TCP peak intensities at 948 cm^{-1} and 970 cm^{-1} after SBF immersion indicates the dissolution of β-TCP phase from the BCP microspheres and the reprecipitation of HA (Figure 9D). More apatite formation was observed on the surfaces of BCP microspheres with 70wt% β-TCP content than the BCP microspheres with 44wt% β-TCP (Figure B.5).

5. CONCLUSIONS

This study demonstrated that hollow BCP microspheres could be produced by the heat-treatment of CDHA microspheres obtained by the glass conversion technique. The composition and microstructure of the microspheres was affected by the concentration and pH value of the phosphate solution in glass conversion process. Two sets of CDHA microspheres (Ca/P ≈ 1.55 and 1.59) and the corresponding BCP microspheres (β-TCP/HA=70/30 and 44/56were selected for further *in vitro* tests. The BCP microspheres with 70wt% β-TCP showed faster degradation rates in acetic acid and converted more quickly to HA in simulated body fluids. The ability to tailor the composition, nano-structure, and meso-structure of these microspheres by controlling the processing conditions to convert the Li-Ca-B glasses in phosphate solutions means that materials can be designed for specific biomedical applications that utilize the macro-porosity of the hollow microspheres, the nano-porosity of the shell walls, and the enhanced bio-activity of the BCP phases.

ACKNOWLEDGEMENT

We are grateful for the technical support of colleagues in the Missouri S&T Materials Research Center and for the financial support of the Lasko Endowment in the Department of Materials Science and Engineering.

REFERENCES

[1] J.C. Elliott, *Structure and chemistry of the apatites and other calcium orthophosphates*. Vol. 18. 2013: Elsevier.

[2] R.Z. Legeros, *Apatites in biological systems.* Progress in crystal growth and characterization, 1981. **4**(1-2): p. 1-45.

[3] C. Rey, V. Renugopalakrishman, B. Collins, and M.J. Glimcher, *Fourier transform infrared spectroscopic study of the carbonate ions in bone mineral during aging.* Calcified tissue international, 1991. **49**(4): p. 251-258.

[4] R.Z. LeGeros, *Calcium phosphate-based osteoinductive materials.* Chemical Reviews, 2008. **108**(11): p. 4742-4753.

[5] N. Eliaz and N. Metoki, *Calcium phosphate bioceramics: A review of their history, structure, properties, coating technologies and biomedical applications.* Materials, 2017. **10**(4): p. 334.

[6] W. Wang and K.W.K. Yeung, *Bone grafts and biomaterials substitutes for bone defect repair: A review.* Bioactive Materials, 2017. **2**(4): p. 224-247.

[7] E. García-Gareta, M.J. Coathup, and G.W. Blunn, *Osteoinduction of bone grafting materials for bone repair and regeneration.* Bone, 2015. **81**: p. 112-121.

[8] V. Campana, G. Milano, E. Pagano, M. Barba, C. Cicione, G. Salonna, W. Lattanzi, and G. Logroscino, *Bone substitutes in orthopaedic surgery: from basic science to clinical practice.* Journal of Materials Science: Materials in Medicine, 2014. **25**(10): p. 2445-2461.

[9] C. Laurencin, Y. Khan, and S.F. El-Amin, *Bone graft substitutes.* Expert review of medical devices, 2006. **3**(1): p. 49-57.

[10] M. Bohner and J. Lemaitre, *Can bioactivity be tested in vitro with SBF solution?* Biomaterials, 2009. **30**(12): p. 2175-2179.

[11] S.V. Dorozhkin, *Calcium orthophosphates (CaPO4): occurrence and properties.* Progress in Biomaterials, 2016. **5**(1): p. 9-70.

[12] I.R. Gibson, I. Rehman, S.M. Best, and W. Bonfield, *Characterization of the transformation from calcium-deficient apatite to β-tricalcium phosphate.* Journal of Materials Science: Materials in Medicine, 2000. **11**(12): p. 799-804.

[13] K.-R. Kang, Z.-G. Piao, J.-S. Kim, I.-A. Cho, M.-J. Yim, B.-H. Kim, J.-S. Oh, J.S. Son, C.S. Kim, and D.K. Kim, *Synthesis and Characterization of β-Tricalcium Phosphate Derived From Haliotis sp. Shells.* Implant dentistry, 2017. **26**(3): p. 378-387.

[14] J. Tao, H. Pan, H. Zhai, J. Wang, L. Li, J. Wu, W. Jiang, X. Xu, and R. Tang, *Controls of tricalcium phosphate single-crystal formation from its amorphous precursor by interfacial energy.* Crystal Growth and Design, 2009. **9**(7): p. 3154-3160.

[15] W. Huang, D.E. Day, and M.N. Rahaman, *Conversion of tetranary borate glasses to phosphate compounds in aqueous phosphate solution.* Journal of the American Ceramic Society, 2008. **91**(6): p. 1898-1904.

[16] N.N. Vanderspiegel, *Reaction of potassium calcium borate glasses to form apatite and dicalcium phosphate dihydrate*. Masters Theses, Missouri University of Science and Technology, 2004.

[17] H. Fu, M.N. Rahaman, and D.E. Day, *Effect of process variables on the microstructure of hollow hydroxyapatite microspheres prepared by a glass conversion method.* Journal of the American Ceramic Society, 2010. **93**(10): p. 3116-3123.

[18] W. Xiao, B. Sonny Bal, and M.N. Rahaman, *Preparation of resorbable carbonate-substituted hollow hydroxyapatite microspheres and their evaluation in osseous defects in vivo.* Materials Science & Engineering C, 2016. **60**: p. 324-332.

[19] H. Fu, M.N. Rahaman, D.E. Day, and W. Huang, *Effect of pyrophosphate ions on the conversion of calcium–lithium–borate glass to hydroxyapatite in aqueous phosphate solution.* Journal of Materials Science: Materials in Medicine, 2010. **21**(10): p. 2733-2741.

[20] Y. Gu, W. Xiao, L. Lu, W. Huang, M.N. Rahaman, and D. Wang, *Kinetics and mechanisms of converting bioactive borate glasses to hydroxyapatite in aqueous phosphate solution.* Journal of Materials Science, 2011. **46**(1): p. 47-54.

[21] Y. Shen, J.A. Semon, and R.K. Brow, *Hollow biphasic calcium phosphate microspheres from glass dissolution and reprecipitation; Part II: In vivo Studies of Bone Regeneration and Blood Vessel Formation.*

[22] T. Kokubo, H. Kushitani, S. Sakka, T. Kitsugi, and T. Yamamuro, *Solutions able to reproduce in vivo surface-structure changes in bioactive glass-ceramic A-W3.* Journal of biomedical materials research, 1990. **24**(6): p. 721-734.

[23] A. Mazzoli and O. Favoni, *Particle size, size distribution and morphological evaluation of airborne dust particles of diverse woods by Scanning Electron Microscopy and image processing program.* Powder Technology, 2012. **225**: p. 65-71.

[24] K.A. Gross, J. Andersons, M. Misevicius, and J. Svirksts, *Traversing phase fields towards nanosized beta tricalcium phosphate.* Key Engineering Materials, 2014. **587**: p. 97-100.

[25] N. Varadarajan, R. Balu, D. Rana, M. Ramalingam, and T. Kumar, *Accelerated sonochemical synthesis of calcium deficient hydroxyapatite nanoparticles: structural and morphological evolution.* Journal of Biomaterials and Tissue Engineering, 2014. **4**(4): p. 295-299.

[26] R.Z. LeGeros, S. Lin, R. Rohanizadeh, D. Mijares, and J.P. LeGeros, *Biphasic calcium phosphate bioceramics: preparation, properties and applications.* Journal of Materials Science: Materials in Medicine, 2003. **14**(3): p. 201-209.

[27] L. Berzina-Cimdina and N. Borodajenko, *Research of calcium phosphates using Fourier transform infrared spectroscopy*, in *Infrared Spectroscopy-Materials Science, Engineering and Technology*. 2012, IntechOpen.

[28] A. Destainville, E. Champion, D. Bernache-Assollant, and E. Laborde, *Synthesis, characterization and thermal behavior of apatitic tricalcium phosphate.* Materials Chemistry and Physics, 2003. **80**(1): p. 269-277.

[29] P. De Aza, F. Guitian, C. Santos, S. De Aza, R. Cusco, and L. Artus, *Vibrational properties of calcium phosphate compounds. 2. Comparison between hydroxyapatite and β-tricalcium phosphate.* Chemistry of Materials, 1997. **9**(4): p. 916-922.

[30] F. Bakan, *A Systematic Study of the Effect of pH on the Initialization of Ca-deficient Hydroxyapatite to β-TCP Nanoparticles.* Materials (Basel, Switzerland), 2019. **12**(3): p. 354.

[31] D.-H. Kim, K.-H. Hwang, J.D. Lee, H.-C. Park, and S.-Y. Yoon, *Long and short range order structural analysis of in-situ formed biphasic calcium phosphates.* Biomaterials Research, 2015. **19**(1): p. 14.

[32] P. Ducheyne, *Comprehensive biomaterials II*. 2017: Elsevier.

[33] T.R. Machado, J.C. Sczancoski, H. Beltrán-Mir, M.S. Li, J. Andrés, E. Cordoncillo, E. Leite, and E. Longo, *Structural properties and self-activated photoluminescence emissions in hydroxyapatite with distinct particle shapes.* Ceramics International, 2018. **44**(1): p. 236-245.

[34] A. Awonusi, M.D. Morris, and M.M.J. Tecklenburg, *Carbonate Assignment and Calibration in the Raman Spectrum of Apatite.* Calcified Tissue International, 2007. **81**(1): p. 46-52.

[35] L. Borkowski, A. Sroka-Bartnicka, P. Drączkowski, A. Ptak, E. Zięba, A. Ślósarczyk, and G. Ginalska, *The comparison study of bioactivity between composites containing synthetic non-substituted and carbonate-substituted hydroxyapatite.* Materials Science and Engineering: C, 2016. **62**: p. 260-267.

[36] Q. Wang, W. Huang, D. Wang, B.W. Darvell, D.E. Day, and M.N. Rahaman, *Preparation of hollow hydroxyapatite microspheres.* Journal of Materials Science: Materials in Medicine, 2006. **17**(7): p. 641-646.

[37] K.P. Fears, *Formation of hollow hydroxyapatite microspheres*. Masters Theses, Missouri University of Science and Technology, 2001.

[38] K. Salma, L. Berzina-Cimdina, and N. Borodajenko, *Calcium phosphate bioceramics prepared from wet chemically precipitated powders.* Processing and Application of Ceramics, 2010. **4**(1): p. 45-51.

[39] Y. Song, H.H. Hahn, and E. Hoffmann, *Effects of solution conditions on the precipitation of phosphate for recovery: A thermodynamic evaluation.* Chemosphere, 2002. **48**(10): p. 1029-1034.

[40] M.H. Veléz, H.L. Tuller, and D.R. Uhlmann, *Chemical durability of lithium borate glasses.* Journal of Non-Crystalline Solids, 1982. **49**(1): p. 351-362.

[41] J.D. Lowry, *Dissolution behavior of alkali borate glasses*. Masters Theses, Missouri University of Science and Technology, 2002.

[42] V. Čadež, I. Erceg, A. Selmani, D.D. Jurašin, S. Šegota, D.M. Lyons, D. Kralj, and M. Dutour Sikirić, *Amorphous calcium phosphate formation and aggregation process revealed by light scattering techniques.* Crystals, 2018. **8**(6): p. 254.

[43] H. Fu, M.N. Rahaman, D.E. Day, and R.F. Brown, *Hollow hydroxyapatite microspheres as a device for controlled delivery of proteins.* Journal of Materials Science: Materials in Medicine, 2011. **22**(3): p. 579-591.

[44] S.-C. Liou and S.-Y. Chen, *Transformation mechanism of different chemically precipitated apatitic precursors into β-tricalcium phosphate upon calcination.* Biomaterials, 2002. **23**(23): p. 4541-4547.

[45] M. Ebrahimi, M.G. Botelho, and S.V. Dorozhkin, *Biphasic calcium phosphates bioceramics (HA/TCP): Concept, physicochemical properties and the impact of standardization of study protocols in biomaterials research.* Materials Science & Engineering C, 2017. **71**: p. 1293-1312.

[46] T. Kokubo and H. Takadama, *How useful is SBF in predicting in vivo bone bioactivity?* Biomaterials, 2006. **27**(15): p. 2907-2915.

III. HOLLOW BIPHASIC CALCIUM PHOSPHATE MICROSPHERES FROM GLASS DISSOLUTION AND REPRECIPITATION; PART II: IN VIVO STUDIES OF BONE REGENERATION AND BLOOD VESSEL FORMATION

Youqu Shen[1], Julie Semon[2], and Richard K. Brow[1]

[1]Department of Materials Science and Engineering, Missouri University of Science and Technology, Rolla, MO 65409

[2]Department of Biological Sciences, Missouri University of Science and Technology, Rolla, MO 65409

ABSTRACT

Hollow Ca-deficient hydroxyapatite (CDHA) microspheres were prepared by a glass dissolution/reprecipitation reaction, and converted through heat-treatments to biphasic calcium phosphate (BCP) microspheres. By varying the pH of the solution used to convert the glass to CDHA, BCP particles with different fractions of hydroxyapatite (HA) and tricalcium phosphate (β-TCP) could be prepared. CDHA and BCP microspheres were implanted in rat calvarial defects and after 8 weeks, the BCP microspheres with a β-TCP/HA ratio of 70/30 (by weight) promoted a greater fraction of new bone formation (33 ± 7%) compared to BCP microspheres with a β-TCP/HA ratio of 44/56 (20 ± 9%) and to the respective CDHA microspheres (17 ± 4%, 17 ± 5). Bone formation was not observed in the subcutaneous implants of any types of these microspheres, after 8 weeks and 12 weeks, and so the microspheres are not osteoinductive. However, the more reactive BCP microspheres (β-TCP/HA=70/30) were associated with significantly more blood vessel formation in the subcutaneous implants.

1. INTRODUCTION

Over the past several decades, calcium phosphate materials have been developed for clinical applications to promote regeneration in osteo-defects [1-3]. In particular, biphasic calcium phosphate (BCP) materials that combine hydroxyapatite (HA) and β-tricalcium phosphate (β-TCP) phases have served as bone graft substitutes in orthopedics [4-7].

In general, HA is poorly bioresorbable, whereas β-TCP is more bioresorbable and can be replaced by new bone at faster rates [3, 6, 7]. Therefore, the chemical properties of BCP materials can be tailored by the relative concentrations of the individual phases [2, 4, 6-8]. The Ca/P atomic ratios in BCP materials range from 1.5 for pure β-TCP to 1.67 for pure HA. BCP ceramics have been used to produce biocompatible scaffolds, where the level of bioactivity, bioresorbability, osteoconductivity, and osteoinductivity could be adjusted by varying the β-TCP/HA ratio [4-7]. Various BCP products with different β-TCP/HA ratios have been evaluated in large number of studies, but there is no agreement on the optimal β-TCP/HA ratio for clinical applications [6].

Previous studies [9-11] have shown that the hollow HA microspheres alone have limited capacity for bone regeneration, likely because they were composed of chemically stable HA or CDHA. In Part I of this study [12], CDHA microspheres were produced by a glass conversion technique and hollow BCP microspheres with different β-TCP/HA ratios were produced by heat-treating the CDHA microspheres. The composition and microstructure of the microspheres was affected by the concentration and pH value of the phosphate solution used in the glass conversion process.

The objective of the present paper is to characterize the *in vivo* performance of the hollow CDHA and BCP microspheres. CDHA microspheres with different Ca/P ratios produce BCP microspheres with different β-TCP/HA ratios. The microspheres were implanted in rat calvarial defects for 8 weeks and subcutaneous defects for 8 and 12 weeks, and their bioactive performances were evaluated.

2. MATERIALS AND METHODS

2.1. PREPARATION AND CHARACTERIZATION OF HOLLOW BIPHASIC CALCIUM PHOSPHATE MICROSPHERES

The preparation of CDHA and BCP microspheres used here is described in Part I of this study [12]. Briefly, hollow CDHA microspheres were prepared by reacting glass microspheres (composition $11Li_2O$, 15CaO and $74B_2O_3$ (wt%), 150- 250 μm in diameter) in 0.1 M K_2HPO_4 solutions with pH values of 7 and 12 at 37°C for 4 days. The converted microspheres were washed with distilled water and anhydrous ethanol, and then dried at room temperature for at least 12 h, and at 90 °C for at least 12 h. After conversion, some of the CDHA microspheres were converted to BCP microspheres by heating them in a platinum dish in air at 800°C for 5 hours.

Table 1 lists the properties of the hollow microspheres used in this study. Samples prepared in a phosphate solution with a pH of 7 had Ca/P atomic ratios of 1.55 and after the heat treatment, converted to BCP microspheres with an β-TCP/HA ratio of 70/30 (by weight), whereas samples prepared in a phosphate solution with a pH of 12 had Ca/P atomic ratios of 1.59 and after the heat treatment, converted to BCP microspheres with a

β-TCP/HA ratio of 44/56. Prior to implantation, all microspheres were sterilized by immersing in anhydrous ethanol and then exposing them to ultraviolet light for 15 min.

2.2. *IN VIVO* STUDIES OF CDHA AND BCP MICROSPHERES

All animal use and care procedures were approved by the Missouri S&T Institutional Animal Care and Use Committee in compliance with the NIH Guide for Care and Use of Laboratory Animals (1985). Male Sprague-Dawley (SD) rats, three months old, were used. Before surgery, the animals were acclimated for two weeks to diet, water, and housing under a 12 h/12 h light/dark cycle. The rats were anesthetized with a combination of isoflurane and oxygen. The surgery area on each animal was shaved, scrubbed with 70% ethanol and iodine, and draped. Calvarial defects and subcutaneous defects were implanted with one of the four groups of microspheres described in the previous section. The microspheres were sterilized by immersing in anhydrous ethanol and then exposing them to ultraviolet light for 15 min, prior to implantation.

2.2.1. Calvarial Defects. For the calvarial defects, sterile instruments and aseptic techniques were used to create a 1 cm cranial skin incision in an anterior-to-posterior direction along the midline. The subcutaneous tissue, musculature and periosteum were dissected and reflected to expose the calvaria. Bilateral full thickness defects (4.6 mm in diameter) were created in the central area of each parietal bone using a saline-cooled trephine drill. The sites were constantly irrigated with sterile phosphate-buffered saline to prevent overheating of the bone margins and to remove the bone debris. Each defect was randomly implanted with 10 mg of microspheres from each group listed in Table 1. After

the implantation of the microspheres, one drop of Ringer's solution was added to each defect. The periosteum and skin were repositioned and closed with wound clips. Each animal received an intramuscular injection of ~200 µl buprenorphine and ~200 µl penicillin post-surgery. All animals were monitored daily for the condition of the surgical wound, food intake, activity and clinical signs of infection. After 8 weeks, the animals were sacrificed by CO_2 inhalation, and the calvarial defect sites with surrounding bone and soft tissue were harvested for subsequent evaluations.

2.2.2. Subcutaneous Defects. For the subcutaneous implants, the microspheres were implanted at random implant sites to remove any bias from a single rat. Each rat had four implant sites, two inferior to the shoulders and two superior to the hind legs. An incision approximately 2 cm in length was made completely through the dermal tissue perpendicular to the spine with a pair of SuperCut surgical scissors. Then, a skin retractor was gently inserted into the incision to create a pocket between the cutaneous tissue and the skeletal muscle. Each pocket was randomly implanted with 20 mg of the microspheres from each group listed in Table 1, and the skin was then closed with wound clips. All rats received the same post-surgery care and monitoring as those in the calvarial implantation study. At the predetermined time points (8 weeks or 12 weeks), the animals were sacrificed and the subcutaneous defect sites with surrounding soft tissue were harvested for subsequent evaluations.

2.2.3. Histological Processing. Harvested calvarial samples and subcutaneous samples were fixed in a 10% neutral buffer formalin solution for five days. All samples were cut in the middle after being washed with deionized water. The samples were decalcified in 14 wt% ethylenediaminetetraacetic acid (Sigma-Aldrich, USA) for 2

weeks, dehydrated in ethanol, and then embedded in paraffin using standard histological techniques. These samples were sectioned using a microtome (Leica RM 2235, Germany). The thickness of the tissue section with paraffin was 5 μm. These slices were then stained with hematoxylin and eosin (H&E).

2.2.4. Histomorphometric Analysis. The stained sections were viewed using an optical microscope (KH-8700, Hirox-USA) and analyzed by Image J software (National Institutes of Health, USA).

For calvarial samples, the percentages of new bone and residual microspheres in the defect were evaluated from the H&E stained sections. The total defect area was measured from one edge of the old calvarial bone, including the entire implant and tissue within it, to the other edge of the old bone. The newly formed bone and residual microspheres within this area were then outlined and measured. The amount of the new bone formation and residual microspheres were expressed as a percentage of the total defect area.

For subcutaneous samples, the blood vessels and foreign body giant cells were examined based on the H&E stained sections. The total defect area containing all the microspheres and tissue within them was identified, and blood vessels and foreign body giant cells were outlined, measured, and presented as a percentage of the total defect area.

2.3. STATISTICAL ANALYSIS

Measurements of the percentage of new bone or blood vessel formation (relative to the entire defect area) were expressed as a mean ± SD. Analysis for differences

between groups was performed using one-way analysis of variance (ANOVA) followed by the Tukey's post hoc test; the differences were considered significant at $p < 0.05$.

3. RESULTS

3.1. HOLLOW CA-PHOSPHATE MICROSPHERES

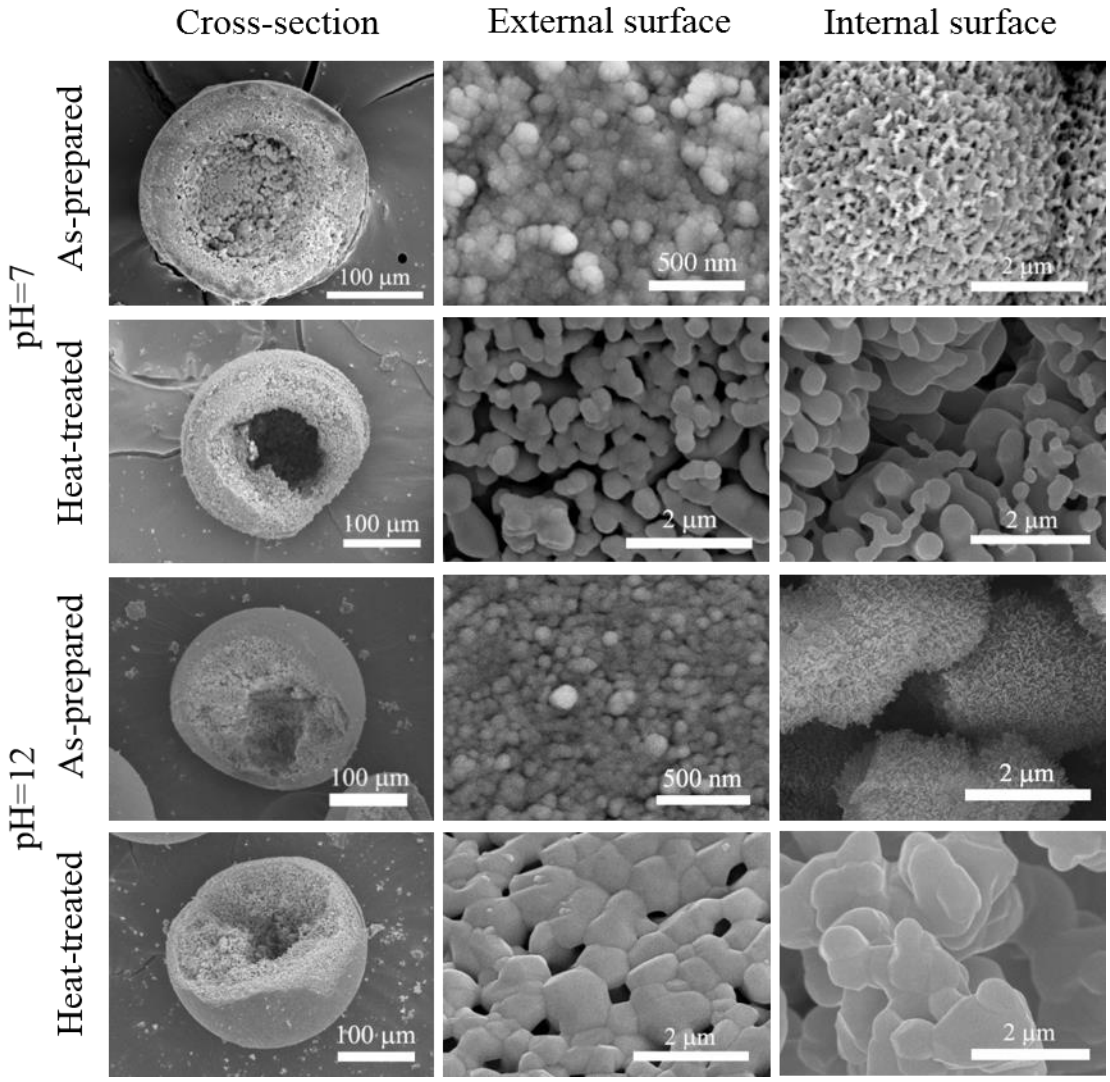

Figure 1. Electron micrographs of the cross-sections (left), external surfaces (center) and internal surfaces (right) of the CDHA and BCP hollow microspheres used in this study; from [12].

Table 1. Microspheres used for *in vivo* tests (rat calvarial implantation and subcutaneous implantation); compositions and properties are from [12].

Group	Microspheres						
	pH	Heat-treatment	Phase (wt%)	Ca/P atomic ratio	Surface Area (m^2/g)	Pore size (nm)	Sample size (n)
1	7	-	CDHA	~1.55	147.4 ± 1.4	14 ± 0.1	6
2	7	800 °C / 5h	70 β-TCP 30 HA	~1.55	3.6 ± 0.1	6.8 ± 0.6	6
3	12	-	CDHA	~1.59	148.2 ± 2.3	148.2 ± 2.3	6
4	12	800 °C / 5h	44 β-TCP 56 HA	~1.59	6.6 ± 0.2	6.6 ± 0.2	6

Figure 1 shows representative scanning electron microscopic images of the CDHA and BCP microspheres used in this study, and Table 1 lists some of their properties [12]. The diameter ratios of hollow core to outer surface were ~0.53. Samples prepared in a phosphate solution with a pH of 7 had Ca/P atomic ratios of 1.55, and after the heat treatment, converted to BCP microspheres with an β-TCP/HA ratio of 70/30 (by weight), whereas samples prepared in a phosphate solution with a pH of 12 had Ca/P atomic ratios of 1.59, and after the heat treatment, converted to BCP microspheres with an β-TCP/HA ratio of 44/56. The CDHA microspheres are formed from particles about 100 nm in diameter [12] that form high surface areas (about 150 m^2/g) with nanoporosity (Table 1). After heat treatments, the CDHA particles transform to larger β-TCP and HA grains, and there is a substantial loss of surface area (4-7 m^2/g), although the walls retain nanoporosity (Table 1).

3.2. CALVARIAL IMPLANTATION

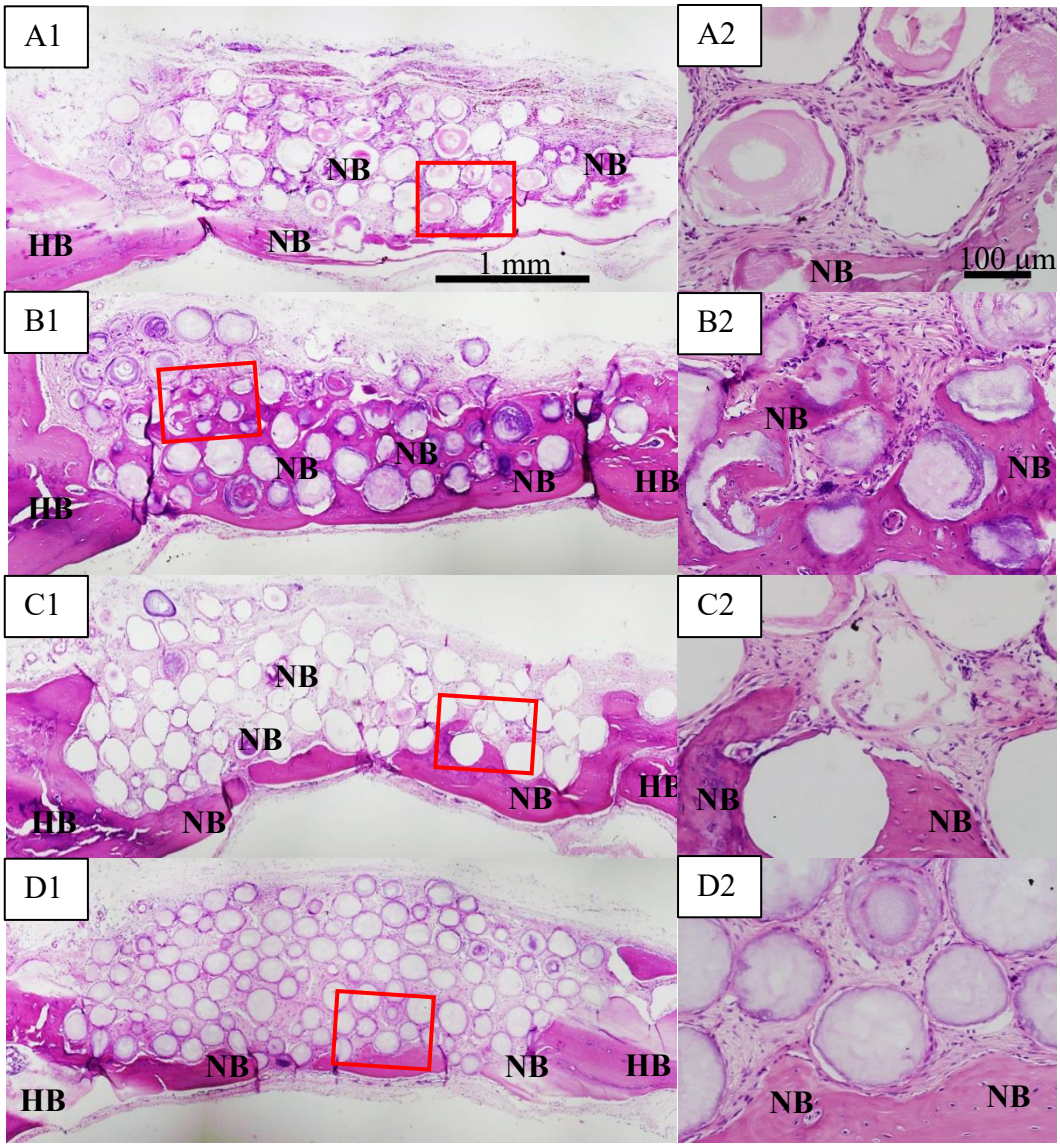

Figure 2. Optical images of H&E stained sections of rat calvarial defects implanted with four groups of microspheres at 8 weeks. (A1) CDHA/pH=7; (B1) BCP/pH=7; (C) CDHA/pH=12; (D) BCP/pH=12. (A2-D2) Higher-magnification images of outlined areas in (A1-D1). HB=host bone; NB=new bone.

H&E stained sections from the rat calvarial defects implanted with four groups of microspheres after 8 weeks are shown in Figure 2. The areal fractions of new bone

formation and residual microspheres are summarized in Table 2. In general, the fractions of residual microspheres remaining increased in the order (BCP/pH=7) < (BCP/pH=12) < (CDHA/pH=7) = (CDHA/pH=12), whereas new bone formation increased in the opposite order (CDHA/pH=7) = (CDHA/pH=12) < (BCP/pH=12) < (BCP/pH=7).

Table 2. Summary of areal fractions of new bone formation and residual microspheres in rat calvarial defects 8 weeks after implantation.

Implant type	Percent new bone (%)	Percent residual microspheres (%)
CDHA/pH=7	17 ± 4	31 ± 6
BCP/pH=7	33 ± 7	23 ± 4
CDHA/pH=12	17 ± 5	32 ± 6
BCP/pH=12	20 ± 9	29 ± 3

Figure 3A presents the data from Table 2 and shows that after eight weeks of implantation, the fraction of new bone formation associated with the BCP/pH=7 (70 wt% β-TCP) microspheres was statistically greater than what formed around the other implants ($n = 6$, $p < 0.05$, Figure 3A). For the CDHA microspheres and BCP/pH=12 (44 wt% β-TCP) microspheres, the new bone growth was limited to the periphery of the defects (edges and the bottom of the defects), and connective tissue filled the majority of these defects (Figure 2). There was no significant difference in new bone formation between these three groups ($n = 6$, $p > 0.05$).

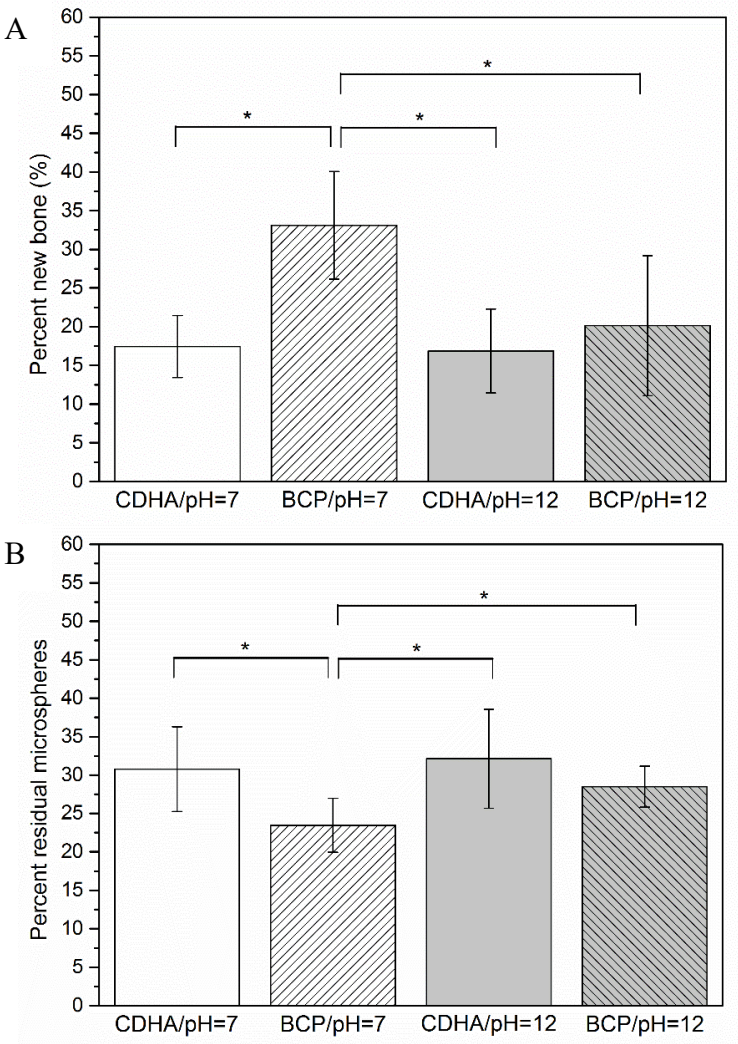

Figure 3. A comparison of A) new bone formation, and B) residual microspheres, as a percentage of the total defect area, in rat calvarial defects implanted with four group of microspheres at 8 weeks. (Mean ± SD; n = 6, * significant difference between groups; $p < 0.05$).

Figure 2 shows that residual microspheres remain in the calvarial defects after eight weeks implantation, and Figure 3B shows the respective cross-sectional areas of those microspheres. The areal fraction of residual BCP/pH=7 microspheres was significantly lower ($n = 6$, $p < 0.05$) than the residual fractions of the other three samples, and the enhanced *in vivo* reactivity of these particles is consistent with the greater fraction

of new bone formation around these particles. In fact, Figure 2B1 and B2 show that new bone or fibrous tissue has infiltrated into the hollow core of a number of the BCP/pH=7 microspheres, additional evidence for the enhanced reactivity of these particles.

3.3. SUBCUTANEOUS IMPLANTATION

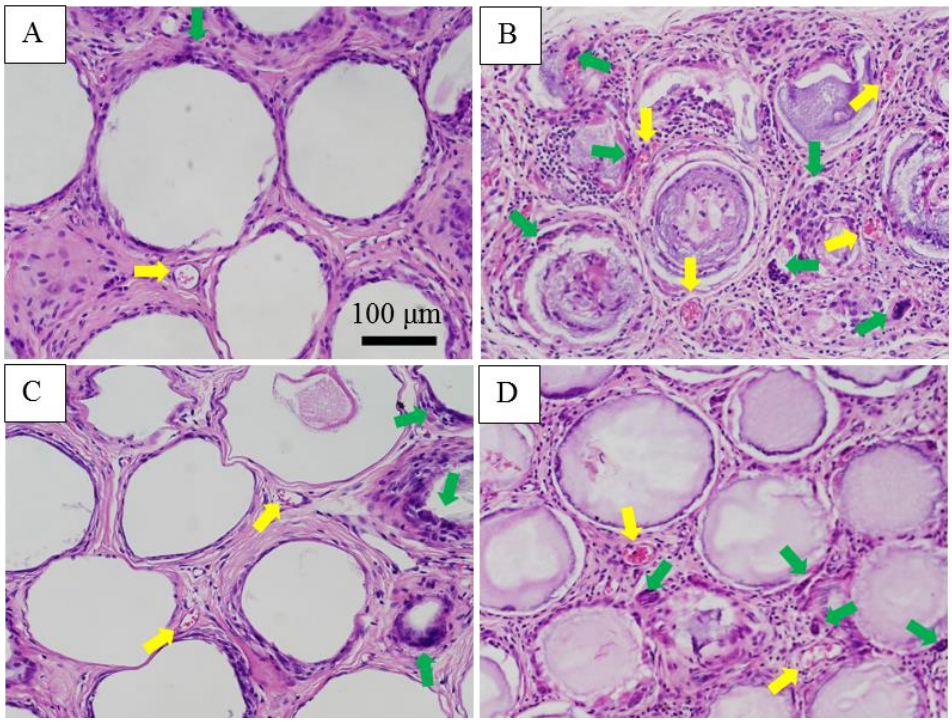

Figure 4. Optical images of H&E stained sections of rat subcutaneous defects implanted with four groups of microspheres at 8 weeks. (A) CDHA/pH=7; (B) BCP/pH=7; (C) CDHA/pH=12; (D) BCP/pH=12. Green arrows indicate multinuclear cells, yellow arrows indicate blood vessels.

The H&E stained sections of subcutaneous defects implanted with the four groups of microspheres are shown in Figure 4 after implantation for 8 weeks and in Figure 5, after 12 weeks. No new bone formation was observed around any of these implants and so there is no evidence for osteoinductivity by these CDHA and BCP microspheres. Cell

nuclei are blue, cytoplasm connective tissue and extra cellular matrix are purple or red, and red blood cells are bright red. The microspheres from all four groups are surrounded by connective tissue, some giant multinuclear cells (green arrows) and blood vessels (yellow arrows). Larger numbers of blood vessels and giant multinuclear cells are associated with the BCP microspheres than with the associated CDHA microspheres. The biodegradation rates of the BCP microspheres appear to be faster than the CDHA microspheres. Moreover, the BCP/pH=7 microspheres appear to have degraded faster than BCP/pH=12 microspheres.

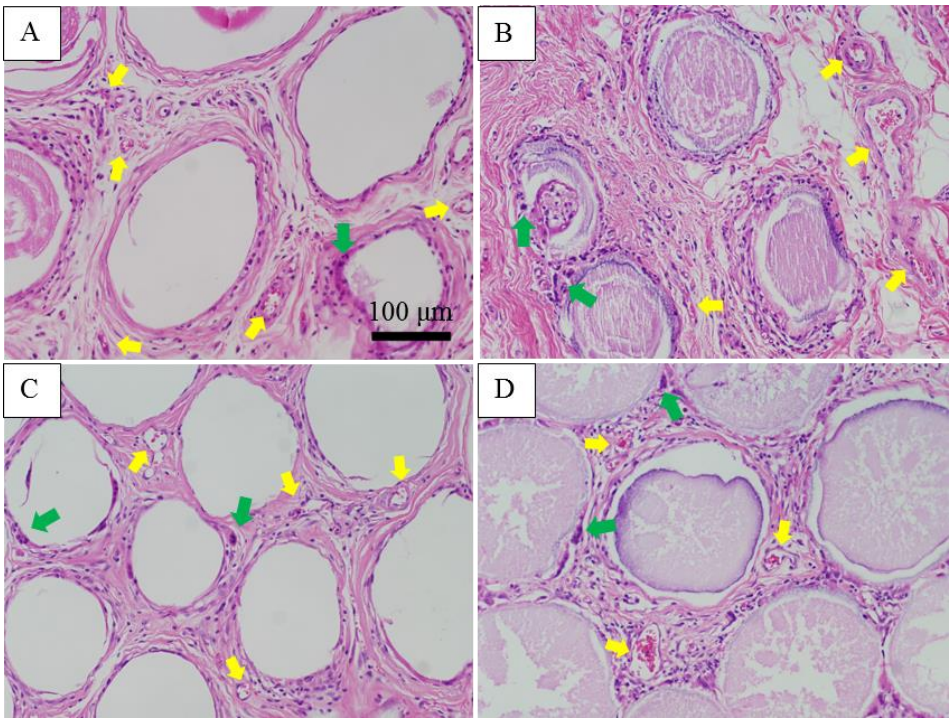

Figure 5. Optical images of H&E stained sections of rat subcutaneous defects implanted with four groups of microspheres at 12 weeks. (A) CDHA/pH=7; (B) BCP/pH=7; (C) CDHA/pH=12; (D) BCP/pH=12. Green arrows indicate multinuclear cells, yellow arrows indicate blood vessels.

Table 3. Summary of the areal fractions of blood vessels and foreign body giant cells in rat subcutaneous defects implanted with four groups of microspheres after 8 weeks and 12 weeks.

Implant	Blood vessels (%)	Foreign body giant cells (%)	Implantation time (weeks)
CDHA/pH=7	0.41 ± 0.22	0.48 ± 0.21	8
	0.49 ± 0.17	0.16 ± 0.08	12
BCP/pH=7	1.27 ± 0.36	1.09 ± 0.35	8
	1.43 ± 0.38	0.69 ± 0.28	12
CDHA/pH=12	0.32 ± 0.13	0.29 ± 0.09	8
	0.64 ± 0.28	0.19 ± 0.05	12
BCP/pH=12	0.64 ± 0.16	0.78 ± 0.33	8
	0.79 ± 0.28	0.38 ± 0.20	12

The percent area of blood vessels and foreign body giant cells in rat subcutaneous defects implanted for 8 weeks and 12 weeks with the microspheres from the four groups are summarized in Table 3. At 8 weeks, the areal fractions of blood vessels associated with the BCP microspheres are significantly enhanced relative to their respective CDHA microspheres ($n = 6$, $p < 0.05$, Figure 6A); the fraction of blood vessels formed in BCP/pH=7 microspheres was greater than those with the BCP/pH=12 microspheres, although the difference was not significant ($n = 6$, $p > 0.05$). After 12-weeks implantation, blood vessel formation increased for all groups compared to the 8-weeks implantation, although the increases were not significant ($n = 6$, $p > 0.05$). The area around the BCP/pH=7 microspheres had significantly more blood vessels than the areas

around the microspheres in other three groups (n = 6, $p < 0.05$). Furthermore, there was no significant difference in the formation of blood vessels between CDHA groups and BCP/pH=12 microspheres (n = 6, $p > 0.05$).

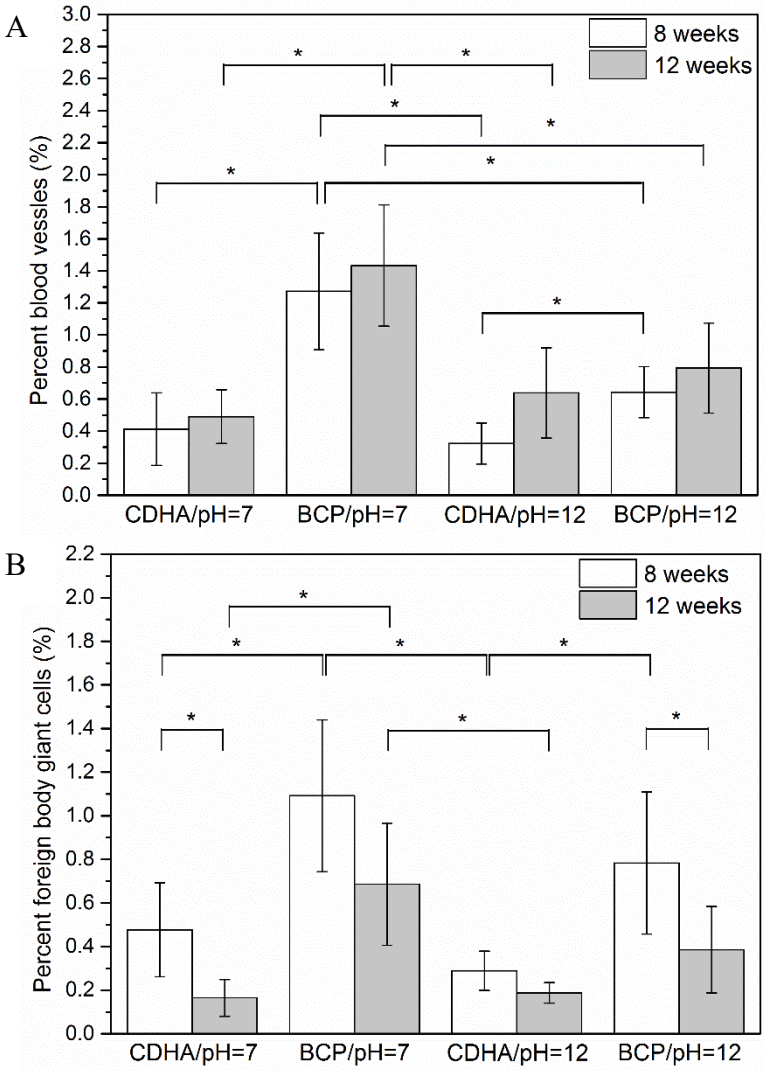

Figure 6. Comparative areal fractions of blood vessels and foreign body giant cells in implants with the four groups of microspheres after 8 weeks and 12 weeks in rat subcutaneous defects (Mean ± SD; n = 6, * significant difference between groups; $p < 0.05$).

Figure 6B shows that after eight weeks in the sub-cutaneous implants, the areal fractions of foreign body giant cells associated with the BCP microspheres were significantly greater than those associated with their respective CDHA microspheres ($n = 6$, $p < 0.05$). There was no significant difference in the presence of foreign body giant cells between the two BCP groups, and no significant difference between the two CDHA groups, as well. The fractions of foreign body giant cells decreased between 8 weeks and 12 weeks for all four groups, significantly for the CDHA/pH=7 and BCP/pH=12 microspheres. Additionally, the foreign body giant cells associated with the BCP/pH=7 microspheres were significantly greater than those associated with the other three groups.

4. DISCUSSION

4.1. *IN VIVO* DEGRADATION

The response of a body to the implantation of calcium phosphate materials includes the diffusion of biological fluid and then cellular colonization. The cells for bioresorption include monocytes, macrophages, giant cells, osteoclasts, and fibroblast, and the cells for tissue repair include osteogenic cells [2, 4, 13]. Therefore, for the *in vivo* studies, cell-mediated degradation also needs to be considered. The chemical properties of calcium phosphate materials, such as solubility, influence the bioresorption ability. For BCP, the resorption activity is influenced by the ratio of β-TCP/HA [4, 5, 14]. In general, the greater the ratio of β-TCP/HA, the greater the bioresorption ability. This was confirmed in Part 1 of this study, where it was shown that the BCP microspheres with 70 wt% β-TCP dissolved faster in an acetic acid solution than the BCP microspheres with 44

wt% β-TCP, and both dissolved faster than the respective CDHA microspheres, despite the much greater surface areas of the latter [12]. The bioresorption of the calcium phosphate is mainly regulated by osteoclasts in calvarial defects and macrophages in subcutaneous defects. The osteoclasts, a type of bone cell, are involved in the maintenance, repair and remodeling of the skeleton. These cells are able to release small amounts of hydrochloric acid at material surfaces leading to a local pH change and the dissolution of calcium phosphate [15].

In the *in vivo* studies, in both the calvarial defects and subcutaneous defects, it is clear that the BCP microspheres with 70 wt% β-TCP degraded faster than the other groups of microspheres (Figures 2, 4 and 5). For example, the residual fraction of microspheres in the calvarial defects implanted with BCP microspheres with 70 wt% β-TCP was significantly lower than those of other groups (Figure 3B). In the subcutaneous defects, there was a greater number of foreign body giant cells associated with the same group of BCP microspheres with 70 wt% β-TCP (Figure 6B). The foreign body giant cells are a collection of fused macrophages that respond to the biomaterials [16]. The macrophages fused together to form giant cells at the biomaterial interface to digest the microspheres.

4.2. BONE REGENERATION *IN VIVO*

4.2.1. Bone Regeneration in Calvarial Defects. The great interest in the use of BCP (β-TCP/HA) materials for bone regeneration is based on the preferential dissolution of the β-TCP phase. By adjusting the β-TCP/HA ratio, the resorption rate of the implant, and its replacement by new bone, can be controlled [6, 7]. In the present study, bone

regeneration in calvarial defects implanted with BCP and CDHA microspheres were evaluated after 8 weeks. The BCP microspheres with 70 wt% β-TCP significantly enhanced new bone formation compared with BCP microspheres with 44 wt% β-TCP, and with the CDHA microspheres.

As mentioned before, the BCP microspheres with 70 wt% β-TCP degraded faster in the animals, releasing more Ca and phosphate ions. Those ions may trigger the osteogenic differentiation and participate in new bone formation. For example, the release of calcium ions could affect the osteoblast viability, proliferation and differentiation [17]. The osteoblastic differentiation of mesenchymal stem cells (MSCs) is accompanied by the expression of calcium ion binding proteins and the incorporation of calcium ions into the extracellular matrix [18]. Moreover, the phosphate ions act as a specific signal affecting various gene expressions implicated in skeletal cell proliferation, differentiation, mineralization, and apoptosis [19]. In addition, with faster degradation, the BCP microspheres with 70 wt% β-TCP provided more available space for the infiltration of cells and new bone formation.

Furthermore, the surface roughness of the microspheres might be a factor for bone regeneration. Compared to the CDHA microspheres with smooth external surfaces, the surfaces of BCP microspheres were topologically rougher (Figure 1). A rougher surface could be a more suitable substrate for cell attachment, proliferation and differentiation.

4.2.2. No Bone Regeneration in Subcutaneous Defects. The microspheres were implanted in subcutaneous defects for 8 weeks and 12 weeks and there were no signs of new bone formation associated with any of these samples. In the literature, BCP materials have shown potential for osteoinductivity, however, not all BCP products can produce

new bone formation in non-osseous defects [6]. The osteoinduction phenomenon of BCPs is affected on the animal species. The observation of osteoinduction has been frequently reported in large animals[20-24], such as goats, pigs, dogs, while rarely in small animals [24-26], such as rabbits, mice, and rats until 120 days. Our microspheres of BCP or CDHA did not induce any new bone in the rat subcutaneous defects within 12 weeks. This is accordance with the previous *in vivo* studies using rats [24, 27].

4.3. BLOOD VESSEL FORMATION IN SUBCUTANEOUS DEFECTS

For subcutaneous implantation, blood vessel formation increased between 8 weeks and 12 weeks for all groups of microspheres, and more blood vessels were formed in the defects implanted with BCP microspheres than CDHA microspheres (Figure 6A). BCP microspheres with faster degradation rates could provide more calcium ions, which play an important role in angiogenesis [28]. The BCP microspheres were also associated with greater inflammation, where multinucleated giant cells fused from macrophages could secrete vascular endothelial factor (VEGF), an important element in the development and maintenance of vascularization [29, 30]. Together, these could enhance blood vessel formation in subcutaneous defects implanted with BCP microspheres.

Vascularization induced by implanted biomaterials is a key factor for tissue repair, where blood flow supplies sufficient nutrition and growth factors needed for tissue repair. Angiogenesis and osteogenesis are intimately linked, and it has been suggested that both processes need to be properly regulated for bone regeneration [31-35]. Thus, BCP microspheres with enhanced ability to form blood vessels have the potential for bone and tissue regeneration.

4.4. INFLAMMATION IN THE SUBCUTANEOUS DEFECTS

The properties of biomaterials, including surface properties, particle size, porosity and pore size, and the release of bioactive ions, could affect the functionality of immune cells [36]. The surface properties, such as wettability, charge, topography, and roughness will affect the adhesion of immune cells. Larger pore sizes in a biomaterial can enhance angiogenesis but inhibit inflammation. Some bioactive ions, such as calcium, have immunoregulatory effects. Calcium ions have been found to be involved in certain inflammatory signaling pathways. The upregulation and downregulation of inflammatory responses could be affected by the concentration of calcium ions [37, 38]. The immune cells not only could lead to inflammation, but also could release cytokines that regulate osteogenesis. Therefore, a favorable immune reaction creates an osteogenic microenvironment that can improve osteogenesis. However, an inappropriate immune reaction may lead to the chronic inflammation and the formation of a fibrous capsule around the biomaterials [36, 39].

In this study, the BCP microspheres implanted in the subcutaneous defects induced stronger inflammatory response with foreign body giant cells than did the CDHA microspheres (Figure 6B). Moreover, the level of inflammatory response in all groups decreased between 8 weeks and 12 weeks (Figure 6B). Malard et al. [40] demonstrated that BCP particles with faster degradation rates led to better bone ingrowth and stronger inflammatory response. These results also suggest that the inflammatory response could be controlled by modifying the composition of the BCP particles.

4.5. POTENTIAL APPLICATIONS

The BCP microspheres prepared in this study have some unusual properties compared to other BCP granules. The BCP microspheres are nanoporous [12], which should promote cell attachment and proliferation. When some part of the microsphere shell is resorbed, the hollow core is exposed, which could provide more available space for cell infiltration. The hollow BCP microspheres could also be used as devices for adsorption of proteins and drug delivery. For bone repair, the BCP microspheres could be loaded with some growth factors, such the bone morphogenetic proteins (BMPs) [41, 42].

5. CONCLUSIONS

Two sets of CDHA microspheres (Ca/P≈ 1.55 and 1.59) and the corresponding BCP microspheres (β-TCP/HA =70/30 and 44/56) were implanted in both calvarial and subcutaneous sites. The BCP microspheres with 70 wt% β-TCP showed faster degradation rates, and the ability to enhance new bone formation in rat calvarial defects, and to promote blood vessel formation in rat subcutaneous defects, compared to the other groups of microspheres.

ACKNOWLEDGMENT

The authors thank Richard Watters (Missouri S&T Animal Research Facility) for his assistance with the animal tests and YS appreciates the financial support of the Lasko Endowment in the Materials Science and Engineering Department.

REFERENCES

[1] V. Campana, G. Milano, E. Pagano, M. Barba, C. Cicione, G. Salonna, W. Lattanzi, and G. Logroscino, *Bone substitutes in orthopaedic surgery: from basic science to clinical practice.* Journal of Materials Science: Materials in Medicine, 2014. **25**(10): p. 2445-2461.

[2] S.V. Dorozhkin, *Calcium orthophosphate-based bioceramics.* Materials, 2013. **6**(9): p. 3840-3942.

[3] S.V. Dorozhkin, *Calcium orthophosphates (CaPO4): occurrence and properties.* Progress in Biomaterials, 2016. **5**(1): p. 9-70.

[4] G. Daculsi, *Biphasic calcium phosphate concept applied to artificial bone, implant coating and injectable bone substitute.* Biomaterials, 1998. **19**(16): p. 1473-1478.

[5] S.V. Dorozhkin, *Biphasic, triphasic and multiphasic calcium orthophosphates.* Acta Biomaterialia, 2012. **8**(3): p. 963-977.

[6] M. Ebrahimi, M.G. Botelho, and S.V. Dorozhkin, *Biphasic calcium phosphates bioceramics (HA/TCP): Concept, physicochemical properties and the impact of standardization of study protocols in biomaterials research.* Materials Science & Engineering C, 2017. **71**: p. 1293-1312.

[7] R.Z. LeGeros, S. Lin, R. Rohanizadeh, D. Mijares, and J.P. LeGeros, *Biphasic calcium phosphate bioceramics: preparation, properties and applications.* Journal of Materials Science: Materials in Medicine, 2003. **14**(3): p. 201-209.

[8] L. Wang and G.H. Nancollas, *Calcium orthophosphates: Crystallization and Dissolution.* Chemical Reviews, 2008. **108**(11): p. 4628-4669.

[9] W. Xiao, H. Fu, M.N. Rahaman, Y. Liu, and B.S. Bal, *Hollow hydroxyapatite microspheres: A novel bioactive and osteoconductive carrier for controlled release of bone morphogenetic protein-2 in bone regeneration.* Acta Biomaterialia, 2013. **9**(9): p. 8374-8383.

[10] W. Xiao, B. Sonny Bal, and M.N. Rahaman, *Preparation of resorbable carbonate-substituted hollow hydroxyapatite microspheres and their evaluation in osseous defects in vivo.* Materials Science & Engineering C, 2016. **60**: p. 324-332.

[11] H. Fu, M.N. Rahaman, R.F. Brown, and D.E. Day, *Evaluation of bone regeneration in implants composed of hollow HA microspheres loaded with transforming growth factor β1 in a rat calvarial defect model.* Acta biomaterialia, 2013. **9**(3): p. 5718-5727.

[12] Y. Shen and R.K. Brow, *Hollow biphasic calcium phosphate microspheres from glass dissolution and reprecipitation. Part I: Particle formation and characterization*.

[13] N. Eliaz and N. Metoki, *Calcium phosphate bioceramics: A review of their history, structure, properties, coating technologies and biomedical applications.* Materials, 2017. **10**(4): p. 334.

[14] S. Yamada, D. Heymann, J.-M. Bouler, and G. Daculsi, *Osteoclastic resorption of calcium phosphate ceramics with different hydroxyapatite/β-tricalcium phosphate ratios.* Biomaterials, 1997. **18**(15): p. 1037-1041.

[15] S.L. Teitelbaum, *Bone Resorption by Osteoclasts.* Science, 2000. **289**(5484): p. 1504-1508.

[16] Z. Sheikh, P.J. Brooks, O. Barzilay, N. Fine, and M. Glogauer, *Macrophages, foreign body giant cells and their response to implantable biomaterials.* Materials, 2015. **8**(9): p. 5671-5701.

[17] S. Maeno, Y. Niki, H. Matsumoto, H. Morioka, T. Yatabe, A. Funayama, Y. Toyama, T. Taguchi, and J. Tanaka, *The effect of calcium ion concentration on osteoblast viability, proliferation and differentiation in monolayer and 3D culture.* Biomaterials, 2005. **26**(23): p. 4847-4855.

[18] I. Titorencu, V.V. Jinga, E. Constantinescu, A.V. Gafencu, C. Ciohodaru, I. Manolescu, C. Zaharia, and M.P. Simionescu, *Proliferation, differentiation and characterization of osteoblasts from human BM mesenchymal cells.* Cytotherapy, 2007. **9**(7): p. 682-696.

[19] S. Khoshniat, A. Bourgine, M. Julien, P. Weiss, J. Guicheux, and L. Beck, *The emergence of phosphate as a specific signaling molecule in bone and other cell types in mammals.* Cellular and Molecular Life Sciences, 2011. **68**(2): p. 205-218.

[20] H. Yamasaki and H. Sakai, *Osteogenic response to porous hydroxyapatite ceramics under the skin of dogs.* Biomaterials, 1992. **13**(5): p. 308-312.

[21] H. Yuan, Z. Yang, Y. Li, X. Zhang, J.D. De Bruijn, and K. De Groot, *Osteoinduction by calcium phosphate biomaterials.* Journal of Materials Science: Materials in Medicine, 1998. **9**(12): p. 723-726.

[22] H. Yuan, K. Kurashina, J.D. de Bruijn, Y. Li, K. De Groot, and X. Zhang, *A preliminary study on osteoinduction of two kinds of calcium phosphate ceramics.* Biomaterials, 1999. **20**(19): p. 1799-1806.

[23] H. Yuan, Y. Li, J.D. de Bruijn, K. de Groot, and X. Zhang, *Tissue responses of calcium phosphate cement: a study in dogs.* Biomaterials, 2000. **21**(12): p. 1283-1290.

[24] H. Yuan, C.A. Van Blitterswijk, K. De Groot, and J.D. De Bruijn, *Cross-species comparison of ectopic bone formation in biphasic calcium phosphate (BCP) and hydroxyapatite (HA) scaffolds.* Tissue engineering, 2006. **12**(6): p. 1607-1615.

[25] L. Cheng, Y. Shi, F. Ye, and H. Bu, *Osteoinduction of calcium phosphate biomaterials in small animals.* Materials Science & Engineering C, 2013. **33**(3): p. 1254-1260.

[26] L. Cheng, F. Ye, R. Yang, X. Lu, Y. Shi, L. Li, H. Fan, and H. Bu, *Osteoinduction of hydroxyapatite/β-tricalcium phosphate bioceramics in mice with a fractured fibula.* Acta Biomaterialia, 2010. **6**(4): p. 1569-1574.

[27] C. Klein, K. de Groot, W. Chen, Y. Li, and X. Zhang, *Osseous substance formation induced in porous calcium phosphate ceramics in soft tissues.* Biomaterials, 1994. **15**(1): p. 31-34.

[28] A. Aguirre, A. González, M. Navarro, Ó. Castaño, J.A. Planell, and E. Engel, *Control of microenvironmental cues with a smart biomaterial composite promotes endothelial progenitor cell angiogenesis.* European Cells and Materials, 2012. **24**: p. 90-106.

[29] J.M. Anderson, A. Rodriguez, and D.T. Chang. *Foreign body reaction to biomaterials*. in *Seminars in immunology*. 2008. Elsevier.

[30] S. Ghanaati, M. Barbeck, C. Orth, I. Willershausen, B.W. Thimm, C. Hoffmann, A. Rasic, R.A. Sader, R.E. Unger, F. Peters, and C.J. Kirkpatrick, *Influence of β-tricalcium phosphate granule size and morphology on tissue reaction in vivo.* Acta Biomaterialia, 2010. **6**(12): p. 4476-4487.

[31] A. Aguirre, J.A. Planell, and E. Engel, *Dynamics of bone marrow-derived endothelial progenitor cell/mesenchymal stem cell interaction in co-culture and its implications in angiogenesis.* Biochemical and Biophysical Research Communications, 2010. **400**(2): p. 284-291.

[32] J.M. Kanczler and R.O.C. Oreffo, *Osteogenesis and angiogenesis: The potential for engineering bone.* European Cells and Materials, 2008. **15**: p. 100-114.

[33] C.J. Kirkpatrick, S. Fuchs, and R.E. Unger, *Co-culture systems for vascularization — Learning from nature.* Advanced Drug Delivery Reviews, 2011. **63**(4): p. 291-299.

[34] H. Li, R. Daculsi, M. Grellier, R. Bareille, C. Bourget, M. Remy, and J. Amedee, *The role of vascular actors in two dimensional dialogue of human bone marrow stromal cell and endothelial cell for inducing self-assembled network.* PLoS ONE, 2011. **6**(2): p. e16767.

[35] A. Malhotra and P. Habibovic, *Calcium Phosphates and Angiogenesis: Implications and Advances for Bone Regeneration.* Trends in Biotechnology, 2016. **34**(12): p. 983-992.

[36] Z. Chen, T. Klein, R.Z. Murray, R. Crawford, J. Chang, C. Wu, and Y. Xiao, *Osteoimmunomodulation for the development of advanced bone biomaterials.* Materials Today, 2016. **19**(6): p. 304-321.

[37] A. De, *Wnt/Ca2+ signaling pathway: a brief overview.* Acta Biochim Biophys Sin, 2011. **43**(10): p. 745-756.

[38] R.J. MacLeod, M. Hayes, and I. Pacheco, *Wnt5a secretion stimulated by the extracellular calcium-sensing receptor inhibits defective Wnt signaling in colon cancer cells.* American Journal of Physiology - Gastrointestinal and Liver Physiology, 2007. **293**(1): p. G403-G411.

[39] Z. Julier, A.J. Park, P.S. Briquez, and M.M. Martino, *Promoting tissue regeneration by modulating the immune system.* Acta Biomaterialia, 2017. **53**: p. 13-28.

[40] O. Malard, J.M. Bouler, J. Guicheux, D. Heymann, P. Pilet, C. Coquard, and G. Daculsi, *Influence of biphasic calcium phosphate granulometry on bone ingrowth, ceramic resorption, and inflammatory reactions: Preliminary in vitro and in vivo study.* Journal of Biomedical Materials Research, 1999. **46**(1): p. 103-111.

[41] J.-W. Jang, J.-W. Jang, J.-H. Yun, K.-I. Lee, U.-W. Jung, C.-S. Kim, S.-H. Choi, and K.-S. Cho, *Osteoinductive activity of biphasic calcium phosphate with different rhBMP-2 doses in rats.* Oral Surgery, Oral Medicine, Oral Pathology and Oral Radiology, 2012. **113**(4): p. 480-487.

[42] S.P. Victor and T.S.S. Kumar, *BCP ceramic microspheres as drug delivery carriers: synthesis, characterisation and doxycycline release.* Journal of Materials Science: Materials in Medicine, 2008. **19**(1): p. 283-290.

IV. EVALUATION OF 13-93 GLASS SCAFFOLDS WITH CURVED FILAMENTS TO ENHANCE BONE FORMATION IN RAT CALVARIAL DEFECTS

Youqu Shen[1], Richard K. Brow[1], Mohamed N. Rahaman[1], Julie A. Semon[2]

[1]Department of Materials Science and Engineering, Missouri University of Science and Technology, Rolla, MO 65409

[2]Department of Biological Sciences, Missouri University of Science and Technology, Rolla, MO 65409

ABSTRACT

Scaffold architecture plays an important role in bone repair and there have been reports in the literature that the surface topology of an implant affects bone growth. Additive manufacturing techniques, like robocasting, allow the ready formation of complex scaffold architectures to optimize *in vivo* performance. The objective of this study was to compare scaffolds of 13-93 glass, produced by the robocasting technique, with straight filaments scaffolds to those with curved filament to determine if the modified topology of the latter promotes greater bone formation in rat calvarial defects. Scaffolds with curved-filaments had slightly larger pores (150 ± 5 μm × 70 ± 8 μm) and greater overall porosity (45 ± 3%) than scaffolds with straight filaments (155 ± 5 μm diameter, pore dimensions of 117 ± 3 μm × 75 ± 5 μm, porosity of 41 ± 2 %). After six weeks in the calvarial defects, scaffolds with curved filaments stimulated a greater amount of new bone formation (30 ± 5%), than the straight filament scaffolds (25 ± 4%). Scaffolds that were pre-reacted to form thin (6 ± 1 μm) surface layers of hydroxyapatite, prior to implantation, were more effective at stimulating new bone formation, with the

curved-filament structures again showing significant improvement in new bone growth (56 ± 13%) compared to the surface-modified straight-filament structures (40 ± 9%).

1. INTRODUCTION

There is a growing need for the development of synthetic bone grafts to repair bone defects caused by injury and disease [1, 2]. For common tissue engineering strategies, biomaterial scaffolds for bone repair are required to serve as templates to guide the regeneration of new bone [3, 4]. An effective scaffold needs to mimic the structure and properties of natural bone [5]. In bone tissue engineering, the selection of materials and the architectural design of the scaffolds are important issues for clinical applications [3, 6].

Bioactive glasses are widely used as scaffold materials for bone repair, due to their biocompatibility, osteoconductivity, their ability to form hydroxyapatite (HA) -like layers *in vivo*, and their ability to form a strong bond with the host bone. By adjusting the composition, a bioactive glass can release certain elements, such as boron [7], zinc [8, 9], copper [10, 11], and strontium [12], in a controlled manner that facilitates bone regeneration. Bioactive silicate glasses, including 45S5 [13, 14] and 13-93 [15-17], have been approved by the Food and Drug Administration (FDA) for *in vivo* use, and scaffolds based on these bioactive glasses can be fabricated with different architectures to provide desired mechanical and chemical environments for bone reconstruction.

Additive manufacturing techniques provide opportunities for innovative design and fabrication of scaffold architectures [18], and many studies have been done to relate

different scaffold designs to bone formation, including the effects of porosity [19], pore size [20], filament concavity [21], mechanical properties [22], and so on.

In our laboratory, porous bioactive glass scaffolds have been fabricated using different manufacturing techniques, their mechanical properties were tested *in vitro*, and their ability to support bone infiltration were tested *in vivo* [6, 23-27], including 13-93 glass scaffolds with "trabecular" [24], "oriented" [24], or "grid-like" [27] microstructures to facilitate bone regeneration in rat calvarial defects. Among these three microstructures, the 13-93 glass scaffolds with grid-like (straight filament) structures showed the most promising bone formation results after shorter implantation times (6 weeks) [27]. Moreover, 13-93 glass scaffolds that were pre-reacted in a phosphate solution to form a thin hydroxyapatite (HA)-like surface layer on the filaments, prior to implantation, showed significantly enhanced bone regeneration in six weeks [27].

Rumpler et al [28] described curvature-driven effects that promoted *in vivo* tissue formation in scaffolds, particularly on concave surfaces, and Paris et al. [19] developed a scaffold curvature-mediated mechanism for the *in vivo* bio-mineralization of extra-cellular matrix. In a recent study [29, 30], we showed that open HA microspheres with rough, porous and concave surfaces were more effective at promoting new bone formation than did closed HA microspheres with smooth and convex surfaces. Based on these results, we hypothesized that 13-93 glass scaffolds with curved filaments may have improved capability to regenerate bone *in vivo*.

The objective of this study is to evaluate the capability of 13-93 glass scaffolds with curved filaments to facilitate bone formation in an osseous (rat calvarial) defect model. Scaffolds with either straight filaments or curved filaments were fabricated by the

robocasting method using 13-93 glass powders that were then sintered to densify the filaments and to form filament-filament bonds. Some scaffolds were pre-reacted in a phosphate solution to form a thin HA-like layer, prior to implantation.

2. MATERIALS AND METHODS

2.1. PREPARATION OF 13-93 GLASS SCAFFOLDS

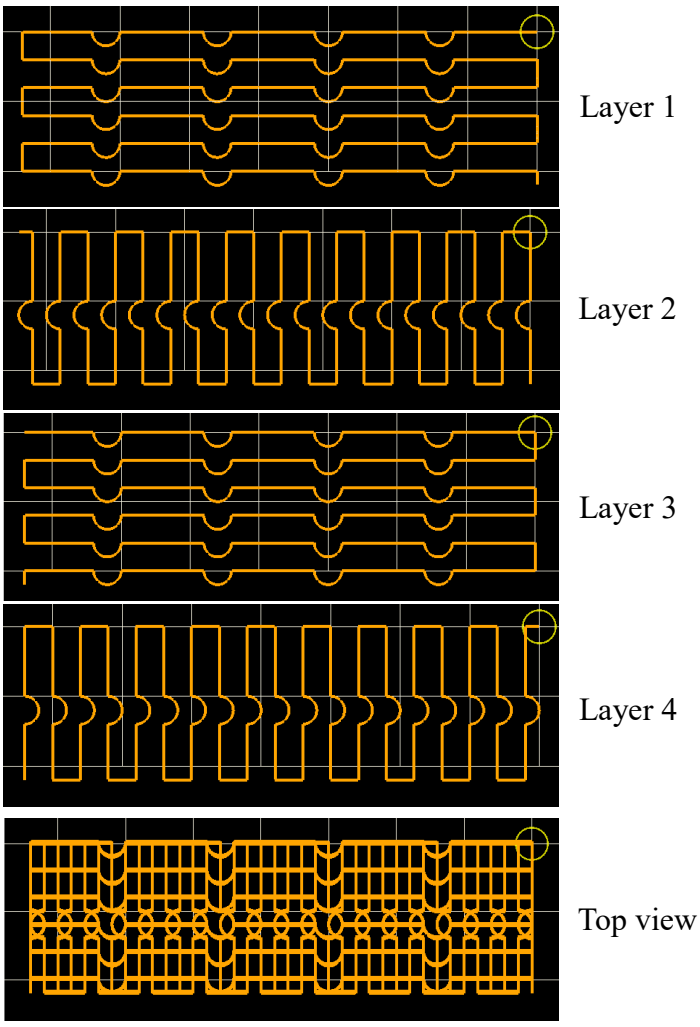

Figure 1. RoboCAD design of 13-93 glass scaffold with curved filaments.

Scaffolds of 13-93 glass ($6Na_2O$, $12K_2O$, 5MgO, 20CaO, $53SiO_2$, $4P_2O_5$, wt%) with grid-like (straight filament) structures were prepared using a robocasting method, as described in our previous studies [10, 26, 27]. The scaffolds with concave filaments were designed by RoboCAD (Figure 1) and fabricated using the robocasting method, as well.

Briefly, 13-93 glass was prepared by melting appropriate amounts of Na_2CO_3, K_2CO_3, $MgCO_3$, $CaCO_3$, SiO_2, and $NaH_2PO_4{\cdot}2H_2O$ in a platinum crucible at 1350 °C for 2 hours, and then quenching the melt between two cold stainless-steel plates. Glass particles with an average diameter of ~ 4 μm were obtained using an attrition mill and these particles were mixed with a 20 wt% aqueous Pluronic@F-127 solution to form a slurry (40 vol% glass particles). The slurry was then extruded in oil using a robocasting system (RoboCAD 3.0; 3-D Inks, Stillwater, OK) to form green-body, 3-D scaffolds. After printing, the scaffolds were dried at room temperature for 24 hours and then in an oven (~90 °C) at least overnight to remove any residual oil and water. The scaffolds were then heated at 0.5-2 °C /min in flowing oxygen to 600 °C for binder burnout and sintered in air at 700 °C for 1 hour to densify the glass filaments. The as-fabricated scaffolds were machined into thin discs (4.6 mm in diameter × 1.5 mm), washed twice with deionized water and twice with ethanol, dried in air, and then sterilized by heating in air for 12 hours at 250°C.

2.2. SURFACE MODIFICATION OF 13-93 GLASS SCAFFOLDS

Prior to the implantation, some of the as-fabricated scaffolds were reacted in an aqueous phosphate solution to produce a hydroxyapatite (HA)-like surface layer on the glass filaments, as described in previous studies [27, 31]. Briefly, the as-fabricated 13-93

glass scaffolds were immersed in 0.25 M K_2HPO_4 solution at 60 °C and pH = 12 (adjusted with 2 M NaOH solution) for 3 days. The ratio of mass of glass scaffolds to the volume of the phosphate solution was kept at 1g per 200 ml, and the solution was stirred gently every day. After the conversion, the scaffolds were rinsed with deionized water twice and with ethanol twice. The scaffolds were dried at 4 °C for at least 48 hours before implantation. The pre-treated scaffolds were sterilized by immersing them in anhydrous ethanol and then exposing them to ultraviolet light for 15 min, prior to implantation.

2.3. ANIMAL EXPERIMENTS

All animal use and care procedures were approved by the Missouri S&T Institutional Animal Care and Use Committee, in compliance with the NIH Guide for Care and Use of Laboratory Animals (1985). Four groups of scaffolds, described in Table 1, were implanted in rat calvarial defects for 6 weeks. The implantation time was selected based upon our previous study [27] which showed considerable bone regeneration for 13-93 glass scaffolds in the same animal model.

Table 1. 13-93 glass scaffolds used in this study.

Group	Structure	Pretreatment	Number of defects (n)
1	Straight	-	7
2	Curved	-	7
3	Straight	Surface-modified	7
4	Curved	Surface-modified	7

Male Sprague-Dawley rats (3 months old, weight ~ 350 g, Envigo, USA) were acclimated for 2 weeks to diet, water, and housing under a 12 h/12 h light/dark cycle. The rats were anesthetized with a combination of ketamine and xylazine (0.15 µl per 100 g). The rat was shaved from the bridge of the snout to the caudal end of the skull using electric clippers, the shaved area scrubbed with 70% ethanol and iodine, and a sterile drape was placed over the body. With a sterile scalpel, a ~1.5 cm incision was made down to the periosteum over the scalp from the nasal bone to the middle sagittal crest or bregma. The subcutaneous tissue, musculature, and periosteum were separated to expose the calvaria. Bilateral full thickness defects (4.6 mm in diameter) were created in the central area of each parietal bone using a saline-cooled trephine drill. The sites were constantly irrigated with sterile PBS to prevent overheating of the bone margins and to remove the bone debris. The dura mater was poked to bleed a little bit, and a scaffold, randomly selected from one of the four groups listed in Table 1, was implanted into each defect. The periosteum and skin were repositioned and closed with wound clips, and each animal then received an intramuscular injection of ~200 µl buprenorphine and ~200 µl penicillin post-surgery. All animals were monitored daily for the condition of the surgical wound, food intake, activity, and clinical signs of infection. After 6 weeks, the animals were sacrificed by CO_2 inhalation, and the calvarial defect sites with surrounding bone and soft tissue were harvested for subsequent evaluations.

2.4. HISTOLOGICAL PROCESSING

Harvested calvarial samples were fixed in a 10% formaldehyde solution for five days. The samples were cut into two halves after being washed with deionized water. One

half of each sample was used for paraffin embedding, and the other half was used for poly (methyl methacrylate) (PMMA) embedding. The paraffin-embedded samples were de-siliconized by immersing in 10% hydrofluoric acid for 2 hours, decalcified in 14 wt % ethylenediaminetetraacetic acid (EDTA, Sigma-Aldrich, USA) for 2 weeks, dehydrated in ethanol, and then embedded in paraffin using standard histological techniques. These samples were sectioned using a microtome. The thickness of the tissue section with paraffin was 5 μm. These slices were then stained with hematoxylin and eosin (H&E) [32] and Toluidine blue stain [33]. Without decalcification, the samples for PMMA embedding were dehydrated in ethanol and embedded in PMMA. These samples were sectioned, affixed to acrylic slices, and ground to a thickness down to 50 μm using a micro-grinding system (EXAKT 400CS, Norderstedt, Germany). The von Kossa stain was used to observe mineralization [34].

2.5. HISTOMORPHOMETRIC ANALYSIS

Histomorphometric analysis was carried out using optical images of stained sections and Fiji software (National Institutes of Health, USA). The percentage of new bone formed in a calvarial defect was evaluated from the H&E stained sections. The total defect area was measured from one edge of the old calvarial bone, including the entire scaffold and tissue within it, to the other edge of the old bone. The available pore area within the scaffold was determined by removing the area of the scaffold from the total defect area. The newly formed bone was identified by outlining the edge of the defect, with the presence of old and new bone being identified by lamellar and woven bone, respectively. The newly formed bone within this area was then outlined and measured;

the amount of the new bone was expressed as a percentage of the total defect area and the available pore area of the scaffolds.

The Von Kossa positive area in the calvarial defects implanted with the scaffolds was determined from the von Kossa stained sections. The mineralized bone and the HA layer formed during glass conversion both reacted with silver nitrate to turn black in color. These dark-stained areas in the defect images were outlined, measured by Fiji, and normalized to the total defect area. The positive area due to glass conversion was determined by subtracting the percentage of new bone in each sample from the percentage of von Kossa positive area in each sample.

2.6. CHARACTERIZATION OF 13-93 GLASS SCAFFOLDS

The scaffold porosity was determined using Archimedes method (ASTM C830). Briefly, the geometric volume of the scaffold (V_s) was computed by the dimensions measured by a Vernier caliper, while the volume of the glass content of the scaffold (V_g) was obtained by measuring the mass difference in air and in water. The porosity of the scaffold was derived from $(V_s-V_g)/V_s\times100$. Five as-fabricated scaffolds from each group were measured. The as-fabricated 13-93 glass scaffolds with different structures were examined by optical microscopy (KH-8700, Hirox-USA). The microstructures of the as-fabricated and surface-modified 13-93 glass scaffolds were observed using a scanning electron microscope (SEM; S4700 Hitachi, Tokyo, Japan) with an accelerating voltage of 15kV and a working distance of 12 mm. The curvature of the concave region of the curved filament was measured by Fiji with Kappa plugin; 20 curves were randomly selected and measured. The unstained sections of the implants in PMMA were coated

with carbon and characterized using the SEM operating in the backscattered electron mode.

2.7. STATISTICAL ANALYSIS

Measurements of the percentage of new bone (relative to the entire defect area) were expressed as a mean ± SD. Analysis of differences between groups was performed using one-way analysis of variance (ANOVA) followed by Tukey's post hoc test; the differences were considered significant at $p < 0.05$.

3. RESULTS

3.1. MICROSTRUCTURE OF 13-93 GLASS SCAFFOLDS

Optical images of the as-fabricated 13-93 glass scaffolds with straight and curved filaments are shown in Figure 2.

For both types of scaffolds, the diameter of the glass filaments was 155 ± 5 μm. The straight filament scaffolds had pores that were 117 ± 3 μm wide in the plane of deposition (xy plane) and 75 ± 5 μm wide in the direction perpendicular to the deposition plane (z direction) (Figure 3A and B), with an overall porosity of 41 ± 2 %. The scaffolds with curved filaments had pores that were 150 ± 5 μm wide in the plane of deposition (xy plane) and 70 ± 8 μm in the direction perpendicular to the deposition plane (z direction) (Figure 3C and D), with an overall porosity of 45 ± 3%. The depth of the concave elements in the curved filament scaffolds was 105 ± 5 μm (h, in Figure 3D). The radius of the concave elements was 0.375 ± 0.106 mm.

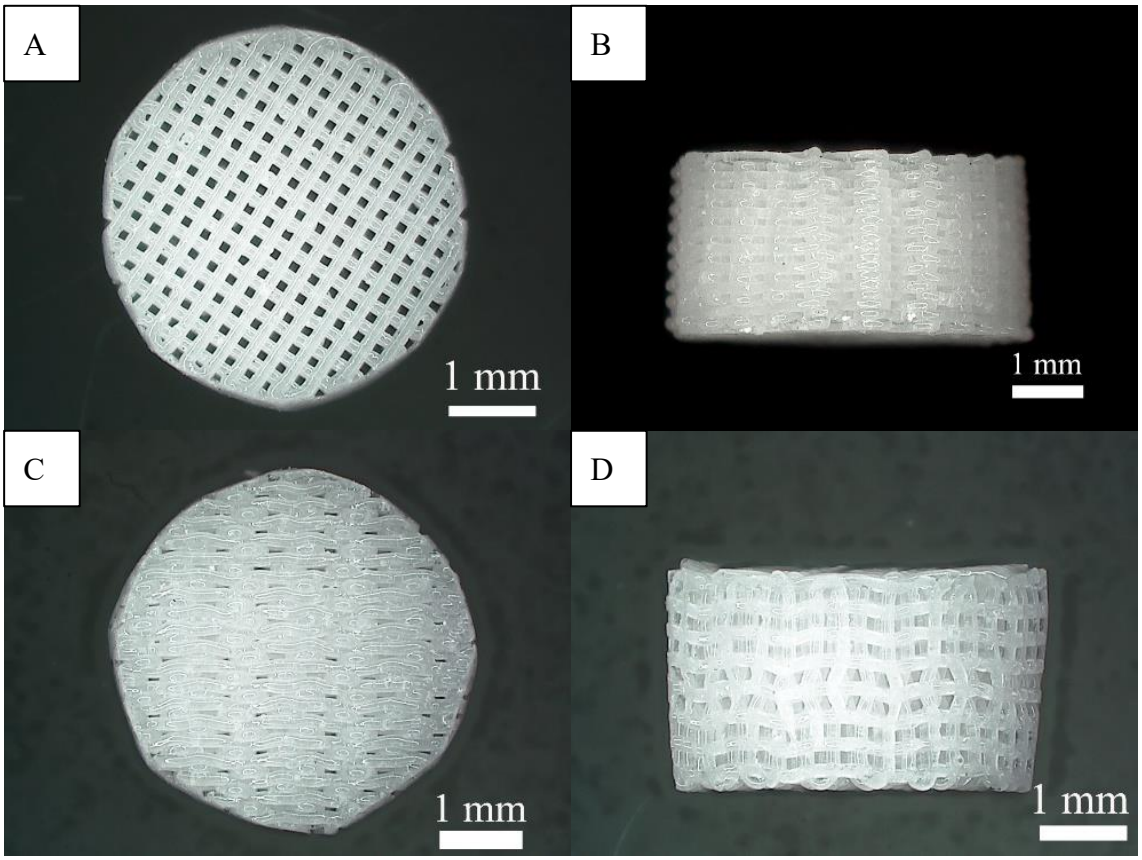

Figure 2. Optical images of 13-93 glass scaffolds ground into a disc shapes: A and B are a top-view and side view of the scaffold with straight filaments, respectively; C and D are a top-view and side-view of the scaffold with curved filaments, respectively.

For the scaffolds with straight filaments, the angles at the intersection of two filaments is obviously ~ 90º. For the scaffold with curved filaments, there were a variety of the angles at the intersection of two filaments. An example from the center part of an as-fabricated scaffold with curved filaments is shown in Figure 4. Angles at these intersections ranged from 40º to > 120º.

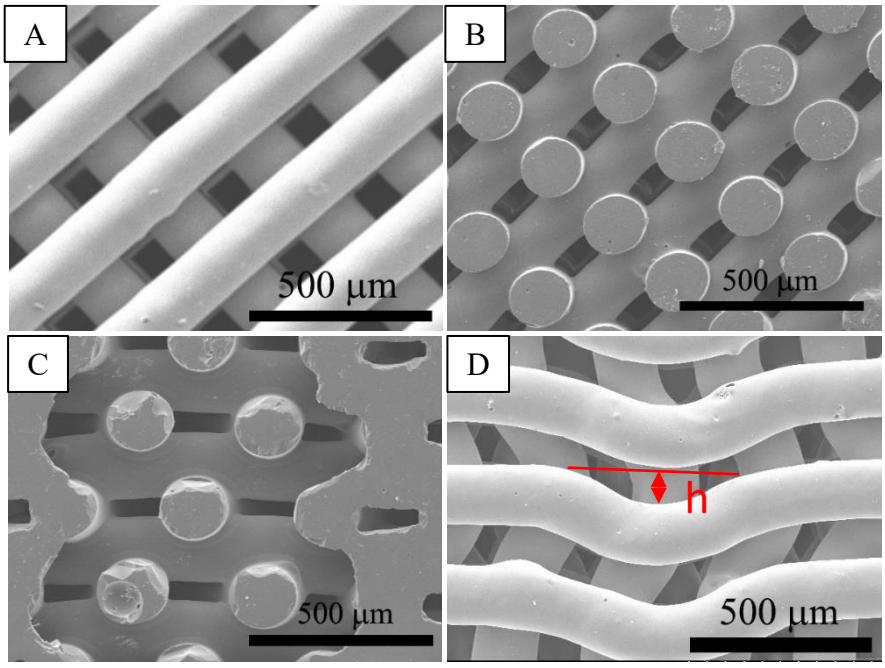

Figure 3. SEM images of as-fabricated 13-93 glass scaffolds with straight filaments (A) in the xy-plane, (B) in the z-direction; and with curved filaments (C) in the xy-plane, (D) in the z-direction. h indicates the depth of a concave element.

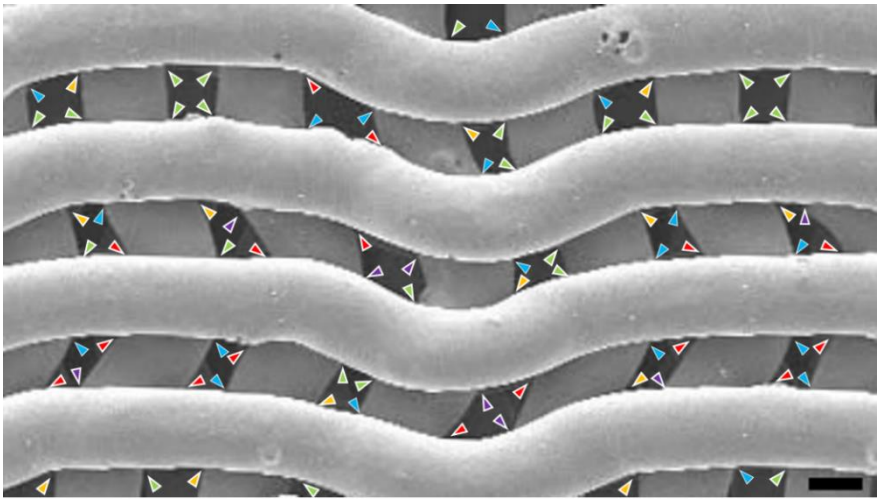

Figure 4. Angles at intersection of two filaments in the center part of the as-fabricated scaffold with curved filaments. Red arrows: 40º -60º. Orange arrows: 60º -80º. Green arrows: 80º -100º. Blue arrows: 100º -120º. Purple arrows: >120º. Scale bar = 100 µm.

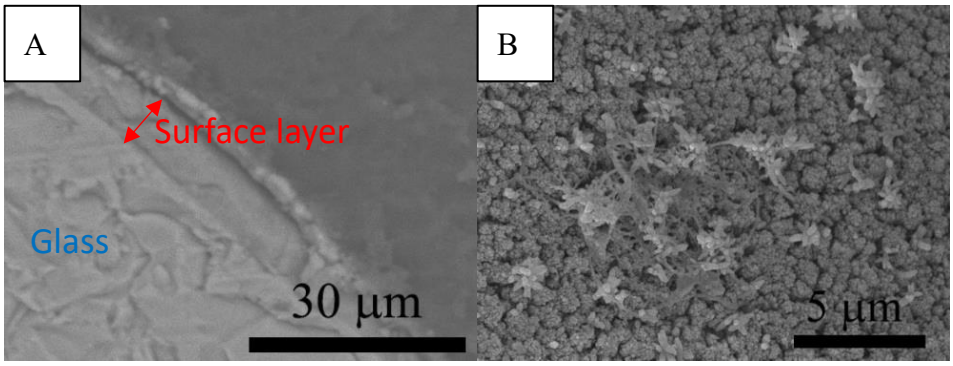

Figure 5. SEM images of surface-modified 13-93 glass scaffold: (A) cross-section of converted scaffold filament and (B) surface of converted glass filament.

Pre-treating scaffolds in a phosphate solution produced a thin (6 ± 1 µm) conversion layer on the surfaces of the glass filaments (Figure 5A), and these converted surfaces possessed both spherical nanoparticles and some needle-like nanoparticles (Figure 5B). These observations are consistent with previous studies of the formation of HA-like layers on the surfaces of 13-93 glass exposed to phosphate solutions [23, 24, 31, 35].

3.2. EVALUATION OF BONE REGENERATION IN RAT CALVARIAL DEFECTS

Representative examples of the H&E stained sections from the four sets of implants after six weeks in the rat calvarial defects are shown in Figure 6. New bone formation was observed mainly at the edges of the defects (adjacent to the host bone) and along the dura mater/bottom of the defects, where blood vessels could provide more nutrients to the site. The amount of new bone growth, expressed as percentage of total defect area and available pore space in the scaffold, was dependent on the microstructure and surface-condition of the 13-93 glass scaffold, as shown in Table 2.

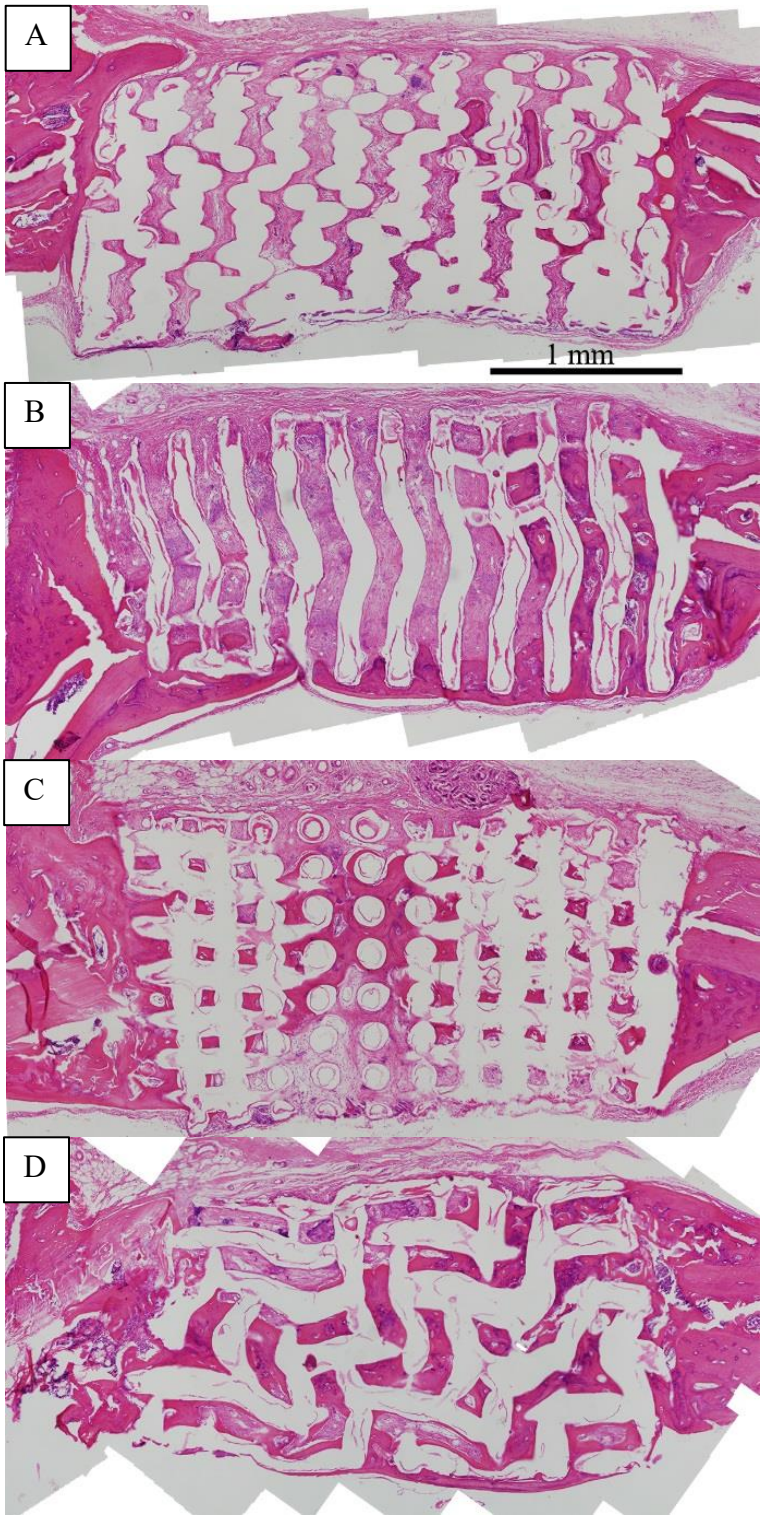

Figure 6. H&E stained sections of implants composed of as-fabricated 13-93 glass scaffold with straight (A1) or curved (B1) filaments, and surface-modified 13-93 glass scaffold with straight (C1) or curved (D1) filaments, from rat calvarial defects after 6 weeks. HB: host bone; NB: new bone; G: glass.

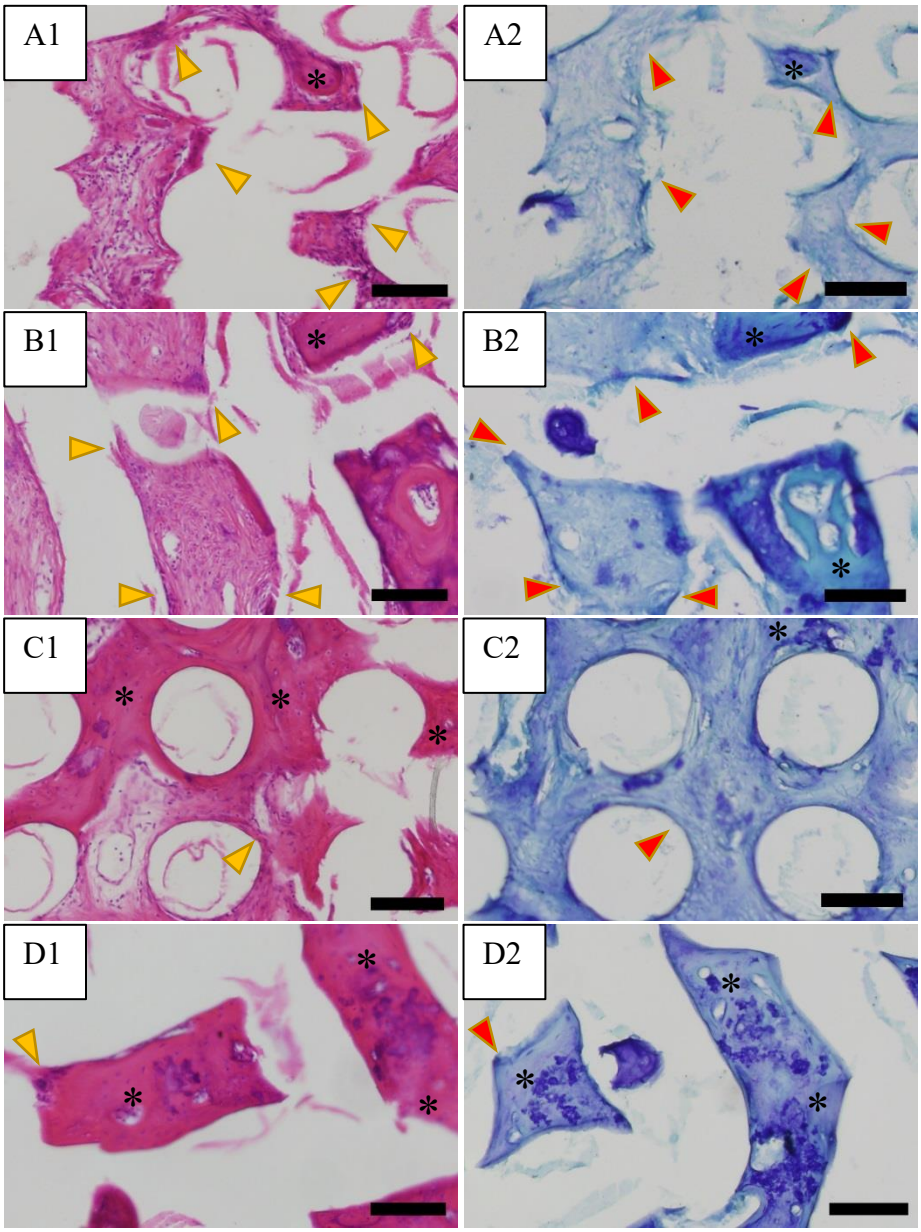

Figure 7. H&E stained (A1-D1) and Toluidine blue stained (B2-D2) sections from the center part of the implants: (A1, A2) as-fabricated scaffold with straight filaments; (B1, B2) as-fabricated scaffold with curved filaments; (C1, C2) surface-modified scaffold with straight filaments; (D1, D2) surface-modified scaffold with curved filaments;. * indicates new bone. Yellow arrows indicate the accumulation of cells in the concave regions of the curved filaments and at the intersection of two filaments. Red arrows are similar sites corresponding to the yellow arrows. Scale bar = 100 µm.

Table 2. Percent new bone formed and total von Kossa positive area in rat calverial defects implanted with the scaffolds at 6 weeks.

Group	New bone%		Von Kossa positive %
	Total area	Available area	Total area
1: straight	13 ± 3	25 ± 4	39 ± 4
2: curved	18 ± 4	30 ± 5	44 ± 4
3: pretreated straight	22 ± 6	40 ± 9	44 ± 5
4: pretreated curved	32 ± 8	56 ± 13	49 ± 6

H&E and Toluidine blue stained sections from the center parts of the implants for as-fabricated and surface-modified scaffolds are shown in Figure 7. For the as-fabricated scaffolds with straight filaments (Figure 7A1 and A2), accumulations of cells were found at the intersections of the filaments, and new bone appears to be growing from the intersections into the more open pore space. For the as-fabricated scaffold with curved filaments (Figure 7B1 and B2), accumulations of cells and bone growth were found at both filament intersections and in the concave regions of the filaments. For the surface-modified scaffold with straight filaments (Figure 7C1 and C2), more bone formation was observed than in the as-fabricated scaffolds, and the accumulations of cells and bone maturation and remodeling were found at the filament intersections. For the surface-modified scaffold with curved filaments (Figure 7D1 and D2), evidence for bone maturation and remodeling was observed in the scaffold pores, whereas newly formed bone was observed along the filament surfaces and in the concave regions of the curved filaments.

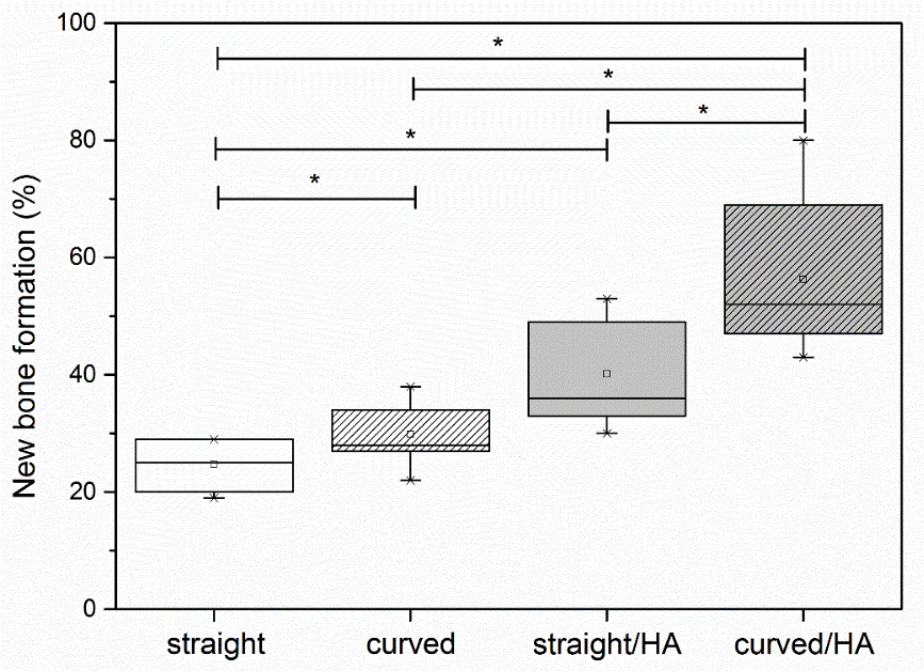

Figure 8. Comparative new bone formation in rat calvarial defects implanted with 13-93 glass scaffolds at 6 weeks: as-fabricated scaffold with straight filament; as-fabricated scaffolds with curved filaments; surface-modified scaffold with straight filaments; surface-modified scaffolds with curved filaments. The new bone formation is shown as a percent of available area in the scaffold. (Mean ± SD; n = 7, * significant difference between groups; $p < 0.05$).

For as-fabricated 13-93 glass scaffolds, the percentages of new bone formation in the total defect area was 13 ± 3% for straight-filament scaffolds (Group 1) and 18 ± 4% for curved-filament scaffolds (Group 2). When normalized to the available pore space in the scaffolds, the amounts of new bone formation were 25 ± 4% and 30 ± 5% for scaffolds in Group 1 and Group 2, respectively. There was a statistically significant improvement in bone regeneration in the scaffolds with curved filaments compared with the scaffolds with straight filaments ($n = 7$, $p < 0.05$, Figure 8).

For the surface-modified 13-93 glass scaffolds, values for new bone regeneration in the total defect areas were 22 ± 6% and 32 ± 8% for scaffolds with straight filaments

(Group 3) and curved filaments (Group 4), respectively. When normalized to the available pore space in the scaffolds, the percentages of new bone growth were 40 ± 9% and 56 ± 13% for Group 3 and Group 4, respectively. Again, for the surface-modified 13-93 glass scaffolds, scaffolds with curved filaments showed statistically more new bone formation than scaffolds with straight filaments ($n = 7$, $p < 0.05$, Figure 8).

For both the straight-filament and curved-filament designs, the pre-reacted scaffolds were more effective in promoting bone regeneration than the as-fabricated scaffolds ($n = 7$, $p< 0.05$, Figure 8).

3.3. EVALUATION OF MINERALIZATION OF 13-93 GLASS SCAFFOLDS

Representative examples of the Von Kossa stained sections of implants from the four sets of scaffolds are shown in Figure 9. A combination of mineralized bone and HA converted from the glass can be detected by von Kossa staining. The von Kossa positive areas (dark stain) are summarized in Table 2. The scaffolds with curved filaments showed significantly greater von Kossa positive areas than the scaffolds with straight filaments, for both as-fabricated and surface-modified scaffolds ($n = 7$, $p < 0.05$, Figure 10). For both the straight-filament and curved-filament designs, the pre-reacted scaffolds had significantly more von Kossa positive areas than the as-fabricated scaffolds ($n = 7$, $p< 0.05$, Figure 10).

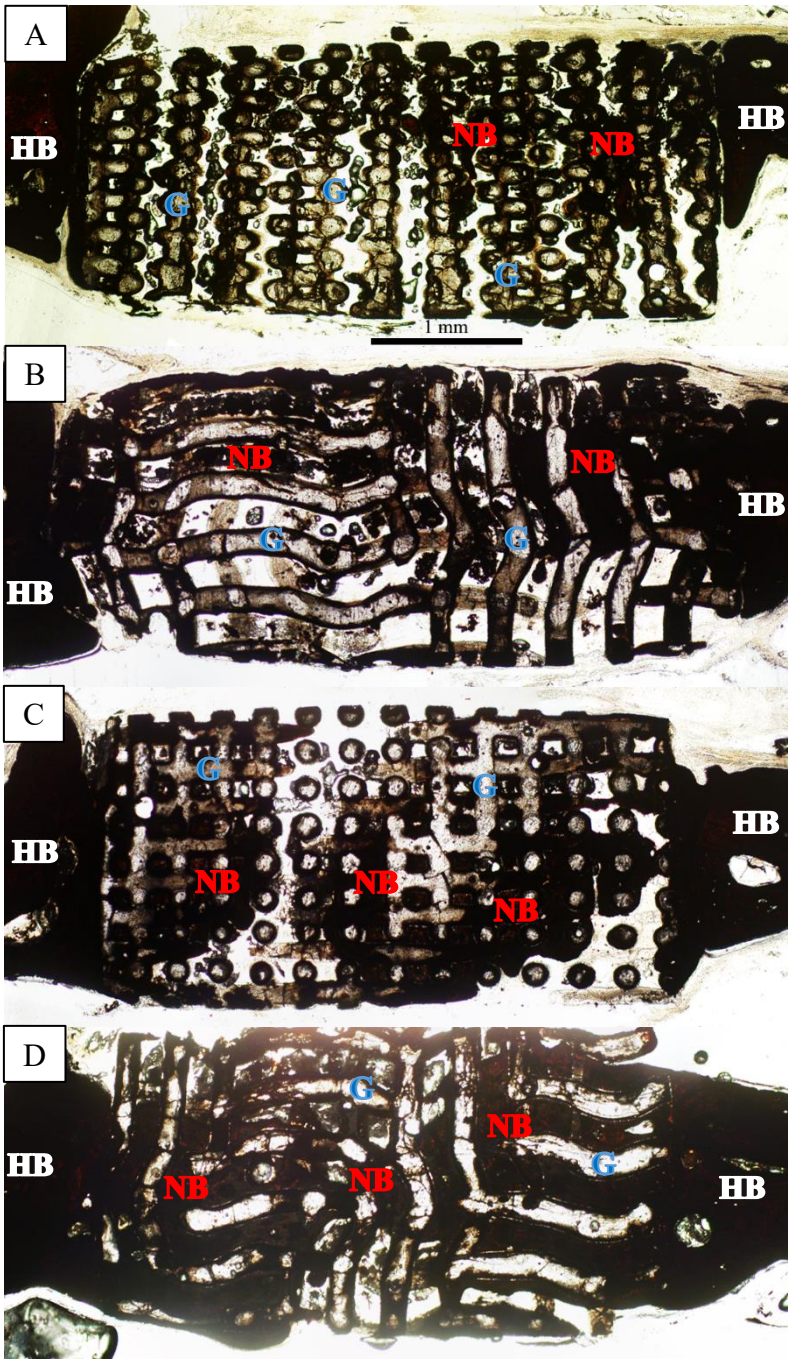

Figure 9. Von Kossa stained sections of implants composed of as-fabricated 13-93 glass scaffold with straight (A) or curved (B) filaments or surface-modified 13-93 glass scaffold with straight (C) or curved (D) filaments, from rat calvarial defect after 6 weeks. HB: host bone; NB: new bone; G: glass.

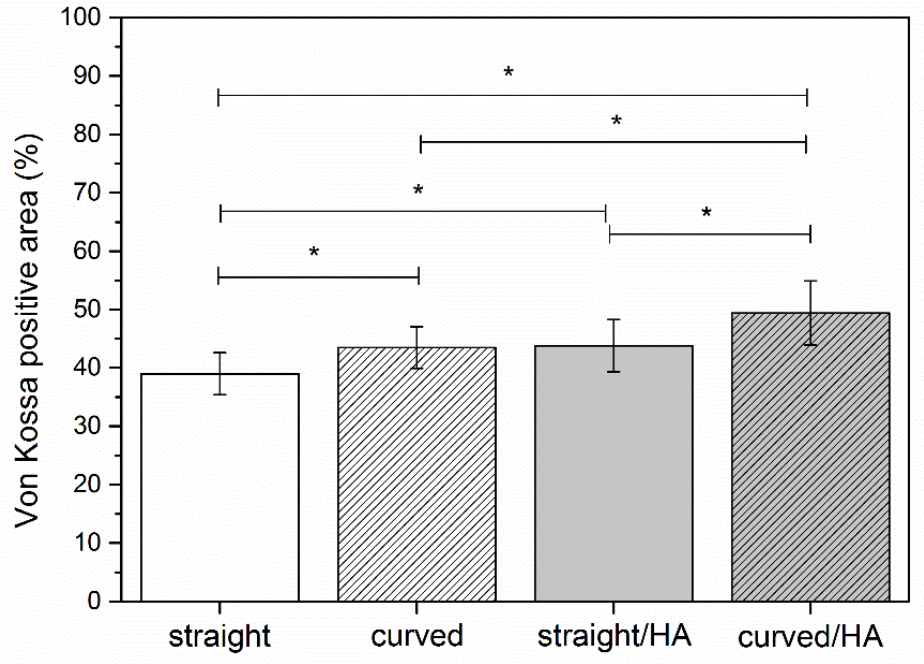

Figure 10. Comparative von Kossa positive areas for implants of 13-93 glass scaffolds in rat calvarial defects after 6 weeks: as-fabricated scaffolds with straight filaments; as-fabricated scaffolds with curved filaments; surface-modified scaffolds with straight filaments; surface-modified scaffolds with curved filaments. The von Kossa positive areas are shown as a percent of available area in the scaffold. (Mean ± SD; n = 7, * significant difference between groups; $p < 0.05$).

In order to evaluate the amount of von Kossa positive area that could be attributed to the formation of HA by the *in vivo* conversion of glass, the percent new bone determined from H&E staining (as a fraction of total available area) was subtracted from the percent von Kossa positive area. The von Kossa positive area due to HA formation by the *in vivo* conversion of the glass from Group 1 to Group 4 were 25 ± 5%, 25 ± 6%, 21 ± 3% and 19 ± 6%, respectively. There was no significant difference in the von Kossa positive area due to glass conversion among the four groups ($n = 7$, $p > 0.05$).

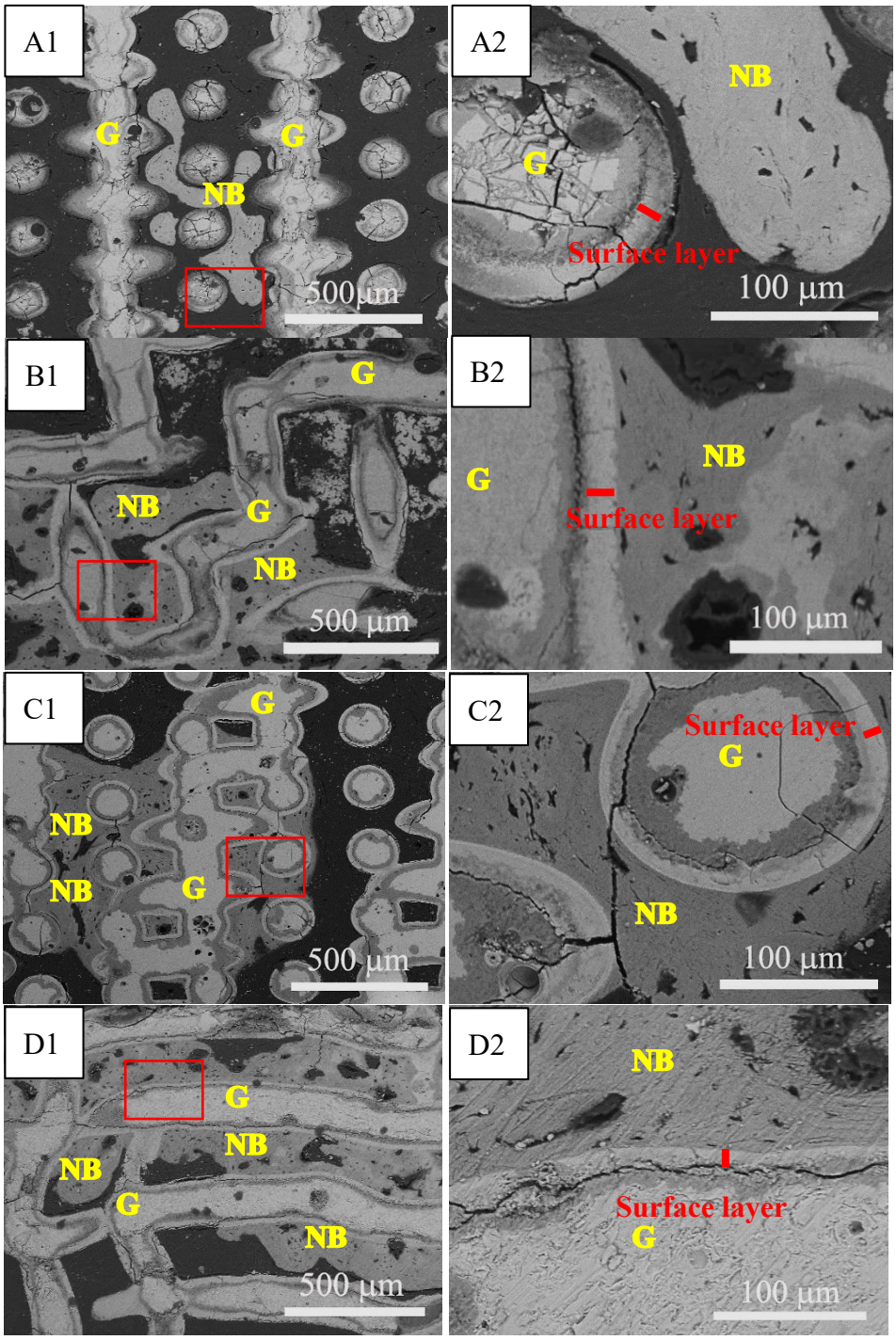

Figure 11. Backscatter SEM images of implants composed of as-fabricated 13-93 glass scaffolds with straight (A1) or curved (B1) filaments, or surface-modified 13-93 glass scaffold with straight (C1) or curved (D1) filaments, from rat calvarial defects after 6 weeks; (A2-D2) higher magnification images of boxed areas in (A1-D1). NB: new bone; G: glass.

Figure 11 shows backscatter SEM images of implants from the rat calvarial defects. The contrast in the grayscale images is an indication of differences in the calcium contents of the different areas including the glass scaffold, the converted surface layer, and the new bone [24, 30, 34]. Ca-rich areas are light gray, the silica-rich layer that forms on filaments in the early stage of glass conversion is dark gray, and lacunae and soft tissue regions are almost black. The glass filaments show three cross-sectional regions with different levels of grayscale: the inner-most region is unconverted glass, the middle region is the silica-rich layer, and the outermost region is the HA-like surface layer on the filament. For the as-fabricated scaffolds, the thickness of the HA-like surface layer in Group 1 (17 ± 2 μm) was similar to that in Group 2 (17 ± 1 μm). For the surface-modified scaffolds, the thicknesses of the surface layers in Group 3 and Group 4 were 8 ± 2 μm and 7 ± 2 μm, respectively, about one-half of the thicknesses of the layers that formed *in vivo* on the as-fabricated scaffolds.

4. DISCUSSION

The reactions that occur at the surfaces of bioactive silicate glasses implanted in osteo-defects have been described by Hench [36] and updated by Gerhardt et al. [37], and are summarized in Table 3. Stages 1-3 involve the exchange of alkali and alkaline earth ions from the glass with protonated water (H_3O^+) in the local environment to create a silica-rich surface layer. An amorphous Ca-phosphate layer forms on the surface of the silica-rich layer when Ca^{2+} ions released from the glass react with phosphate and

carbonate anions in the physiological environment, and this layer then crystallizes to form carbonated hydroxyapatite (HCA) (Stages 4-5). Cells then attach, proliferate, and differentiate on the HCA surface (Stages 6-9), to generate extracellular matrix, crystallize inorganic hydroxyapatite, and form new bone (Stages 10-12). The progress of these reactions is determined by the composition and architecture of the glass scaffolds.

Table 3. Sequence of interfacial reactions involved in forming a bond between bioactive glass and bone [36, 37].

Reaction events	Stages
Exchange of alkali ions with H_3O^+ ions from body fluids	1
Network dissolution and formation of silanol (SiOH) bonds	2
Silca-gel polymerization: SiOH + SiOH → Si-O-Si	3
Adsorption of amorphous Ca + PO_4 + CO_3	4
Crystallization of HCA layer	5
Biochemical adsorption of proteins (growth factors) on HCA layer	6
Macrophages remove debris from site allowing cells to occupy the space	7
Attachment of stem cells	8
Differentiation of stem cells to form osteoblasts	9
Generation of extracellular matrix	10
Crystallization of inorganic calcium phosphate	11
Proliferation and growth of bone	12

The *in vivo* experiments showed that the amount of bone regeneration after six weeks in rat calvarial defects depended on both the geometry of the 13-93 glass scaffold filaments, curved filaments were more effective than straight filaments, and the surface condition of the filaments where HA-converted filaments were more effective than the as-fabricated filaments (Figures 8 and 10). In addition, new bone formation appears to be enhanced at filament-filament intersections and in the concave regions of the curved filaments (Figure 7).

The influence of scaffold surface concavity on bone regeneration has been investigated in previous studies [38-43]. For example, the *in vitro* mineralization of calcium phosphate is enhanced in surface cavities (0.4 mm) compared to planar surfaces [38], and cell proliferation was enhanced on scaffolds with greater surface curvature [39]. Stem cells showed better maturation, osteo-differentiation, and specific protein production on a concave surface than a flat surface [40]. Both *in vitro* and *in vivo* studies [21, 28, 44, 45] have demonstrated that bone tissue growth is enhanced by surface curvature [28]. An *in vivo* test showed that concavities stimulated the formation of blood vessels which play an important role in bone regeneration [41]. Bone formation by intramembranous ossification was preferred on a concave surface [42], and concavity was shown to be conducive to the accumulation of growth factors, such as bone morphogenetic proteins (BMPs) [43]. Similar effects may contribute to the enhanced bone regeneration associated with the scaffolds formed from curved filaments compared to those with straight filaments, noted in the present study.

Further, the pore size and overall porosity of scaffolds are important parameters for bone regeneration [46]. The pore size and porosity influence cell adhesion,

proliferation and distribution by affecting the access to cell recruitment, vascularization, nutrients and oxygen. Interconnected porous structures with pore sizes at least 100 μm have been recommended for scaffolds to regenerate bone due to cell size, migration requirements, and transport, and pore sizes > 300 μm lead to enhancement of new bone formation and vascularization [46]. An *in vivo* test of dental implants coated with cancellous structured titanium showed that a slight increase in porosity (from 44% to 48%) could increase the rate of new bone growth [47]. In the present study, the pore sizes of our scaffolds limited by the diameter of glass filament and robocasting technique are larger than 100 μm. Moreover, the scaffold with curved filaments had slightly greater overall porosity (45 ± 3%) and pore dimensions (150 ± 5 μm × 70 ± 8 μm) than scaffolds with straight filaments (porosity = 41 ± 2 %, pore dimensions = 117 ± 3 μm × 75 ± 5 μm), and these differences might also contribute to the enhanced bone formation associated with the former structures.

After 6-weeks implantation, an HA-like layer formed on the surfaces of the filaments that constituted the structures of each scaffold, as observed by the SEM images for both as-fabricated and surface-modified samples (Fig, 11). 13-93 glass is a bioactive silicate glass that reacts *in vivo* to initially form a silica-rich layer (Stages 1-3), on which an HA-like surface layer forms (Stages 4-5) [3, 15, 24, 48, 49]. For surface-modified scaffolds, no silica-rich layer was observed after the pretreatment (Figure 4A) due to the high solubility of silica at pH=12 [50], whereas a silica-rich layer was apparent (Figure 12C1-2 and D1-2) after implantation *in vivo*. The thickness of the HA layer that formed *in vivo* on the as-fabricated scaffold was about twice that of the surface-modified scaffold. The thickness of the HA layer in surface-modified scaffold did not change

much, from about 6 μm to 7-8 μm, after 6 weeks implantation in the rat calvarial defect. The thin HA-like layer obtained by pretreatment in phosphate solution could reduce the glass conversion rate *in vivo* [27], if that layer hinders the penetration of body fluids to react with the unconverted glass, or if the pre-treatment alters the glass chemistry at the glass-HA interface.

The surface-modified scaffolds promoted greater levels of new bone formation compared to the as-fabricated scaffolds (Figure 8), consistent with a previous *in vivo* study of 13-93 glass scaffolds [27]. From that study, three points were raised. First, the HA layer on the surface of a glass scaffold obtained by pretreatment must interact with cells, tissues and some growth factors to promote bone formation [13, 23, 36, 51]. Second, when the as-fabricated scaffold initially reacts with the body fluid to form the silica-rich gel on the surface, this reaction could irreversibly denature proteins such as BMP-2 [13, 36, 51, 52]. Third, initial ion-exchange reactions at the glass surfaces increase the pH and osmolarity of the local physiological environment [48, 49, 53], and this could adversely affect cell viability and subsequent cellular and tissue interactions [54].

The *in vivo* results of the present work showed that the surface-modified scaffolds with curved filaments had a better capacity to facilitate new bone formation than scaffolds made with straight filaments, although differences in porosity and pore size between the two sets of scaffolds may also contribute to the enhanced bone regeneration. Pre-treating the scaffolds to produce a thin calcium phosphate layer on the glass surface improves the capability of the scaffold to support new bone formation. However, there are still some points that need to be investigated. For instance, the optimum fraction and

curvature of the concavities for bone regeneration are not known, nor is the optimum thickness of the pre-treatment layer.

5. CONCLUSIONS

The geometry and surface condition of the filaments that constitute 13-93 glass scaffolds affect the generation of new bone after six weeks in rat calvarial defects. Scaffolds constructed from curved filaments exhibited enhanced bone regeneration compared to scaffolds made with straight filaments. Pre-reacting the scaffolds to form calcium phosphate surface layers also increased the capacity to improve new bone formation.

ACKNOWLEDGMENT

Youqu Shen appreciates the financial support she received from the Missouri S&T Center for Biomedical Research (CBR) and the Lasko Endowment in the Materials Science and Engineering Department. We thank colleagues in the Missouri S&T Materials Research Center and Richard Watters from the CBR Animal Research Facility for technical assistance.

REFERENCES

[1] V. Campana, G. Milano, E. Pagano, M. Barba, C. Cicione, G. Salonna, W. Lattanzi, and G. Logroscino, *Bone substitutes in orthopaedic surgery: from basic science to clinical practice.* Journal of Materials Science: Materials in Medicine, 2014. **25**(10): p. 2445-2461.

[2] F. Deschaseaux, L. Sensébé, and D. Heymann, *Mechanisms of bone repair and regeneration.* Trends in Molecular Medicine, 2009. **15**(9): p. 417-429.

[3] M.N. Rahaman, D.E. Day, B.S. Bal, Q. Fu, S.B. Jung, L.F. Bonewald, and A.P. Tomsia, *Bioactive glass in tissue engineering.* Acta biomaterialia, 2011. **7**(6): p. 2355-2373.

[4] A.A. El-Rashidy, J.A. Roether, L. Harhaus, U. Kneser, and A.R. Boccaccini, *Regenerating bone with bioactive glass scaffolds: A review of in vivo studies in bone defect models.* Acta Biomaterialia, 2017. **62**: p. 1-28.

[5] L. Polo-Corrales, M. Latorre-Esteves, and J.E. Ramirez-Vick, *Scaffold design for bone regeneration.* Journal of nanoscience and nanotechnology, 2014. **14**(1): p. 15-56.

[6] M.N. Rahaman, W. Xiao, and W. Huang, *bioactive glass implants for potential application in structural bone repair.* Biomedical Glasses, 2017. **3**(1): p. 56-66.

[7] L. Bi, M.N. Rahaman, D.E. Day, Z. Brown, C. Samujh, X. Liu, A. Mohammadkhah, V. Dusevich, J.D. Eick, and L.F. Bonewald, *Effect of bioactive borate glass microstructure on bone regeneration, angiogenesis, and hydroxyapatite conversion in a rat calvarial defect model.* Acta Biomaterialia, 2013. **9**(8): p. 8015-8026.

[8] J. Samira, M. Saoudi, K. Abdelmajid, O. Hassane, R. Treq, E. Hafed, E. Abdelfatteh, and K. Hassib, *Accelerated bone ingrowth by local delivery of Zinc from bioactive glass: oxidative stress status, mechanical property, and microarchitectural characterization in an ovariectomized rat model.* Libyan Journal of Medicine, 2015. **10**(1): p. 28572-28572.

[9] V. Aina, A. Perardi, L. Bergandi, G. Malavasi, L. Menabue, C. Morterra, and D. Ghigo, *Cytotoxicity of zinc-containing bioactive glasses in contact with human osteoblasts.* Chemico-Biological Interactions, 2007. **167**(3): p. 207-218.

[10] Y. Lin, W. Xiao, B.S. Bal, and M.N. Rahaman, *Effect of copper-doped silicate 13–93 bioactive glass scaffolds on the response of MC3T3-E1 cells in vitro and on bone regeneration and angiogenesis in rat calvarial defects in vivo.* Materials Science & Engineering C, 2016. **67**: p. 440-452.

[11] H. Wang, S. Zhao, J. Zhou, Y. Shen, W. Huang, C. Zhang, M.N. Rahaman, and D. Wang, *Evaluation of borate bioactive glass scaffolds as a controlled delivery system for copper ions in stimulating osteogenesis and angiogenesis in bone healing.* Journal of Materials Chemistry B, 2014. **2**(48): p. 8547-8557.

[12] C. Zhang, J. Zhang, S. Zhao, M. Zhu, Y. Zhu, Y. Huang, and C. Tao, *Three-dimensional printing of strontium-containing mesoporous bioactive glass scaffolds for bone regeneration.* Acta Biomaterialia, 2014. **10**(5): p. 2269-2281.

[13] L.L. Hench, *The story of Bioglass®.* Journal of Materials Science: Materials in Medicine, 2006. **17**(11): p. 967-978.

[14] L.L. Hench, R.J. Splinter, W. Allen, and T. Greenlee, *Bonding mechanisms at the interface of ceramic prosthetic materials.* Journal of biomedical materials research, 1971. **5**(6): p. 117-141.

[15] M. Brink, *Bioactive glasses with a large working range*. 1997: Åbo Akademi University, Department of Chemical Engineering.

[16] M. Brink, *The influence of alkali and alkaline earths on the working range for bioactive glasses.* Journal of Biomedical Materials Research: An Official Journal of The Society for Biomaterials and The Japanese Society for Biomaterials, 1997. **36**(1): p. 109-117.

[17] M. Brink, T. Turunen, R.P. Happonen, and A. Yli‐Urpo, *Compositional dependence of bioactivity of glasses in the system Na_2O‐K_2O‐MgO‐CaO‐B_2O_3-P_2O_5-SiO_2.* Journal of Biomedical Materials Research: An Official Journal of The Society for Biomaterials and The Japanese Society for Biomaterials, 1997. **37**(1): p. 114-121.

[18] S. Giannitelli, D. Accoto, M. Trombetta, and A. Rainer, *Current trends in the design of scaffolds for computer-aided tissue engineering.* Acta biomaterialia, 2014. **10**(2): p. 580-594.

[19] S.-I. Roohani-Esfahani, P. Newman, and H. Zreiqat, *Design and Fabrication of 3D printed Scaffolds with a Mechanical Strength Comparable to Cortical Bone to Repair Large Bone Defects.* Scientific Reports, 2016. **6**(1): p. 19468.

[20] J.M. Sobral, S.G. Caridade, R.A. Sousa, J.F. Mano, and R.L. Reis, *Three-dimensional plotted scaffolds with controlled pore size gradients: Effect of scaffold geometry on mechanical performance and cell seeding efficiency.* Acta Biomaterialia, 2011. **7**(3): p. 1009-1018.

[21] M. Paris, A. Götz, I. Hettrich, C.M. Bidan, J.W.C. Dunlop, H. Razi, I. Zizak, D.W. Hutmacher, P. Fratzl, G.N. Duda, W. Wagermaier, and A. Cipitria, *Scaffold curvature-mediated novel biomineralization process originates a continuous soft tissue-to-bone interface.* Acta Biomaterialia, 2017. **60**: p. 64-80.

[22] W. Xiao, M.A. Zaeem, B.S. Bal, and M.N. Rahaman, *Creation of bioactive glass (13–93) scaffolds for structural bone repair using a combined finite element modeling and rapid prototyping approach.* Materials Science & Engineering C, 2016. **68**: p. 651-662.

[23] Q. Fu, M.N. Rahaman, B. Sonny Bal, R.F. Brown, and D.E. Day, *Mechanical and in vitro performance of 13–93 bioactive glass scaffolds prepared by a polymer foam replication technique.* Acta Biomaterialia, 2008. **4**(6): p. 1854-1864.

[24] X. Liu, M.N. Rahaman, and Q. Fu, *Bone regeneration in strong porous bioactive glass (13-93) scaffolds with an oriented microstructure implanted in rat calvarial defects.* Acta Biomaterialia, 2013. **9**(1): p. 4889-4898.

[25] X. Liu, M.N. Rahaman, Q. Fu, and A.P. Tomsia, *Porous and strong bioactive glass (13-93) scaffolds prepared by unidirectional freezing of camphene-based suspensions.* Acta biomaterialia, 2012. **8**(1): p. 415-423.

[26] X. Liu, M.N. Rahaman, G.E. Hilmas, and B.S. Bal, *Mechanical properties of bioactive glass (13-93) scaffolds fabricated by robotic deposition for structural bone repair.* Acta Biomaterialia, 2013. **9**(6): p. 7025-7034.

[27] X. Liu, M.N. Rahaman, Y. Liu, B.S. Bal, and L.F. Bonewald, *Enhanced bone regeneration in rat calvarial defects implanted with surface-modified and BMP-loaded bioactive glass (13-93) scaffolds.* Acta biomaterialia, 2013. **9**(7): p. 7506-7517.

[28] M. Rumpler, A. Woesz, J.W.C. Dunlop, T.v.D. Joost, and P. Fratzl, *The effect of geometry on three-dimensional tissue growth.* Journal of The Royal Society Interface, 2008. **5**(27): p. 1173-1180.

[29] M.N. Rahaman, W. Xiao, Y. Liu, and B. Sonny Bal. *Osteoconductive and Osteoinductive Implants Composed of Hollow Hydroxyapatite Microspheres*. in *Advances in Bioceramics and Porous Ceramics VII: A Collection of Papers Presented at the 38th International Conference on Advanced Ceramics and Composites January 27-31, 2014 Daytona Beach, Florida*. 2015. John Wiley & Sons, Inc.

[30] Y. Shen, M. Rahaman, Y. Liu, and Y.-W. Huang, *Evaluation of open hollow CDHA microspheres on bone regeneration in rat calvarial defects.*

[31] Y. Lin, W. Xiao, X. Liu, B.S. Bal, L.F. Bonewald, and M.N. Rahaman, *Long-term bone regeneration, mineralization and angiogenesis in rat calvarial defects implanted with strong porous bioactive glass (13–93) scaffolds.* Journal of Non-Crystalline Solids, 2016. **432**: p. 120-129.

[32] J.Q. Feng, J. Zhang, S.L. Dallas, Y. Lu, S. Chen, X. Tan, M. Owen, S.E. Harris, and M. Macdougall, *Dentin matrix protein 1, a target molecule for Cbfa1 in bone, is a unique bone marker gene.* Journal of Bone and Mineral Research, 2002. **17**(10): p. 1822-1831.

[33] G. Sridharan and A.A. Shankar, *Toluidine blue: A review of its chemistry and clinical utility.* Journal of Oral and Maxillofacial Pathology, 2012. **16**(2): p. 251-255.

[34] L. Bonewald, S. Harris, J. Rosser, M. Dallas, S. Dallas, N. Camacho, B. Boyan, and A. Boskey, *von Kossa staining alone is not sufficient to confirm that mineralization in vitro represents bone formation.* Calcified tissue international, 2003. **72**(5): p. 537-547.

[35] X. Liu, M.N. Rahaman, Y. Liu, B.S. Bal, and L.F. Bonewald, *Enhanced bone regeneration in rat calvarial defects implanted with surface-modified and BMP-loaded bioactive glass (13-93) scaffolds.* Acta Biomaterialia, 2013. **9**(7): p. 7506-17.

[36] L.L. Hench, *Bioceramics.* Journal of the American Ceramic Society, 1998. **81**(7): p. 1705-1727.

[37] L.-C. Gerhardt and A.R. Boccaccini, *Bioactive glass and glass-ceramic scaffolds for bone tissue engineering.* Materials, 2010. **3**(7): p. 3867-3910.

[38] M. Bianchi, E.R.U. Edreira, J.G. Wolke, Z.T. Birgani, P. Habibovic, J.A. Jansen, A. Tampieri, M. Marcacci, S.C. Leeuwenburgh, and J.J. Van Den Beucken, *Substrate geometry directs the in vitro mineralization of calcium phosphate ceramics.* Acta biomaterialia, 2014. **10**(2): p. 661-669.

[39] K.C.R. Kolan, A. Thomas, M.C. Leu, and G. Hilmas, *In vitro assessment of laser sintered bioactive glass scaffolds with different pore geometries.* Rapid Prototyping Journal, 2015. **21**(2): p. 152-158.

[40] A. Graziano, R. d'Aquino, M.G. Cusella-De Angelis, G. Laino, A. Piattelli, M. Pacifici, A. de Rosa, and G. Papaccio, *Concave Pit-Containing Scaffold Surfaces Improve Stem Cell-Derived Osteoblast Performance and Lead to Significant Bone Tissue Formation.* PLoS ONE, 2007. **2**(6): p. e496.

[41] A. Scarano, V. Perrotti, L. Artese, M. Degidi, D. Degidi, A. Piattelli, and G. Iezzi, *Blood vessels are concentrated within the implant surface concavities: a histologic study in rabbit tibia.* Odontology, 2014. **102**(2): p. 259-266.

[42] M.J. Coathup, K.A. Hing, S. Samizadeh, O. Chan, Y.S. Fang, C. Campion, T. Buckland, and G.W. Blunn, *Effect of increased strut porosity of calcium phosphate bone graft substitute biomaterials on osteoinduction.* Journal of Biomedical Materials Research Part A, 2012. **100**(6): p. 1550-1555.

[43] U.R. Ripamonti, *Functionalized surface geometries induce:" Bone: formation by autoinduction".* Frontiers in physiology, 2017. **8**: p. 1084.

[44] C.M. Bidan, K.P. Kommareddy, M. Rumpler, P. Kollmannsberger, Y.J.M. Bréchet, P. Fratzl, and J.W.C. Dunlop, *How linear tension converts to curvature: Geometric control of bone tissue growth.* PLoS ONE, 2012. **7**(5): p. e36336.

[45] M.A. Alias and P.R. Buenzli, *Modeling the Effect of Curvature on the Collective Behavior of Cells Growing New Tissue.* Biophysical Journal, 2017. **112**(1): p. 193-204.

[46] V. Karageorgiou and D. Kaplan, *Porosity of 3D biomaterial scaffolds and osteogenesis.* Biomaterials, 2005. **26**(27): p. 5474-5491.

[47] B.J. Story, W.R. Wagner, D.M. Gaisser, S.D. Cook, and A.M. Rust-Dawicki, *In vivo performance of a modified CSTi dental implant coating.* International Journal of Oral & Maxillofacial Implants, 1998. **13**(6).

[48] W. Huang, D.E. Day, K. Kittiratanapiboon, and M.N. Rahaman, *Kinetics and mechanisms of the conversion of silicate (45S5), borate, and borosilicate glasses to hydroxyapatite in dilute phosphate solutions.* Journal of Materials Science: Materials in Medicine, 2006. **17**(7): p. 583-596.

[49] A. Yao, D. Wang, W. Huang, Q. Fu, M.N. Rahaman, and D.E. Day, *In vitro bioactive characteristics of borate-based glasses with controllable degradation behavior.* Journal of the American Ceramic Society, 2007. **90**(1): p. 303-306.

[50] B.C. Bunker, *Molecular mechanisms for corrosion of silica and silicate glasses.* Journal of Non-Crystalline Solids, 1994. **179**: p. 300-308.

[51] H. Fu, M.N. Rahaman, D.E. Day, and R.F. Brown, *Hollow hydroxyapatite microspheres as a device for controlled delivery of proteins.* Journal of Materials Science: Materials in Medicine, 2011. **22**(3): p. 579-591.

[52] R.A. Messing, *Insoluble papain prepared by adsorption on porous glass.* Enzymologia, 1970. **38**(1): p. 39-42.

[53] Q. Fu, M.N. Rahaman, H. Fu, and X. Liu, *Silicate, borosilicate, and borate bioactive glass scaffolds with controllable degradation rate for bone tissue engineering applications. I. Preparation and in vitro degradation.* Journal of Biomedical Materials Research Part A, 2010. **95A**(1): p. 164-171.

[54] J.P. Mather and P.E. Roberts, *Introduction to cell and tissue culture: theory and technique*. 1998: Springer Science & Business Media.

SECTION

3. CONCLUSION

3.1. SUMMARY

1) Open CDHA microspheres, produced by sectioning closed microspheres, promote greater new bone formation after six weeks and twelve weeks in rat calvarial defects then do the closed microspheres.
2) Open CDHA microspheres with smaller radii (53-75 μm) promote greater new bone formation than open HA microspheres with larger radii (106-125 μm).
3) Open and closed CDHA microspheres loaded with the same amount of BMP-2 (0.25 μg per defect) promoted similar levels of new bone formation after six 6-weeks implantation in rat calvarial defects.
4) Hollow BCP microspheres were produced by the heat-treatment of CDHA microspheres obtained by glass conversion technique. The composition and microstructure of the microspheres was affected by the concentration and pH value of the phosphate solution used in the glass conversion process.
5) Two sets of CDHA microspheres (Ca/P ≈ 1.55 and 1.59) and the corresponding BCP microspheres (β-TCP/HA =70/30 and 44/56) were selected for further *in vitro* tests. The BCP microspheres with 70 wt% β-TCP showed faster reaction rates in acetic acid (pH=5) and simulated body fluid.
6) Two sets of CDHA microspheres (Ca/P ≈ 1.55 and 1.59) and the corresponding BCP microspheres (β-TCP/HA =70/30 and 44/56) were implanted in both calvarial

and subcutaneous sites in rats. The BCP microspheres with 70 wt% β-TCP showed faster *in vivo* degradation rates, and the best ability to promote new bone formation in the calvarial defects, and to promote blood vessel formation in the subcutaneous defects, compared to the other groups of microspheres.

7) The ability to tailor the composition, nano-structure, and meso-structure of these microspheres by controlling the processing conditions to convert the soluble Ca-containing borate glasses in phosphate solutions means that materials can be designed for specific biomedical applications that utilize the macro-porosity of the hollow microspheres, the nano-porosity of the shell walls, and the enhanced bio-activity of the BCP phases.

8) The geometry and surface condition of the filaments that constitute 13-93 glass scaffolds affect the generation of new bone after six weeks in rat calvarial defects. Scaffolds constructed from curved filaments exhibited enhanced new bone formation compared to scaffolds made with straight filaments. Pre-reacting the scaffolds to form calcium phosphate surface layers also increased the capacity to promote new bone formation.

3.2. RECOMMENDATIONS FOR FUTURE WORK

3.2.1. The Effect of Open CDHA Microspheres on Bone Regeneration. Open CDHA microspheres can enhance bone formation compared to closed CDHA microspheres, and smaller open microspheres showed enhanced new bone formation compared with larger open microspheres. The mechanism for this enhancement is not known and needs to be studied. The optimum open sphere radius has not been

determined; open spheres with radii smaller than 53 microns and larger than 125 microns should be studied to determine if there is a reproducible trend in microsphere radius on bone formation. The enhanced bone formation associated with BCP particles compared to CDHA particles indicates that open BCP microspheres with large β-TCP contents could be most effective for enhancing new bone formation.

3.2.2. Determine the Optimal Size of Open CDHA Microspheres and Dosage of BMP-2 for Bone Regeneration. We do not know how BMP-2 is incorporated into the closed or open CDHA microspheres, whether it is only absorbed on the surfaces of the particles or in the nanoporosity of the particles. The optimal BMP-2 dosage has not been determined, nor have the release rates (pharmakinetics) from the particles. This information must be acquired before treatments with BMP-2-loaded CDHA microspheres can be considered beyond these preliminary results.

3.2.3. Evaluation of BCP Microspheres in Bone Regeneration. The compositions and microstructures of BCP particles are affected by the conditions of glass conversion and heat-treatment. The optimal design of BCP microspheres can be determined with more *in vitro* and *in vivo* experiments. The osteoinductivity of BCPs have been reported in other studies, but our BCP microspheres in current study did not show osteoinductivity in rat subcutaneous defects at up to 12 weeks. The osteoinductivity of BCP microspheres with modified compositions needs future investigation. The potential of BCP microspheres for protein delivery can be evaluated by loading some proteins, such as BSA, BMP-2, and then measuring release rates in standard solutions.

3.2.4. 13-93 Glass Scaffolds with Curved Filaments for Bone Regeneration. The *in vivo* results of the present work showed that the surface-modified scaffolds with

curved filaments had a better capacity to facilitate new bone formation than scaffolds made with straight filaments. The optimum fraction and curvature of the concavities for bone regeneration is not known, nor is the optimum thickness of the pre-treatment layer. The scaffolds with larger fraction and curvature of curved filaments need to be fabricated for further *in vivo* tests. The effect of the fraction and curvature on the mechanical properties of the scaffolds also deserve further investigation by evaluating the compressive strengths and tensile strengths.

APPENDIX A.

BONE REGENERATION FACILATED BY OPEN CDHA MICROSPEHRES LOADED WITH LOW DOSES OF BMP-2

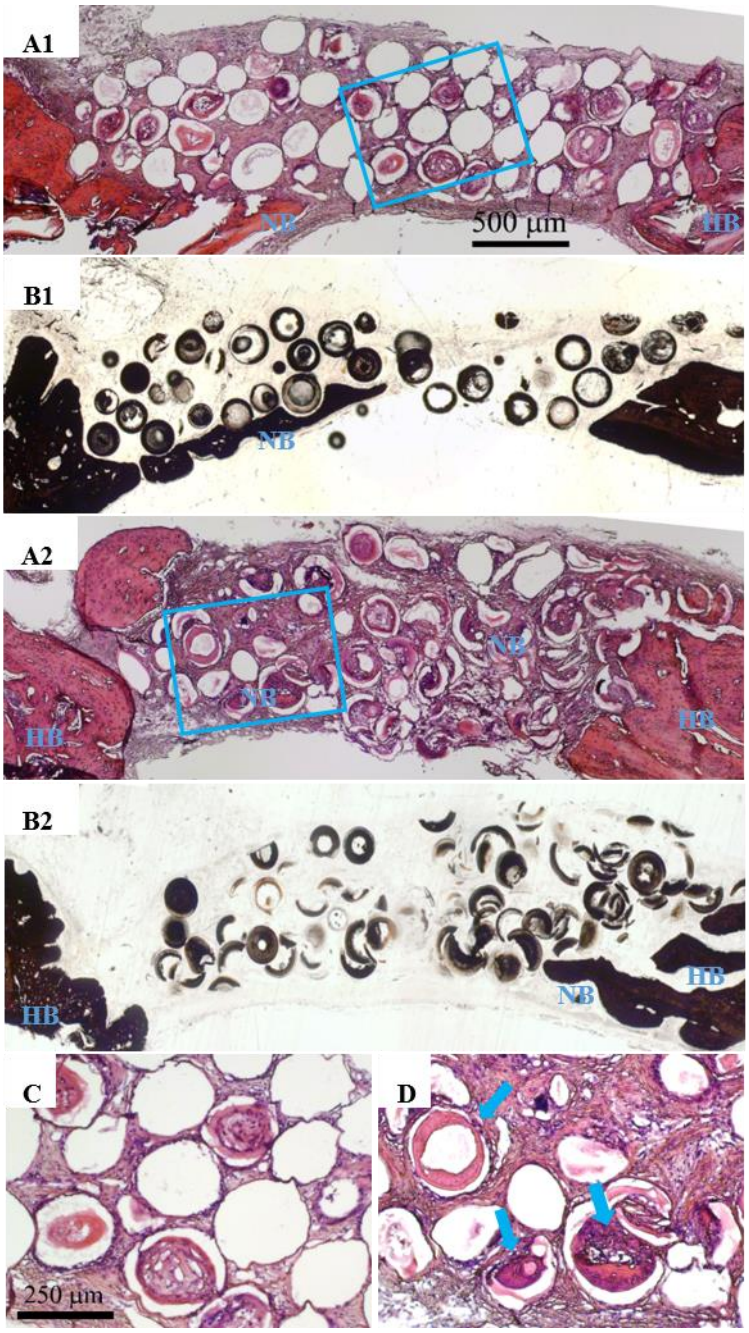

Figure A.1. H&E and von Kossa stained sections of implants composed of closed (A1, B1) and open (A2, B2) CDHA microspheres without BMP-2 after 6 weeks in rat calvarial defects; (C, D) higher-magnification images of boxed area in (A1, A2). HB: host bone; NB: new bone. Blue arrow: new bone growth in micro-concavity.

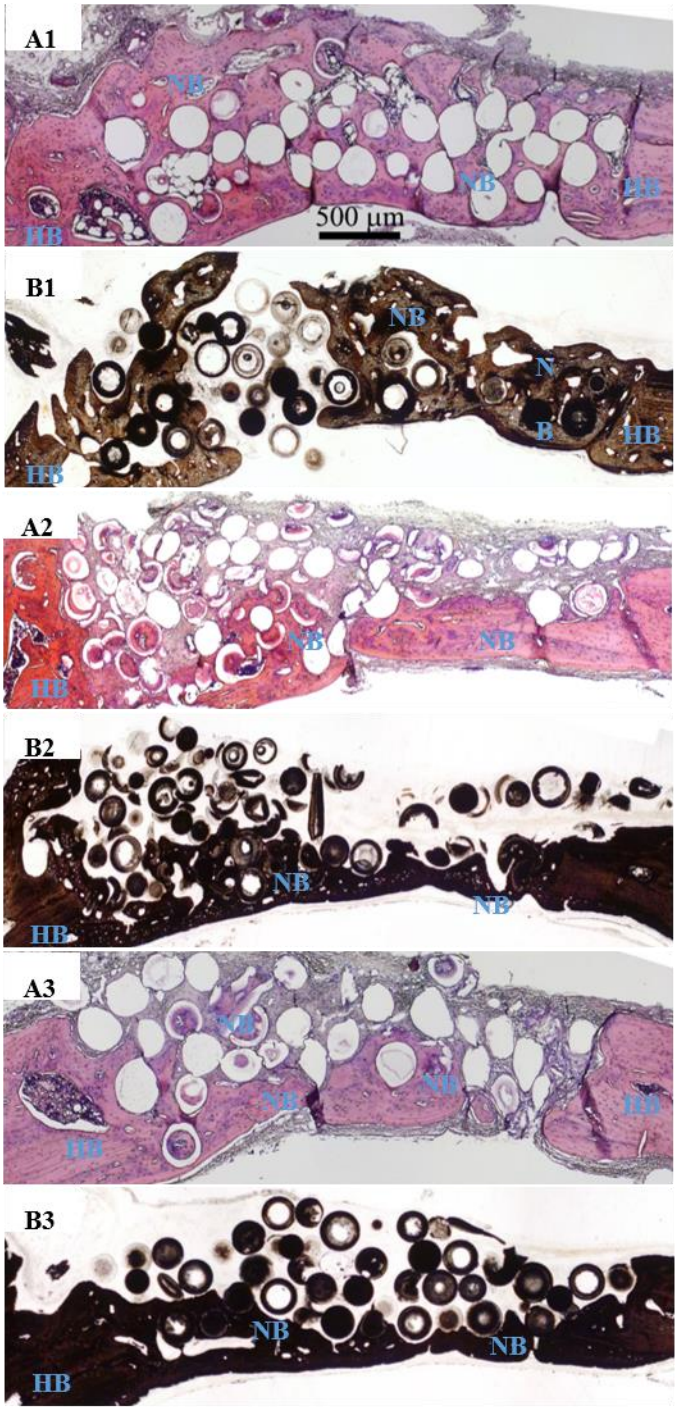

Figure A.2. H&E stained and von Kossa sections of implants composed of closed and open hollow CDHA microspheres with BMP-2 after 6 weeks in rat calvarial defects: closed HA microspheres with 1 μg BMP-2 (A1, B1); open CDHA microspheres with 0.25 μg BMP-2 (A2, B2); closed CDHA microspheres with 0.25 μg BMP-2 (A3, B3). HB: host bone; NB: new bone.

Table A.1. Comparative new bone formation and von Kossa positive area in all implants after 6 weeks in rat calvarial defects; the amount of new bone is expressed as a percent of the total defect area (mean ± SD).

Hollow CDHA microspheres	New bone (%)	Positive area (%)
Closed	6 ± 2	30 ± 3
Open	12 ± 3	35 ± 3
Closed + 1 μg BMP-2	40 ± 6	69 ± 5
Closed + 0.25 μg BMP-2	26 ± 9	55 ± 8
Open + 0.25 μg BMP-2	24 ± 8	49 ± 7

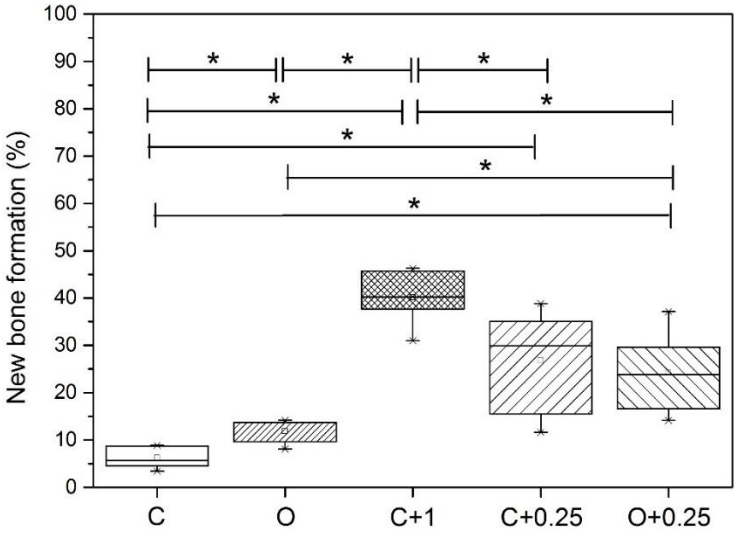

Figure A.3. Comparative new bone formation in all implants after 6 weeks in rat calvarial defects. (Mean ± SD; n = 5~10, * significant difference between groups; $p < 0.05$). Closed CDHA microspheres denoted as “C”, open HA microspheres denoted as “O”, and closed CDHA microspheres loaded with 1 μg BMP-2/defect are control groups. All BMP2 concentration are μg/defect.

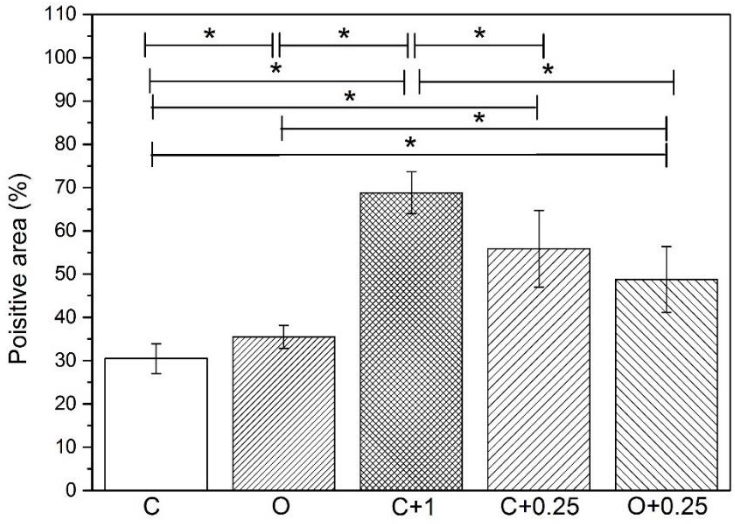

Figure A.4. Comparative von Kossa positive area for all implants after 6 weeks in rat calvarial defects. (Mean ± SD; n = 5~10, * significant difference between groups; $p < 0.05$). Closed CDHA microspheres denoted as "C", open CDHA microspheres denoted as "O", and closed CDHA microspheres loaded with 1 µg BMP-2/defect are control groups. All BMP2 concentration are µg/defect.

APPENDIX B.

HOLLOW BIPHASIC CALCIUM PHOSPHATE MICROSPHERES FROM GLASS DISSOLUTION AND REPRECIPITATION

Table B.1. The particle sizes in the external surface and the diameter ratios of hollow core (d) to the microsphere size (D) of the microspheres produced in different conditions.

Microspheres			d/D	Particle size (nm)
pH	K_2HPO_4 solution (M)	Heat-treatment		
7	0.25	-	0.374 ± 0.011	133 ± 13
7	0.25	800°C/5h	0.353 ± 0.013	530 ± 90
9	0.25	-	0.370 ± 0.005	114 ± 10
9	0.25	800°C/5h	0.351 ± 0.017	570 ± 113
12	0.25	-	0.371 ± 0.006	90 ± 13
12	0.25	800°C/5h	0.363 ± 0.011	770 ± 294
7	0.1	-	0.543 ± 0.007	113 ± 16
7	0.1	800°C/5h	0.536 ± 0.011	365 ±130
9	0.1	-	0.546 ± 0.009	86 ± 10
9	0.1	800°C/5h	0.532 ± 0.012	576 ± 244
12	0.1	-	0.534 ± 0.013	84 ± 22
12	0.1	800°C/5h	0.518 ± 0.016	748 ± 253

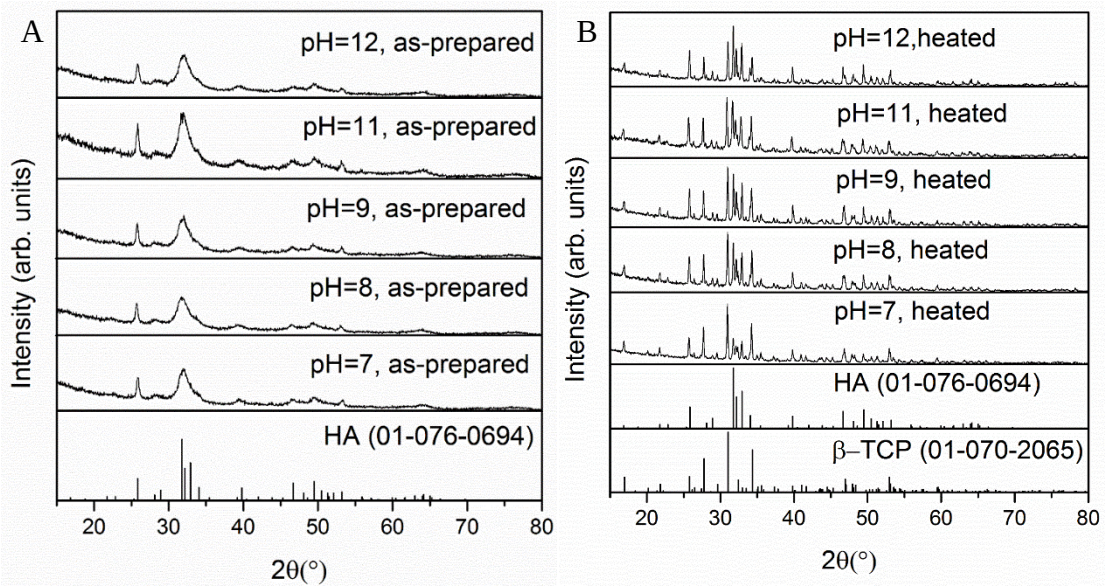

Figure B.1. XRD patterns of the as-prepared (A) and heat-treated (B) microspheres produced in 0.1 M K_2HPO_4 solution at various pH values.

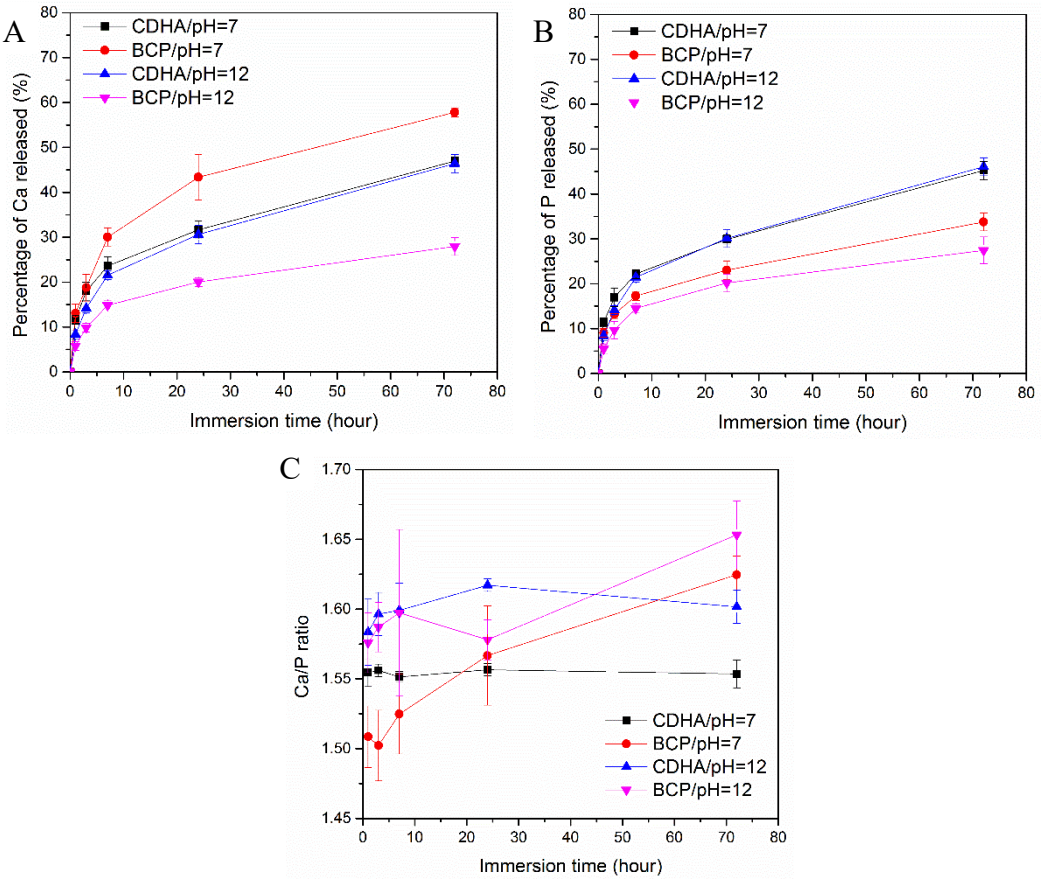

Figure B.2. Percentage of calcium (A) and phosphate (B) ions released from the microspheres in KAc solution. (C) The Ca/P ion ratios released to the KAc solutions a function of immersion time.

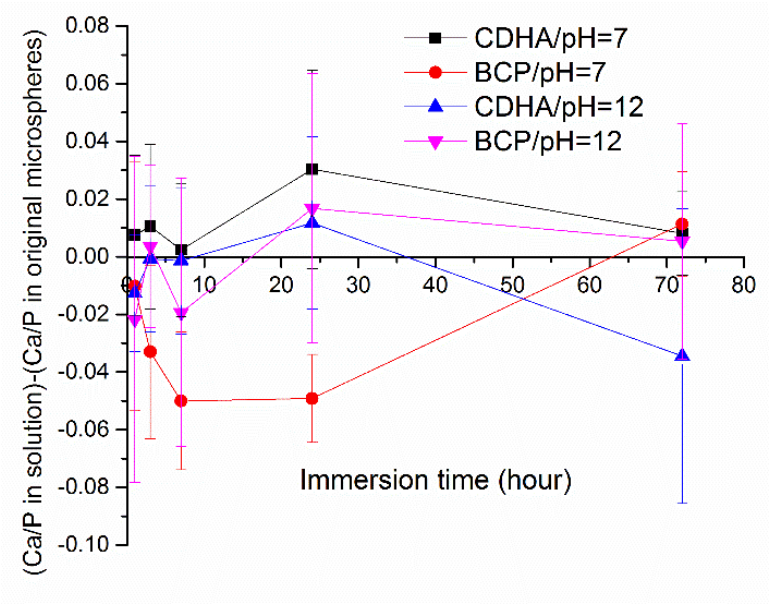

Figure B.3. Changes of the Ca/P ion ratios released to the KAc solutions during immersion time.

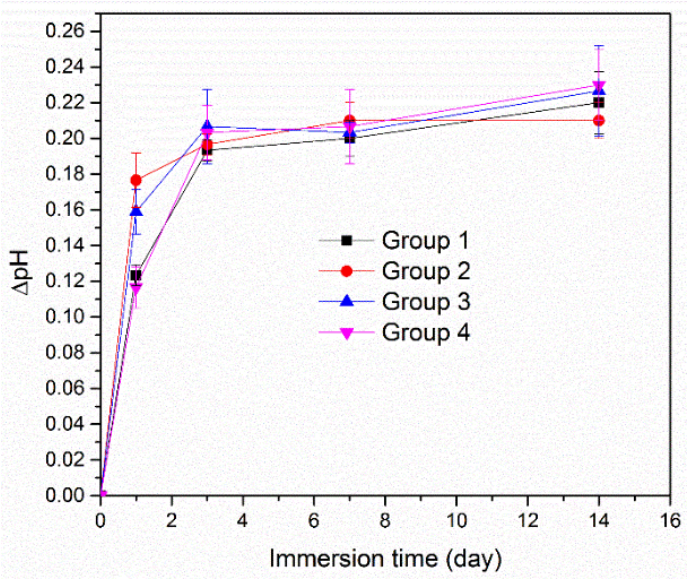

Figure B.4. Changes of pH value of the SBF solution after adding the microspheres during two-weeks immersion at 37°C.

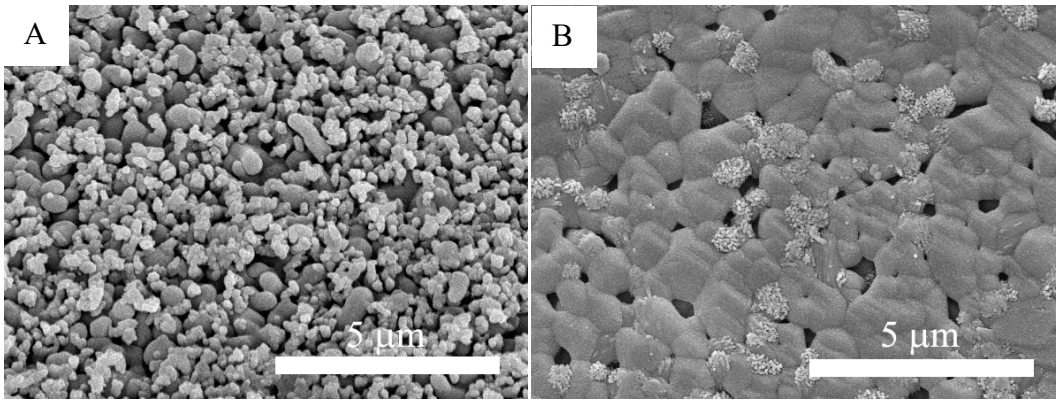

Figure B.5. SEM images of the external surfaces of the BCP microspheres: (A) BCP/pH=7 and (B) BCP/pH=12 after two-weeks of immersion of SBF solution at 37°C.

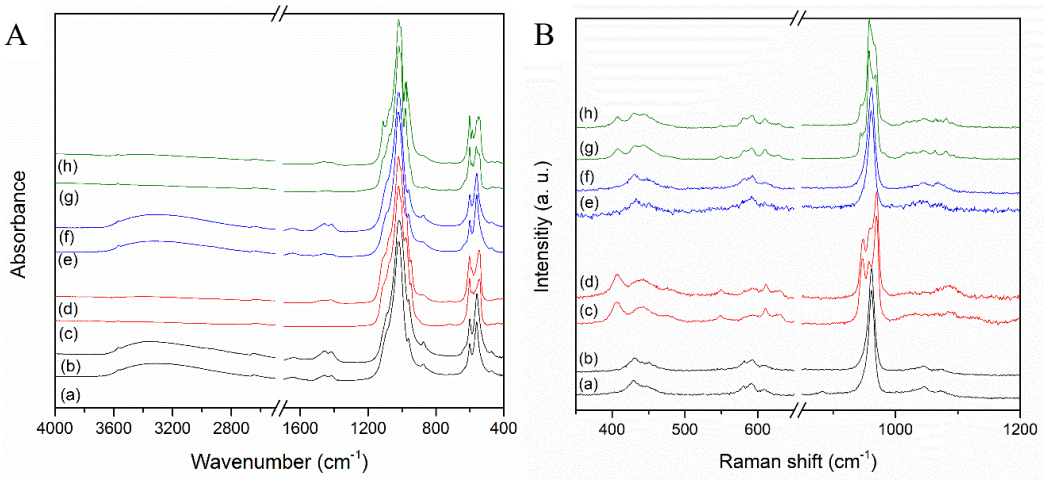

Figure B.6. FTIR (A) and Raman (B) spectra of the microspheres before and after immersion in SBF solution for 14 days. CDHA/pH=7: (a) before and (b) after; BCP/pH=7: (c) before and (d) after; CDHA/pH=12: (e) before and (f) after; BCP/pH=12: (g) before and (h) after.

Table B.2. Vibration modes observed in FTIR spectra of the microspheres before and after SBF solution.

Vibration mode	CDHA/pH=7		BCP/pH=7		CDHA/pH=12		BCP/pH=12	
	Before	After	Before	After	Before	After	Before	After
ν_1PO_4 (symmetric stretching)	962	962	946 974	947 974	962	962	949 963 980	962 980
ν_2PO_4 (deformation)	470	470	470	470	470	470	472	471
ν_3PO_4 (asymmetric stretching)	1022 1090	1017 1090	1021	1020	1019	1013	1007 1019 1073 1112	1004 1017 1073 1096 1110
ν_4PO_4 (deformation)	560 600	570 600	543 600	544 603	601 560	560 601	562 587 602	550 586 602
HPO_4	875	875	-	878	875	873	-	875
OH (symmetric stretching)	3570	3570	3570	3570	3570	3570	3570	3570
H_2O	3200-3600	3200-3600	-	3200-3600	3200-3600	3200-3600	-	3200-3600
$\nu_1\ CO_3^{2-}$ (symmetric stretching)	1457 1420	1456 1417	-	1455 1417	1456 1417	1457 1416	-	1457 1417

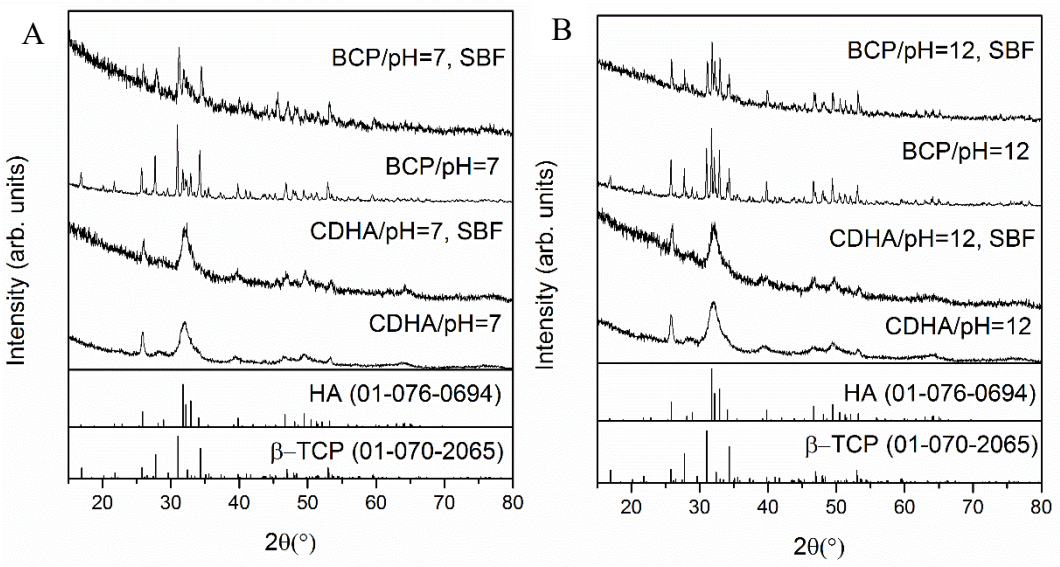

Figure B.7. XRD patterns of the CDHA and BCP microspheres produced at pH=7 (A) and pH=12 (B) before and after immersion in SBF solution for 14 days.

APPENDIX C.

13-93 GLASS SCAFFOLDS WITH CURVED FILAMENTS

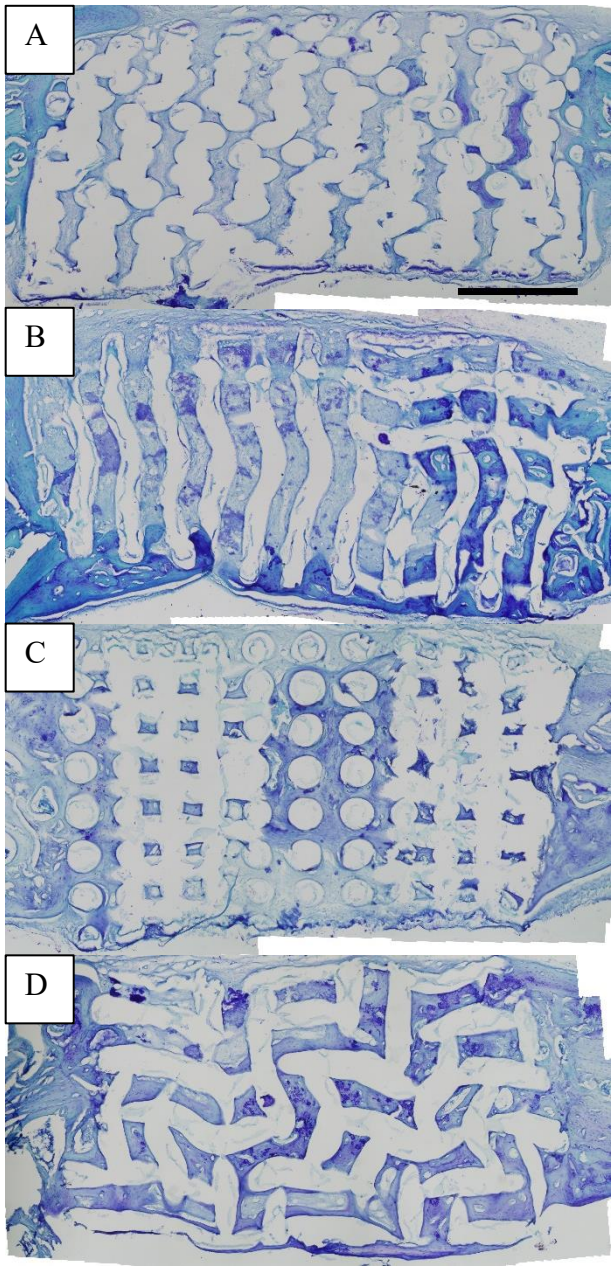

Figure C.1. Toluidine blue stained sections of implants composed of as-fabricated 13-93 glass scaffolds with straight (A) or curved (B) filaments or surface-modified 13-93 glass scaffolds with straight (C) or curved (D) filaments, from rat calvarial defect after 6 weeks.

Table C.1. Thickness of silica-rich layers measured from SEM images of implanted scaffolds (20 measurements).

Group	Thickness of silica-rich layer
1	16 ± 4
2	19 ± 6
3	20 ± 7
4	18 ± 5

Table C.2. Ca/P atomic ratios in regions of the converted layer, the Si-rich layer, and unconverted glass from Von Kossa stained samples, assuming Ca^{2+} is replaced by $2Ag^{+}$.

Group	Converted layer	Si-rich layer	Unconverted glass
1	1.59 ± 0.10	3.04 ± 0.35	5.68 ± 1.76
2	1.63 ± 0.20	3.16 ± 0.41	5.79 ± 0.71
3	1.55 ± 0.18	2.63 ± 0.31	5.48 ± 1.64
4	1.56 ± 0.09	2.75 ± 0.36	5.65 ± 1.12

BIBLIOGRAPHY

[1] V. Campana, G. Milano, E. Pagano, M. Barba, C. Cicione, G. Salonna, W. Lattanzi, and G. Logroscino, *Bone substitutes in orthopaedic surgery: from basic science to clinical practice.* Journal of Materials Science: Materials in Medicine, 2014. **25**(10): p. 2445-2461.

[2] F. Deschaseaux, L. Sensébé, and D. Heymann, *Mechanisms of bone repair and regeneration.* Trends in Molecular Medicine, 2009. **15**(9): p. 417-429.

[3] F. Loi, L.A. Córdova, J. Pajarinen, T.-h. Lin, Z. Yao, and S.B. Goodman, *Inflammation, fracture and bone repair.* Bone, 2015. **86**: p. 119-130.

[4] I.H. Kalfas, *Principles of bone healing.* Neurosurg Focus, 2001. **10**(4): p. E1.

[5] P. Pivonka and C.R. Dunstan, *Role of mathematical modeling in bone fracture healing.* BoneKEy reports, 2012. **1**: p. 221.

[6] A. Scarano, M. Degidi, G. Iezzi, G. Pecora, M. Piattelli, G. Orsini, S. Caputi, V. Perrotti, C. Mangano, and A. Piattelli, *Maxillary sinus augmentation with different biomaterials: a comparative histologic and histomorphometric study in man.* Implant dentistry, 2006. **15**(2): p. 197-207.

[7] L. Trombelli, *Which reconstructive procedures are effective for treating the periodontal intraosseous defect?* Periodontology 2000, 2005. **37**(1): p. 88-105.

[8] R.T. Kao, G. Conte, D. Nishimine, and S. Dault, *Tissue engineering for periodontal regeneration.* Journal of the California Dental Association, 2005. **33**(3): p. 205-215.

[9] N. Pandit, R. Malik, and D. Philips, *Tissue engineering: a new vista in periodontal regeneration.* Journal of Indian Society of Periodontology, 2011. **15**(4): p. 328.

[10] C. Dahlin and A. Johansson, *Iliac Crest Autogenous Bone Graft versus Alloplastic Graft and Guided Bone Regeneration in the Reconstruction of Atrophic Maxillae: A 5-Year Retrospective Study on Cost-Effectiveness and Clinical Outcome.* Clinical implant dentistry and related research, 2011. **13**(4): p. 305-310.

[11] P.V. Giannoudis, H. Dinopoulos, and E. Tsiridis, *Bone substitutes: an update.* Injury, 2005. **36**(3): p. S20-S27.

[12] J.A. McAuliffe, *Bone graft substitutes.* Journal of Hand Therapy, 2003. **16**(2): p. 180-187.

[13] O. Reikerås, H. Shegarfi, C. Naper, F.P. Reinholt, and B. Rolstad, *Impact of MHC mismatch and freezing on bone graft incorporation: an experimental study in rats.* Journal of Orthopaedic Research, 2008. **26**(7): p. 925-931.

[14] W. Wang and K.W.K. Yeung, *Bone grafts and biomaterials substitutes for bone defect repair: A review.* Bioactive Materials, 2017. **2**(4): p. 224-247.

[15] L.L. Hench and L.L. Hench, *Bioceramics: From Concept to Clinic.* Journal of the American Ceramic Society, 1991. **74**(7): p. 1487-1510.

[16] M.N. Richard, *Bioactive behavior of a borate glass*. Masters Theses, Missouri University of Science and Technology, 2000.

[17] K.P. Fears, *Formation of hollow hydroxyapatite microspheres*. Masters Theses, Missouri University of Science and Technology, 2001.

[18] X. Han and D.E. Day, *Reaction of sodium calcium borate glasses to form hydroxyapatite.* Journal of Materials Science: Materials in Medicine, 2007. **18**(9): p. 1837-1847.

[19] Y. Yu, Z. Bacsik, M. Edén, u. Stockholms, f. Naturvetenskapliga, and m. Institutionen för material- och, *Contrasting in vitro apatite growth from bioactive glass surfaces with that of spontaneous precipitation.* Materials, 2018. **11**(9): p. 1690.

[20] H. Fu, M.N. Rahaman, and D.E. Day, *Effect of process variables on the microstructure of hollow hydroxyapatite microspheres prepared by a glass conversion method.* Journal of the American Ceramic Society, 2010. **93**(10): p. 3116-3123.

[21] L.C. Chow, *Solubility of calcium phosphates.* Monographs in oral science, 2001. **18**: p. 94-111.

[22] S.V. Dorozhkin, *Calcium orthophosphates (CaPO4): occurrence and properties.* Progress in Biomaterials, 2016. **5**(1): p. 9-70.

[23] Y. Liu, X. Sheng, Y. Dong, and Y. Ma, *Removal of high-concentration phosphate by calcite: Effect of sulfate and pH.* Desalination, 2012. **289**: p. 66-71.

[24] N.N. Vanderspiegel, *Reaction of potassium calcium borate glasses to form apatite and dicalcium phosphate dihydrate*. Masters Theses, Missouri University of Science and Technology 2004.

[25] F. Bakan, *A Systematic Study of the Effect of pH on the Initialization of Ca-deficient Hydroxyapatite to β-TCP Nanoparticles.* Materials (Basel, Switzerland), 2019. **12**(3): p. 354.

[26] K. Salma, L. Berzina-Cimdina, and N. Borodajenko, *Calcium phosphate bioceramics prepared from wet chemically precipitated powders.* Processing and Application of Ceramics, 2010. **4**(1): p. 45-51.

[27] Y. Gu, W. Xiao, L. Lu, W. Huang, M.N. Rahaman, and D. Wang, *Kinetics and mechanisms of converting bioactive borate glasses to hydroxyapatite in aqueous phosphate solution.* Journal of Materials Science, 2011. **46**(1): p. 47-54.

[28] G.H. Nancollas and J. Zhang, *Formation and dissolution mechanisms of calcium phosphates in aqueous systems*, in *Hydroxyapatite and related materials*, P.W. Brown and B. Constantz, Editors. 1994, CPC Press, Inc.: United State of America. p. 73-81.

[29] W. Huang, M.N. Rahaman, D.E. Day, and Y. Li, *Mechanisms for converting bioactive silicate, borate, and borosilicate glasses to hydroxyapatite in dilute phosphate solution.* Physics and Chemistry of Glasses-European Journal of Glass Science and Technology Part B, 2006. **47**(6): p. 647-658.

[30] A.-H. Yao, J. Lin, X. Duan, and W.-H. Huang, *Formation mechanism of multilayered structure on surface of bioactive borosilicate glass.* Chinese Journal of Inorganic Chemistry, 2008. **24**(7): p. 1132-1136.

[31] S.B. Jung and D.E. Day, *Conversion kinetics of silicate, borosilicate, and borate bioactive glasses to hydroxyapatite.* Physics and Chemistry of Glasses-European Journal of Glass Science and Technology Part B, 2009. **50**(2): p. 85-88.

[32] D. Zhao, W. Huang, M.N. Rahaman, D.E. Day, and D. Wang, *Mechanism for converting Al 2O 3-containing borate glass to hydroxyapatite in aqueous phosphate solution.* Acta Biomaterialia, 2009. **5**(4): p. 1265-1273.

[33] A. Khawam and D.R. Flanagan, *Solid-state kinetic models: Basics and mathematical fundamentals.* Journal of Physical Chemistry B, 2006. **110**(35): p. 17315-17328.

[34] W. Huang, D.E. Day, and M.N. Rahaman, *Conversion of tetranary borate glasses to phosphate compounds in aqueous phosphate solution.* Journal of the American Ceramic Society, 2008. **91**(6): p. 1898-1904.

[35] S. Kuşlu, F.Ç. Dişli, and S. Çolak, *Leaching kinetics of ulexite in borax pentahydrate solutions saturated with carbon dioxide.* Journal of Industrial and Engineering Chemistry, 2010. **16**(5): p. 673-678.

[36] H. Temur, A. Yartaş, M. Çopur, and M. Muhtar Kocakerim, *The kinetics of dissolution of colemanite in H3PO4 solutions.* Industrial and Engineering Chemistry Research, 2000. **39**(11): p. 4114-4119.

[37] J.L. George, *Dissolution of borate glasses and precipitation of phosphate compounds*. 2015, Missouri University of Science and Technology.

[38] W. Xiao, B. Sonny Bal, and M.N. Rahaman, *Preparation of resorbable carbonate-substituted hollow hydroxyapatite microspheres and their evaluation in osseous defects in vivo.* Materials Science & Engineering C, 2016. **60**: p. 324-332.

[39] A.M. Abdelghany, H.A. ElBatal, and F.M. EzzElDin, *Bone bonding ability behavior of some ternary borate glasses by immersion in sodium phosphate solution.* Ceramics International, 2012. **38**(2): p. 1105-1113.

[40] K.L. Goetschius, *The effect of composition on the viscosity, crystallization and dissolution of simple borate glasses and compositional design of borate based bioactive glasses*. 2014, Missouri University of Science and Technology.

[41] A. Yao, D. Wang, W. Huang, Q. Fu, M.N. Rahaman, and D.E. Day, *In vitro bioactive characteristics of borate‐based glasses with controllable degradation behavior.* Journal of the American Ceramic Society, 2007. **90**(1): p. 303-306.

[42] A.K. Yadav and P. Singh, *A review of the structures of oxide glasses by Raman spectroscopy.* RSC Advances, 2015. **5**(83): p. 67583-6769.

[43] D. Maniua, T. Iliescu, I. Ardelean, S. Cinta-Pinzaru, N. Tarcea, and W. Kiefer, *Raman study on B2O3-CaO glasses.* Journal of Molecular Structure, 2003. **651-653**: p. 485-488.

[44] G.S. Sandhu, *Synthesis and characterization of microspheres for controlled release*. Masters theses, Missouri University of Science and Technology, 2010.

[45] Q. Wang, W. Huang, D. Wang, B.W. Darvell, D.E. Day, and M.N. Rahaman, *Preparation of hollow hydroxyapatite microspheres.* Journal of Materials Science: Materials in Medicine, 2006. **17**(7): p. 641-646.

[46] Manupriya, K.S. Thind, D. Singh, D.P. Singh, K. Singh, V. Kumar, and G. Sharma, *Compositional dependence of in-vitro bioactivity in sodium calcium borate glasses.* Journal of Physics and Chemistry of Solids, 2009. **70**(8): p. 1137-1141.

[47] A.M. Abdelghany, *Novel method for early investigation of bioactivity in different borate bio-glasses.* Spectrochimica Acta Part A: Molecular and Biomolecular Spectroscopy, 2013. **100**: p. 120-126.

[48] N. Eliaz and N. Metoki, *Calcium phosphate bioceramics: A review of their history, structure, properties, coating technologies and biomedical applications.* Materials, 2017. **10**(4): p. 334.

[49] H. Fu, M.N. Rahaman, D.E. Day, and R.F. Brown, *Hollow hydroxyapatite microspheres as a device for controlled delivery of proteins.* Journal of Materials Science: Materials in Medicine, 2011. **22**(3): p. 579-591.

[50] H. Fu, M.N. Rahaman, R.F. Brown, and D.E. Day, *Evaluation of bone regeneration in implants composed of hollow HA microspheres loaded with transforming growth factor β1 in a rat calvarial defect model.* Acta biomaterialia, 2013. **9**(3): p. 5718-5727.

[51] H. Fu, *Hollow Hydroxyapatite Microspheres as Devices for Controlled Delivery of Proteins and as Scaffolds for Tissue Engineering*. Doctoral Dissertations, Missouri University of Science and Technology, 2012.

[52] W. Xiao, H. Fu, M.N. Rahaman, Y. Liu, and B.S. Bal, *Hollow hydroxyapatite microspheres: A novel bioactive and osteoconductive carrier for controlled release of bone morphogenetic protein-2 in bone regeneration.* Acta Biomaterialia, 2013. **9**(9): p. 8374-8383.

[53] M.N. Rahaman, W. Xiao, Y. Liu, and B. Sonny Bal, *Osteoconductive and Osteoinductive Implants Composed of Hollow Hydroxyapatite Microspheres*, in *Advances in Bioceramics and Porous Ceramics VII*. 2014, John Wiley & Sons, Inc: Hoboken, NJ, USA. p. 65-79.

[54] S.V. Dorozhkin, *Calcium orthophosphate-based bioceramics.* Materials, 2013. **6**(9): p. 3840-3942.

[55] J.T.B. Ratnayake, M. Mucalo, and G.J. Dias, *Substituted hydroxyapatites for bone regeneration: A review of current trends.* Journal of Biomedical Materials Research Part B: Applied Biomaterials, 2017. **105**(5): p. 1285-1299.

[56] F.B. Bagambisa and U. Joos, *Preliminary studies on the phenomenological behaviour of osteoblasts cultured on hydroxyapatite ceramics.* Biomaterials, 1990. **11**(1): p. 50-56.

[57] D.O. Costa, P.D.H. Prowse, T. Chrones, S.M. Sims, D.W. Hamilton, A.S. Rizkalla, and S.J. Dixon, *The differential regulation of osteoblast and osteoclast activity bysurface topography of hydroxyapatite coatings.* Biomaterials, 2013. **34**(30): p. 7215-7226.

[58] S.L. Teitelbaum, *Bone Resorption by Osteoclasts.* Science, 2000. **289**(5484): p. 1504-1508.

[59] K. Lin, L. Xia, J. Gan, Z. Zhang, H. Chen, X. Jiang, and J. Chang, *Tailoring the nanostructured surfaces of hydroxyapatite bioceramics to promote protein adsorption, osteoblast growth, and osteogenic differentiation.* ACS Applied Materials and Interfaces, 2013. **5**(16): p. 8008-8017.

[60] S. Bertazzo, W.F. Zambuzzi, D.D.P. Campos, T.L. Ogeda, C.V. Ferreira, and C.A. Bertran, *Hydroxyapatite surface solubility and effect on cell adhesion.* Colloids and Surfaces B: Biointerfaces, 2010. **78**(2): p. 177-184.

[61] E. García-Gareta, M.J. Coathup, and G.W. Blunn, *Osteoinduction of bone grafting materials for bone repair and regeneration.* Bone, 2015. **81**: p. 112-121.

[62] C. Laurencin, Y. Khan, and S.F. El-Amin, *Bone graft substitutes.* Expert review of medical devices, 2006. **3**(1): p. 49-57.

[63] E. Nery, K. Lynch, W. Hirthe, and K. Mueller, *Bioceramic implants in surgically produced infrabony defects.* Journal of periodontology, 1975. **46**(6): p. 328-347.

[64] R. Detsch, H. Mayr, and G. Ziegler, *Formation of osteoclast-like cells on HA and TCP ceramics.* Acta Biomaterialia, 2008. **4**(1): p. 139-148.

[65] A.A. Mirtchi, J. Lemaitre, and N. Terao, *Calcium phosphate cements: study of the β-tricalcium phosphate — monocalcium phosphate system.* Biomaterials, 1989. **10**(7): p. 475-480.

[66] X. Hou, K. Mao, and D. Chen, *Bone formation performance of beta-tricalcium phosphate sintered bone.* J Clin Rehabil Tiss Eng Res, 2008. **12**: p. 9627-9630.

[67] D.S. Metsger, T. Driskell, and J. Paulsrud, *Tricalcium phosphate ceramic—a resorbable bone implant: review and current status.* The Journal of the American Dental Association, 1982. **105**(6): p. 1035-1038.

[68] N.E. Epstein, *Beta tricalcium phosphate: observation of use in 100 posterolateral lumbar instrumented fusions.* The Spine Journal, 2009. **9**(8): p. 630-638.

[69] J. Tao, H. Pan, H. Zhai, J. Wang, L. Li, J. Wu, W. Jiang, X. Xu, and R. Tang, *Controls of tricalcium phosphate single-crystal formation from its amorphous precursor by interfacial energy.* Crystal Growth and Design, 2009. **9**(7): p. 3154-3160.

[70] M. Bohner and J. Lemaitre, *Can bioactivity be tested in vitro with SBF solution?* Biomaterials, 2009. **30**(12): p. 2175-2179.

[71] I.R. Gibson, I. Rehman, S.M. Best, and W. Bonfield, *Characterization of the transformation from calcium-deficient apatite to β-tricalcium phosphate.* Journal of Materials Science: Materials in Medicine, 2000. **11**(12): p. 799-804.

[72] K.-R. Kang, Z.-G. Piao, J.-S. Kim, I.-A. Cho, M.-J. Yim, B.-H. Kim, J.-S. Oh, J.S. Son, C.S. Kim, and D.K. Kim, *Synthesis and Characterization of β-Tricalcium Phosphate Derived From Haliotis sp. Shells.* Implant dentistry, 2017. **26**(3): p. 378-387.

[73] G. Daculsi, R. LeGeros, M. Heughebaert, and I. Barbieux, *Formation of carbonate-apatite crystals after implantation of calcium phosphate ceramics.* Calcified tissue international, 1990. **46**(1): p. 20-27.

[74] G. Daculsi, R. LeGeros, E. Nery, K. Lynch, and B. Kerebel, *Transformation of biphasic calcium phosphate ceramics in vivo: ultrastructural and physicochemical characterization.* Journal of Biomedical Materials Research Part A, 1989. **23**(8): p. 883-894.

[75] M. Ebrahimi, M.G. Botelho, and S.V. Dorozhkin, *Biphasic calcium phosphates bioceramics (HA/TCP): Concept, physicochemical properties and the impact of standardization of study protocols in biomaterials research.* Materials Science & Engineering C, 2017. **71**: p. 1293-1312.

[76] R.Z. LeGeros, S. Lin, R. Rohanizadeh, D. Mijares, and J.P. LeGeros, *Biphasic calcium phosphate bioceramics: preparation, properties and applications.* Journal of Materials Science: Materials in Medicine, 2003. **14**(3): p. 201-209.

[77] G. Daculsi, *Biphasic calcium phosphate concept applied to artificial bone, implant coating and injectable bone substitute.* Biomaterials, 1998. **19**(16): p. 1473-1478.

[78] S.V. Dorozhkin, *Biphasic, triphasic and multiphasic calcium orthophosphates.* Acta Biomaterialia, 2012. **8**(3): p. 963-977.

[79] L. Bi, M.N. Rahaman, D.E. Day, Z. Brown, C. Samujh, X. Liu, A. Mohammadkhah, V. Dusevich, J.D. Eick, and L.F. Bonewald, *Effect of bioactive borate glass microstructure on bone regeneration, angiogenesis, and hydroxyapatite conversion in a rat calvarial defect model.* Acta Biomaterialia, 2013. **9**(8): p. 8015-8026.

[80] J. Samira, M. Saoudi, K. Abdelmajid, O. Hassane, R. Treq, E. Hafed, E. Abdelfatteh, and K. Hassib, *Accelerated bone ingrowth by local delivery of Zinc from bioactive glass: oxidative stress status, mechanical property, and microarchitectural characterization in an ovariectomized rat model.* Libyan Journal of Medicine, 2015. **10**(1): p. 28572-28572.

[81] A. Awonusi, M.D. Morris, and M.M.J. Tecklenburg, *Carbonate Assignment and Calibration in the Raman Spectrum of Apatite.* Calcified Tissue International, 2007. **81**(1): p. 46-52.

[82] Y. Lin, W. Xiao, B.S. Bal, and M.N. Rahaman, *Effect of copper-doped silicate 13–93 bioactive glass scaffolds on the response of MC3T3-E1 cells in vitro and on bone regeneration and angiogenesis in rat calvarial defects in vivo.* Materials Science & Engineering C, 2016. **67**: p. 440-452.

[83] H. Wang, S. Zhao, J. Zhou, Y. Shen, W. Huang, C. Zhang, M.N. Rahaman, and D. Wang, *Evaluation of borate bioactive glass scaffolds as a controlled delivery system for copper ions in stimulating osteogenesis and angiogenesis in bone healing.* Journal of Materials Chemistry B, 2014. **2**(48): p. 8547-8557.

[84] C. Zhang, J. Zhang, S. Zhao, M. Zhu, Y. Zhu, Y. Huang, and C. Tao, *Three-dimensional printing of strontium-containing mesoporous bioactive glass scaffolds for bone regeneration.* Acta Biomaterialia, 2014. **10**(5): p. 2269-2281.

[85] L.L. Hench, *The story of Bioglass®.* Journal of Materials Science: Materials in Medicine, 2006. **17**(11): p. 967-978.

[86] L.L. Hench, R.J. Splinter, W. Allen, and T. Greenlee, *Bonding mechanisms at the interface of ceramic prosthetic materials.* Journal of biomedical materials research, 1971. **5**(6): p. 117-141.

[87] M. Brink, *Bioactive glasses with a large working range*. 1997: Åbo Akademi University, Department of Chemical Engineering.

[88] M. Brink, *The influence of alkali and alkaline earths on the working range for bioactive glasses.* Journal of Biomedical Materials Research: An Official Journal of The Society for Biomaterials and The Japanese Society for Biomaterials, 1997. **36**(1): p. 109-117.

[89] M. Brink, T. Turunen, R.P. Happonen, and A. Yli-Urpo, *Compositional dependence of bioactivity of glasses in the system Na_2O-K_2O-MgO-CaO-B_2O_3-P_2O_5-SiO_2.* Journal of Biomedical Materials Research: An Official Journal of The Society for Biomaterials and The Japanese Society for Biomaterials, 1997. **37**(1): p. 114-121.

[90] L. Hupa and M. Hupa, *Recent Research on Composition Dependence of the Properties of Bioactive Glasses.* Advances in Bioceramics and Biotechnologies, 2010: p. 145-156.

[91] L. Hupa, *Composition-property relations of bioactive silicate glasses*, in *Bioactive Glasses*. 2018, Elsevier. p. 1-35.

[92] X. Liu, M.N. Rahaman, G.E. Hilmas, and B.S. Bal, *Mechanical properties of bioactive glass (13-93) scaffolds fabricated by robotic deposition for structural bone repair.* Acta Biomaterialia, 2013. **9**(6): p. 7025-7034.

[93] Y. Cao, B. Yang, C. Gao, P. Feng, and C. Shuai, *Laser sintering of nano 13-93 glass scaffolds: Microstructure, mechanical properties and bioactivity.* Science of Sintering, 2015. **47**(1): p. 31-39.

[94] N.D. Doiphode, T. Huang, M.C. Leu, M.N. Rahaman, and D.E. Day, *Freeze extrusion fabrication of 13–93 bioactive glass scaffolds for bone repair*. Journal of Materials Science: Materials in Medicine, 2011. **22**(3): p. 515-523.

[95] K.C.R. Kolan, M.C. Leu, G.E. Hilmas, R.F. Brown, and M. Velez, *Fabrication of 13-93 bioactive glass scaffolds for bone tissue engineering using indirect selective laser sintering.* Biofabrication, 2011. **3**(2): p. 025004-025004.

[96] S. Giannitelli, D. Accoto, M. Trombetta, and A. Rainer, *Current trends in the design of scaffolds for computer-aided tissue engineering.* Acta biomaterialia, 2014. **10**(2): p. 580-594.

[97] T.S. Huang, M.N. Rahaman, N.D. Doiphode, M.C. Leu, B.S. Bal, D.E. Day, and X. Liu, *Porous and strong bioactive glass (13–93) scaffolds fabricated by freeze extrusion technique.* Materials Science and Engineering: C, 2011. **31**(7): p. 1482-1489.

[98] Q. Fu, E. Saiz, and A.P. Tomsia, *Direct ink writing of highly porous and strong glass scaffolds for load-bearing bone defects repair and regeneration.* Acta Biomaterialia, 2011. **7**(10): p. 3547-3554.

[99] X. Liu, M.N. Rahaman, Y. Liu, B.S. Bal, and L.F. Bonewald, *Enhanced bone regeneration in rat calvarial defects implanted with surface-modified and BMP-loaded bioactive glass (13-93) scaffolds.* Acta Biomaterialia, 2013. **9**(7): p. 7506-17.

[100] X. Liu, M.N. Rahaman, and Q. Fu, *Bone regeneration in strong porous bioactive glass (13-93) scaffolds with an oriented microstructure implanted in rat calvarial defects.* Acta Biomaterialia, 2013. **9**(1): p. 4889-4898.

[101] L. Bi, S. Jung, D. Day, K. Neidig, V. Dusevich, D. Eick, and L. Bonewald, *Evaluation of bone regeneration, angiogenesis, and hydroxyapatite conversion in critical-sized rat calvarial defects implanted with bioactive glass scaffolds.* Journal of Biomedical Materials Research Part A, 2012. **100A**(12): p. 3267-3275.

[102] A. Scarano, V. Perrotti, L. Artese, M. Degidi, D. Degidi, A. Piattelli, and G. Iezzi, *Blood vessels are concentrated within the implant surface concavities: a histologic study in rabbit tibia.* Odontology, 2014. **102**(2): p. 259-266.

[103] M.J. Coathup, K.A. Hing, S. Samizadeh, O. Chan, Y.S. Fang, C. Campion, T. Buckland, and G.W. Blunn, *Effect of increased strut porosity of calcium phosphate bone graft substitute biomaterials on osteoinduction.* Journal of Biomedical Materials Research Part A, 2012. **100**(6): p. 1550-1555.

[104] U.R. Ripamonti, *Functionalized surface geometries induce:" Bone: formation by autoinduction".* Frontiers in physiology, 2017. **8**: p. 1084.

VITA

Youqu Shen was born in 1989 in Liuzhou, Guangxi, China. She recieved her B.S. degree in Electronic Packaging Technology in 2011 from Harbin Institute Technology in China. Youqu started her graduate study under the supervision of Dr. Deping Wang in 2011 at Tongji University in China. She received her M.S. degree in Materiology in 2014.

In 2014, Youqu started to persue her Ph.D. in Material Science and Engineering at Missouri University of Science and Technology at Rolla, MO, USA. She worked mainly on biomaterials for bone regeneration under the supervision of Dr. Mohamed N. Rahaman at the start of the research and Dr. Richard K. Brow at the finish of the research. In December 2019, she received her Ph.D. degree in Material Science and Engineering from Missouri University of Science and Technology.